The Astrophysical Journal, 1008:240 (31pp), 2026 September 10 https://doi.org/10.3847/1538-4357/ae879b
© 2026. The Author(s). Published by the American Astronomical Society.
OPEN ACCESS

The LBT Y_p Project. IV. A New Value of the Primordial Helium Abundance

Erik Aver[1,10], Evan D. Skillman[2], Richard W. Pogge[3,4], Noah S. J. Rogers[5], Miqaela K. Weller[3], Keith A. Olive[6], Danielle A. Berg[7], John J. Salzer[8], John H. Miller, Jr.[2], and José Eduardo Méndez-Delgado[9]
[1] Department of Physics, Gonzaga University, 502 East Boone Avenue, Spokane, WA 99258, USA; aver@gonzaga.edu
[2] Minnesota Institute for Astrophysics, University of Minnesota, 116 Church Street SE, Minneapolis, MN 55455, USA
[3] Department of Astronomy, The Ohio State University, 140 West 18th Avenue, Columbus, OH 43210, USA
[4] Center for Cosmology & AstroParticle Physics, The Ohio State University, 191 West Woodruff Avenue, Columbus, OH 43210, USA
[5] Center for Interdisciplinary Exploration and Research in Astrophysics (CIERA), Northwestern University, 1800 Sherman Avenue, Evanston, IL 60201, USA
[6] William I. Fine Theoretical Physics Institute, School of Physics and Astronomy, University of Minnesota, Minneapolis, MN 55455, USA
[7] Department of Astronomy, The University of Texas at Austin, 2515 Speedway, Stop C1400, Austin, TX 78712, USA
[8] Department of Astronomy, Indiana University, 727 East Third Street, Bloomington, IN 47405, USA
[9] Instituto de Astronomía, Universidad Nacional Autónoma de México, Ap. 70-264, 04510, CDMX, Mexico
Received 2026 January 29; revised 2026 April 24; accepted 2026 April 28; published 2026 September 9

Abstract

We present a new determination of the primordial helium abundance based on new, high-quality Large Binocular Telescope (LBT) observations of 54 metal-poor H II regions. These regions have been observed and analyzed uniformly. We also describe a number of updates to our methodology, including updated helium emissivities. Enabled by the large, high-quality dataset, we examine our sample targets for potential systematic errors, which could bias their results. We perform a standard 95% confidence level (CL) χ^2 cut and find that a significantly larger fraction ($47/54 = 87\%$) of our sample qualifies than for previous datasets. We also screen for quality and reliability, flagging targets that may introduce significant systematic errors, producing a dataset of 41 targets. In a significant breakthrough for the field, that dataset includes 15 high signal-to-noise ratio (SNR) targets with low metallicity ($O/H \leqslant 4 \times 10^{-5}$). Due to this low-metallicity dataset, for the first time, a weighted average for determining the primordial helium abundance (y_p) is well justified and produces a robust result. By weighted average of our 15 low-metallicity targets, we determine $y_p = 0.08146 \pm 0.00058$, with the corresponding mass fraction $Y_p = 0.2458 \pm 0.0013$. This result achieves an unprecedented precision of 0.5%, and it is in good agreement with the Big Bang nucleosynthesis (BBN) result, $Y_p = 0.2467 \pm 0.0002$, based on the Planck determination of the baryon density.

Unified Astronomy Thesaurus concepts: Chemical abundances (224); H II regions (694); Cosmic abundances (315); Big Bang nucleosynthesis (151); Infrared spectroscopy (2285); Spectroscopy (1558)

1. Introduction

Observations of the cosmic microwave background (CMB) and its anisotropy spectrum have provided unparalleled information about the early Universe up to a redshift $z \simeq 1100$ (Planck Collaboration 2020). Examples of high-precision determinations include the Hubble parameter, cold dark matter density, baryon density, and total density. With higher-resolution experiments (E. Camphuis et al. 2025; T. Louis et al. 2025), the primordial helium abundance, Y_p, and the effective number of neutrino degrees of freedom, N_{eff}, may soon join this list. Big Bang nucleosynthesis (BBN), however, enables one to probe the early Universe back to redshifts of order $z \sim 10^{10}$, when the temperature of the radiation background was of order 1 MeV. At these temperatures, protons and neutrons are processed to form the light-element isotopes, D, ^{3}He, ^{4}He, and ^{7}Li (K. A. Olive et al. 2000; F. Iocco et al. 2009; R. H. Cyburt et al. 2016; C. Pitrou et al. 2018; B. D. Fields et al. 2020).

Standard Model physics up to the MeV scale is well understood, and if provided with precision determinations of the light-element abundances, the physics of the early Universe can be tested. To do so requires accurate *primordial abundance determinations*, that is, abundances in astrophysical environments that have not been contaminated by either stellar production, astration, or depletion. For example, ^{3}He is both produced and destroyed in stars (K. A. Olive et al. 1995, 1997; D. S. P. Dearborn et al. 1996), making it difficult to extract a primordial abundance from available observations (E. Vangioni-Flam et al. 2003). ^{7}Li abundance determinations in low-mass halo dwarf stars were long thought to provide a good measure of the primordial abundance (F. Spite & M. Spite 1982; J. Yang et al. 1984). The degree to which ^{7}Li has been destroyed in its host star is unclear (B. D. Fields & K. A. Olive 2022). In contrast, there are several high-precision determinations of D/H in high-redshift ($z \sim 3$) quasar absorption systems (R. J. Cooke et al. 2014, 2016, 2018; S. Riemer-Sørensen et al. 2015, 2017; S. A. Balashev et al. 2016; E. O. Zavarygin et al. 2018; F. Guarneri et al. 2024; P. A. Kislitsyn et al. 2024), which have enabled precision tests of the compatibility between BBN and CMB observations. Our goal here is to provide a high-precision determination of the primordial ^{4}He abundance.

Y_p needs to be measured to high accuracy to provide any diagnostic power. In the currently favored method of measuring relative abundances in ionized plasmas associated with low-metallicity star-forming regions, this means accounting for a number of effects that can alter the observed ratios of the H and He emission lines. In addition to measuring the

[10] Corresponding author.

Original content from this work may be used under the terms of the Creative Commons Attribution 4.0 licence. Any further distribution of this work must maintain attribution to the author(s) and the title of the work, journal citation and DOI.

appropriate values of temperature and density, which determine the emissivities required to convert the recombination emission line ratios into relative abundances, there are a number of other factors that need to be accounted for. These have been identified as reddening by the intervening interstellar medium, the stellar absorption profiles underlying the emission lines, the collisional excitation of H lines (which requires measuring the neutral hydrogen fraction), and the radiative transfer gains and losses in the He triplet lines due to the presence of the 2^3S metastable level. All of these effects have various histories of corrections. Those histories will not be enumerated here, but we strive to be as clear as possible concerning how we deal with each of these corrections, as discussed in Section 2.

The absence of direct measurements of the physical quantities that enter into the model may lead to significant systematic uncertainties in the derived helium abundance. Historically, reasonable values for the physical parameters were adopted, ignoring their inherent uncertainties. Our method for accounting for and estimating the size of the systematic errors is described in Section 2. The physical parameters are treated on an equal footing with the helium abundance, and together, they are all determined simultaneously by minimizing the χ^2 likelihood function, which compares the observed emission line fluxes with model predictions. A Markov Chain Monte Carlo (MCMC) exploration of the parameter space then allows us to determine the uncertainties in each parameter including the helium abundance. This method typically leads to larger calculated uncertainties in the helium abundance, thereby motivating higher precision to reduce these (more realistic) uncertainties.

Based on the success in significantly lowering the uncertainty on a helium abundance measurement in the metal-poor galaxy Leo P (E. Aver et al. 2021), we proposed to obtain new, high-quality optical and near-infrared (NIR) spectra of as many known low-metallicity galaxies as possible. For that project, we prioritize low values of measured oxygen abundance and high values of hydrogen emission line flux and equivalent width. Many known low-metallicity galaxies are too faint to provide sufficiently small uncertainties on their helium abundances with a reasonable amount of telescope time, so not all known low-metallicity galaxies were pursued. Nonetheless, we were able to compile a sample of high-quality spectra enabling a significant step forward in the determination of Y_p.

This is the fourth paper in the series of the LBT Y_p Project. Papers I–III (N. S. J. Rogers et al. 2026; E. D. Skillman et al. 2026; M. K. Weller et al. 2026) presented an overview of the project, our new LBT MODS optical spectra, and our new Large Binocular Telescope (LBT) LUCI NIR spectra, respectively. Paper I also provides an overview and history of primordial helium abundance determinations. This paper is followed by Paper V (T.-H. Yeh et al. 2026) demonstrating the impact of our new Y_p determination, and Paper VI (N. Rogers et al. 2026, in preparation) will present a complete survey of all of the metal abundances derived from our new LBT MODS spectra.

This paper is organized as follows. First, in Section 2, we discuss the basic theoretical model for the analysis of ^{4}He data, including recent updates that have been made. Model equations and data for those updates are provided in Appendices A–F. In Section 3, we provide the requirements for inclusion in the sample used for determining Y_p. The results of the χ^2 cut for our sample are discussed in Section 4. We then examine that qualifying dataset for systematic errors in Section 5, and we review the best-fit physical parameters and the effects of key model updates in Section 6. In Section 7, we derive the resulting primordial helium abundance. Two avenues for future investigation and improvements to further reduce potential systematic errors are discussed in Section 8. Finally, Section 9 offers a discussion of the results and prospects for improvement.

2. Model

H II regions are emission nebulae photoionized by one or more massive stars (O and B stars). Correspondingly, their spectra include nebular emission lines overlaid on a stellar continuum. In seeking the helium abundance, $y^+ = \frac{n(\mathrm{He}^+)}{n(\mathrm{H}^+)}$, we model the primary emission region using a radiative transfer model based on the "Case B" approximation (optically thick to Lyman lines). For hydrogen and helium, recombination emission dominates, but collisional excitation also contributes, with hydrogen collisional excitation from the small fraction of neutral hydrogen in the ionized region, ξ. Self-absorption and reemission of photons within the nebula also occur. The radiative transfer model assumes a uniform H II region with an average electron density, n_e, and average electron temperature, T_e, as well as optical depth, τ. The stellar continuum juxtaposes absorption features under the nebular helium and hydrogen emission lines, including separate parameters for the Balmer and Paschen lines, a_{He}, a_H, and a_P, respectively (E. Aver et al. 2021). Dust along the line of sight also scatters the emitted photons (interstellar reddening, $C(H\beta)$).

We determine the helium abundance in an individual H II region based on an MCMC analysis. The MCMC method is an algorithmic procedure for sampling from a statistical distribution (A. A. Markov 1906; N. Metropolis et al. 1953). We define a χ^2 distribution from the difference between flux ratios,

$$\chi^2 = \sum_{\lambda} \frac{\left(\frac{F(\lambda)}{F(\mathrm{H}\beta\,|\,P\gamma)} - \frac{F(\lambda)}{F(\mathrm{H}\beta\,|\,P\gamma)_{\mathrm{meas}}}\right)^2}{\sigma(\lambda)^2}, \quad (1)$$

where the emission line fluxes, $F(\lambda)$, are measured and calculated for a set of H and He lines and $\sigma(\lambda)$ is the measured uncertainty in the flux ratio at each wavelength. The optical/NIR emission line fluxes from the LBT/MODS spectra are calculated relative to Hβ, while the infrared flux of He I λ10830 is calculated relative to the IR Paschen line, Pγ. Thus, by $F(\mathrm{H}\beta|\mathrm{P}\gamma)$, we mean $F(\mathrm{H}\beta)$ for all lines other than He I λ10830 and $F(\mathrm{P}\gamma)$ for the latter.

Up to eight helium line ratios are employed: $\lambda\lambda$4026, 4388, 4471, 4922, 5876, 6678, and 7065, relative to Hβ, and λ10830, relative to Pγ. He I λ5016 was previously employed (E. Aver et al. 2021), and He I λ7281 is available in our model, but, as discussed below (Section 2.3), there is evidence for significant systematic bias in these two emission lines (Y. I. Izotov et al. 2007; J. E. Méndez-Delgado et al. 2025). As a result, they have been excluded from our analysis here. Up to 15 hydrogen line ratios are employed, Hα, Hγ, Hδ, H9, H10, H11, H12, P8, P9, P10, P11, P12, P13, P14, and P15, relative to Hβ. Finally, the blended line He I λ3889 + H8, relative to Hβ, is also utilized. Depending on the observed target's signal-to-noise

ratio (SNR), not all of the preceding lines are detected and used (see Section 4.1).

The observed line ratios are used to fit up to nine model parameters, as introduced above (E. Aver et al. 2021): T_e, n_e, τ, $C(H\beta)$, a_{He}, a_H, a_P, ξ, and y^+. Thus, if all of the above emission lines are detected and employed, we are left with 15 degrees of freedom, corresponding to a total of 24 observed line ratios and nine parameters to fit.

The MCMC scans of our 9D parameter space map out the χ^2 distribution given above. We conduct a frequentist analysis, and the χ^2 is minimized to determine the best-fit solution for the nine model parameters, including y^+, as well as determining the goodness of fit. Uncertainties in each quantity are estimated by calculating a 1D marginalized likelihood and finding the 68% confidence interval from the increase in the χ^2 from the minimum.

Our entire model and the data employed, including the model equations for the helium and hydrogen flux ratios and relevant parameterizations, are given in full and detailed in the extensive appendices in E. Aver et al. (2021). Please see that work for details and a comprehensive accounting. Since that work, the following updates have been made to our model.

1. The helium and hydrogen emissivities have been updated to employ the most recent calculations based on the latest atomic data and modeling improvements (P. J. Storey & T. Sochi 2015; G. Del Zanna & P. J. Storey 2022). These helium and hydrogen emissivities have been computed on higher-resolution temperature and density grids.
2. The radiative transfer model has been updated to employ the most recent calculations based on the latest atomic data and modeling improvements (O. Kurichin & A. Ivanchik 2026, hereafter KI26). Previously, limited-range fitting equations were employed (R. A. Benjamin et al. 2002, hereafter BSS02). In addition to the updates to the calculations, the new radiative transfer equations were fit over an expanded parameter range, largely eliminating potential extrapolation.
3. Three hydrogen Paschen series emission lines, P13, P14, and P15, were added to the model, increasing the maximum number of Paschen lines employed from five to eight, spanning from P8 to P15 (all in the NIR from the MODS optical + NIR spectrum).
4. The radiative transfer treatment of the blended emission line H8 + He I λ3889 was revised. In particular, the radiative transfer correction to H8 due to absorption by He I λ3889 was removed. The two lines are separated by 0.4 Å, and the number density of He atoms compared to H atoms is less than one-tenth. As a result, the absorption of H8-emitted photons by He is expected to be relatively rare, with negligible impacts on the H8 or He fluxes (He I $\lambda\lambda$3889, 7065, 10830).
5. The neutral hydrogen fraction, ξ, is not included as a fit parameter in our model for temperatures below 14,000 K. Below 14,000 K, the potential emission from the collisional excitation is negligible, due to its exponential dependence on temperature.

Further discussion of the new helium and hydrogen emissivities, the new radiative transfer calculations, the excluded He I λ5016 and λ7281 emission lines, and the treatment of neutral hydrogen collisional excitation is given below (Sections 2.1, 2.2, 2.3, and 2.4, respectively). The corresponding updates to the equations and data provided in the Appendices in E. Aver et al. (2021) are provided here in Appendices A–F.

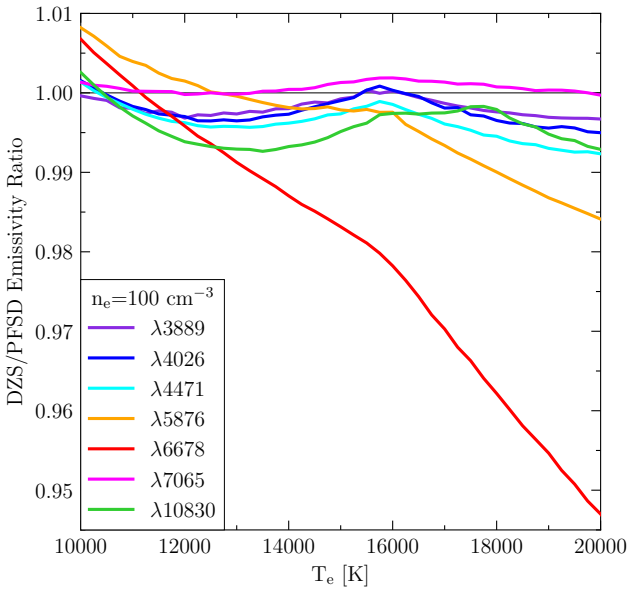


Figure 1. The G. Del Zanna & P. J. Storey (2022) emissivities plotted relative to those of R. L. Porter et al. (2012, 2013) as a function of temperature at $n_e = 100$ cm^{-3} for the core He emission lines, He I $\lambda\lambda$3889, 4026, 4471, 5876, 6678, 7065, and 10830. At low density, all of the He emission lines employed in this work show changes of $\lesssim$1% and typically a slight decrease, except for He I λ6678, which shows a more significant decrease.

2.1. He and H Emissivities

G. Del Zanna & P. J. Storey (2022) have published updated He emissivities based on improved collision rates and that correct some errors in previous He emissivity calculations (please see G. Del Zanna & P. J. Storey 2022 for details). Extending that work, G. Del Zanna graciously agreed to calculate the updated He emissivities on a higher-resolution temperature and density grid to help limit interpolation errors (private communication, 2022). Those He emissivities calculated on the finer grid are employed in this work and are available from the authors by request. As discussed in G. Del Zanna & P. J. Storey (2022) and shown below, the largest deviations from the previously employed R. L. Porter et al. (2012, 2013) emissivities occur for He I λ6678, and the deviations increase with density. Figures 1 and 2 compare the G. Del Zanna & P. J. Storey (2022) and R. L. Porter et al. (2012, 2013) emissivities versus temperature (at n_e = 100 cm^{-3}) and density (at T_e = 15,000 K), respectively. With the exception of He I λ6678 and for the low densities most relevant for our sample, all of the He emission lines employed in this work show changes of $\lesssim$1%. The effect of the updated He emissivities on the helium abundance is discussed in Section 6.2.

P. J. Storey & T. Sochi (2015) have published updated H emissivities. Extending that work, P. Storey graciously agreed to calculate the updated H emissivities on a higher-resolution temperature and density grid (private communication, 2023). Those H emissivities calculated on the finer grid are employed in this work and are available from the authors by request. Updated fit equations for the emissivity ratios, relative to Hβ, are provided in Appendix C. At the low densities applicable to

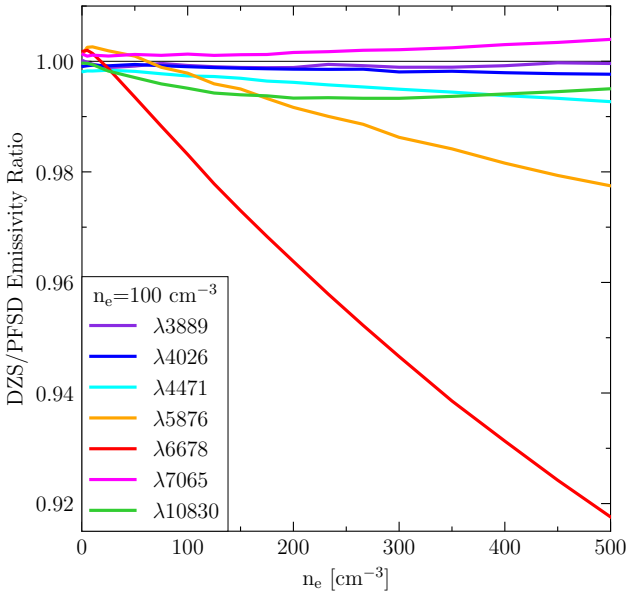


Figure 2. The G. Del Zanna & P. J. Storey (2022) emissivities plotted relative to those of R. L. Porter et al. (2012, 2013) as a function of density at $T_e = 15{,}000$ K for the core He emission lines, He I $\lambda\lambda$3889, 4026, 4471, 5876, 6678, 7065, and 10830. Across the range of densities spanning our qualifying sample, all of the He emission lines employed in this work show changes of $\lesssim$1% and typically a slight decrease, except for He I λ6678, which shows a more significant decrease.

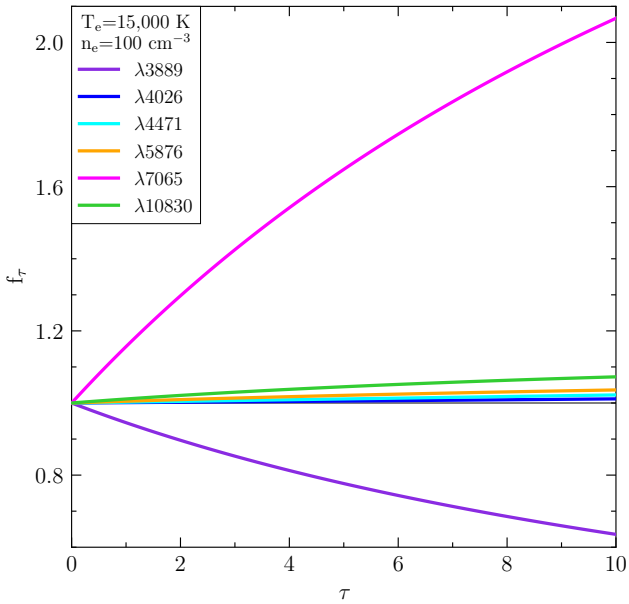


Figure 3. The KI26 radiative transfer corrections, f_τ, plotted as a function of optical depth ($\tau = \tau_{3889}$) at $n_e = 100\,\mathrm{cm}^{-3}$ and $T_e = 15{,}000$ K for the He triplet emission lines, He I $\lambda\lambda$3889, 4026, 4471, 5876, 7065, and 10830. As shown, radiative transfer results in a net decrease in He I λ3889 emission and a net increase in He I λ7065 emission, with those two lines by far the most strongly affected.

the H II regions in this work, the updated P. J. Storey & T. Sochi (2015) H emissivities and the previously employed D. G. Hummer & P. J. Storey (1987) emissivities are essentially identical, with the largest deviation across our range of densities and temperatures being <0.05%.

Given the higher-resolution grid for the H emissivities, the normalizing emissivity values for Balmer series Hβ and Paschen series Pγ, E(Hβ) and E(Pγ), were also updated to employ the latest data and for consistency. The previously employed Hβ emissivity fit equation did not include density dependence and was based on CLOUDY modeling calculations by R.L. Porter (E. Aver et al. 2010, 2021). The difference varies with temperature and density, but the P. J. Storey & T. Sochi (2015) Hβ emissivity data show a systematic increase ranging from $\sim$0.1% to $\sim$0.25% compared to the previous fit equation across our dataset. The previous Pγ fit equation (E. Aver et al. 2021) was based on D. G. Hummer & P. J. Storey (1987), with the new P. J. Storey & T. Sochi (2015) data nearly identical for the low densities relevant for our work. However, the higher-resolution temperature and density data allowed for a more accurate fit equation. The updated E(Hβ) and E(Pγ) fit equations are provided in Appendix C.

2.2. Radiative Transfer

Radiative transfer for the He triplet emission lines is accounted for in our model-predicted flux via a multiplicative correction term, f_τ, parameterized in terms of optical depth for He I λ3889 at line center (i.e., $\tau = \tau_{3889}$, and see E. Aver et al. 2021 for model implementation).

Very recently, KI26 produced updated radiative transfer calculations, and we have adopted them for this work. The new KI26 radiative transfer calculations are based on the latest atomic data, as well as improvements in modeling, including an expanded number of energy levels and an improved treatment of collisional transitions.

For comparison, we refer to the previous radiative transfer results from BSS02. BSS02 included limited-range fitting equations, as well as an expanded grid for interpolation. The equations were fit over the parameter ranges $12{,}000\,\mathrm{K} < T_e < 20{,}000\,\mathrm{K}$, $1\,\mathrm{cm}^{-3} < n_e < 300\,\mathrm{cm}^{-3}$, and $0 < \tau < 2$. In our previous analyses, we used the fit equations. However, given their limited range and the presence of significantly higher optical depth targets in our sample, they were not well suited to this work. To avoid extrapolation and following the approach in D. A. Berg et al. (2026), we had switched to trilinear interpolation based on the program developed by BSS02. However, upon the release of the updated KI26 radiative transfer calculations, we adopted them for this work. We compare all three of these results below.

KI26 provide equations fit over the parameter ranges $8000\,\mathrm{K} < T_e < 22{,}000\,\mathrm{K}$, $1\,\mathrm{cm}^{-3} < n_e < 10{,}000\,\mathrm{cm}^{-3}$, and $0 < \tau < 10$ with an accuracy of $\lesssim$0.1%. Those expanded parameter ranges nearly eliminate the possibility of extrapolation beyond the fit range for our targets, except perhaps for rare targets with higher optical depths, $\tau > 10$. However, systems with such high optical depths are suspect and may be less reliable, given the large radiative transfer effects and the potential for more complex dynamics. As such, targets with $\tau > 10$ are less desirable for helium abundance determinations, and we caution against relying on them (see Section 5.1 below). The KI26 fit equations employed in this work are reproduced in Appendix D.

Figure 3 shows the radiative transfer correction term, f_τ, plotted versus optical depth ($\tau = \tau_{3889}$) for all He triplet lines utilized in our model. The functions plotted are the fit equations from KI26. Absorption within the H II region and subsequent reemission—but frequently at longer wavelengths—decreases He I λ3889 emission while increasing net

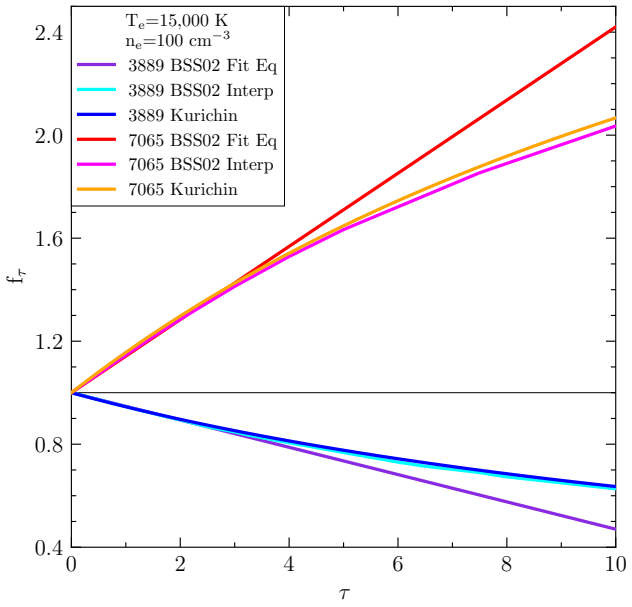


Figure 4. The KI26 and BSS02 radiative transfer corrections, f_τ, plotted as a function of optical depth ($\tau = \tau_{3889}$) at $n_e = 100$ cm^{-3} and $T_e = 15{,}000$ K for He I λ3889 and He I λ7065, the two He emission lines most strongly affected by radiative transfer. The plot compares the limited-range fitting function and the trilinear interpolation program from BSS02 and the updated results of KI26. As is the case for all He triplet lines affected by radiative transfer, the magnitude of the radiative transfer effect is overestimated by extrapolation based on the limited-range fitting function, which was fit for $0 < \tau < 2$. The BSS02 interpolation and KI26 fit equations are more similar, though with differences that increase for higher optical depths (and also for higher densities, especially for He I λ7065).

He I λ7065 emission (see description in D. E. Osterbrock & G. J. Ferland 2006). As Figure 3 shows, these two emission lines are by far the most strongly affected by radiative transfer.

Figure 4 compares the BSS02 limited-range fit equation, the BSS02 interpolation grid, and the KI26 fit equations as optical depth increases. As shown in Figure 4, the dominant effect of moving from the limited-range fit equations from BSS02 to the BSS02 interpolation grid or the KI26 fit equations is to decrease the radiative transfer effect at higher optical depths (compared to extrapolating beyond $\tau > 2$ using the limited-range fit equations). This applies across all triplet He lines. The BSS02 limited-range fit equations are linear with τ, so it is not surprising that the radiative transfer effects depart from that linear extrapolation. These differences grow steadily for $\tau > 2$, exceed 10% for He I λ3889 for $\tau > 6$, and reach 35% and 15% at $\tau = 10$ for He I λ3889 and He I λ7065, respectively.

As a result, the best-fit optical depth values for targets returning $\tau > 2$, but especially for $\tau > 4$, are larger using the BSS02 interpolation grid or KI26 fit equations compared to the best-fit optical depth resulting from the BSS02 limited-range fit equations. This comparative increase is a consequence of comparing to the results based on an extrapolation of the limited-range fit equations beyond their fit domain. The KI26 differences with the underlying BSS02 results are much smaller, though still significant, as is discussed next and illustrated in Section 6.3.

Compared to interpolation based on the BSS02 calculations, the new calculations of KI26 are similar for most emission lines, with differences of less than 1% across the fit range. The differences are larger for He I λ3889 and He I λ7065 and tend to increase with optical depth, as is shown in Figure 4 with $n_e = 100\,\mathrm{cm}^{-3}$ and $T_e = 15{,}000$ K. For He I λ3889 and He I λ7065, these differences between the BSS02 interpolation and the KI26 calculations exceed 1% for $\tau > 5$, reaching 1.5% at $\tau = 8$. At higher densities, larger differences open up for the more collisionally sensitive He I λ7065 emission line, in particular. For $n_e = 300\,\mathrm{cm}^{-3}$, the difference grows to 10% at $\tau = 10$.

As discussed above, He I λ7065 is the most strongly affected by radiative transfer, and it shows the largest relative changes from the updated calculations by KI26. As shown in Figure 4, the KI26 calculations slightly increase the magnitude of the boost from radiative transfer for He I λ7065 compared to the BSS02 calculations (i.e., the BSS02 interpolation). Correspondingly, for targets with higher optical depth values, the adoption of the updated KI26 radiative transfer model results in a moderate decrease in the best-fit optical depth compared to the BSS02 radiative transfer model. This finding will be further examined and discussed in Section 6.3.

2.3. He I λ5016 and λ7281

Y. I. Izotov et al. (2007) and later J. E. Méndez-Delgado et al. (2025) found significant systematic discrepancies in observed He I λ5016 and λ7281 fluxes compared to standard Case B modeling and assumed temperature homogeneity. Correspondingly, J. E. Méndez-Delgado et al. (2025) investigate two hypotheses for these discrepancies: (1) deviations from Case B due to photon loss and/or (2) significant temperature inhomogeneities. Both scenarios were found to be possible sources of the observed discrepancies. Regardless, the observed discrepancies, with both lines systematically biased low compared to the model, make them unsuitable for calculating their corresponding helium abundance using the available atomic data and model. The inclusion of those lines would systematically bias the result. The finding from J. E. Méndez-Delgado et al. (2025) was reinforced by our own analysis, which showed that the measured fluxes for both emission lines were systematically low compared to the model prediction based on the best-fit parameter solution for the full set of He and H lines (see Section 2 above for a summary of our model and methodology and E. Aver et al. 2021 for a full description). As such, we exclude both lines from our analysis.

2.4. Neutral Hydrogen Collisional Correction

As shown in Figure 5, emission from the collisional excitation of neutral hydrogen has a strong exponential dependence on the electron temperature (E. Aver et al. 2010, 2021). As a result, at low temperatures, the potential contribution from neutral hydrogen is negligible. However, as discussed in E. Aver et al. (2012), this extremely low collisional emission rate can drive the model's best-fit parameter solution toward increasingly large and completely nonphysical fractions of neutral hydrogen in the H II region. As we have improved and expanded our model with additional H emission lines, this degenerate result from our model has been diminished, and the best fit for the neutral hydrogen fraction, ξ, has become better constrained (E. Aver et al. 2021).

However, given that, *physically*, the collisional excitation rate is completely negligible compared to the recombination rate at low temperatures as discussed in E. Aver et al. (2010, 2021) and shown in Figure 5, trying to solve for the

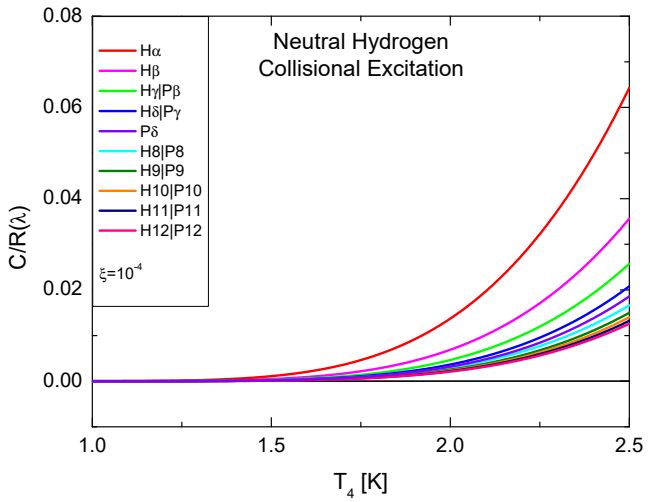


Figure 5. The collisional excitation relative to recombination rate for the hydrogen emission lines due to neutral hydrogen. The behavior is dominantly exponential with temperature, with, as expected, larger corrections for the lower-level (lower-energy) emission lines. Reproduced from E. Aver et al. (2021).

fraction of neutral hydrogen becomes physically meaningless. Correspondingly, the correction for neutral hydrogen collisional excitation is not included in our model below electron temperatures of 14,000 K ($T_4 < 1.4$). As a result, for temperatures below 14,000 K, the neutral hydrogen fraction, ξ, is no longer included as one of our model parameters, and our number of model parameters decreases from nine to eight.

3. Sample Selection

Papers I, II, and III discuss our target selection, optical and NIR MODS observations, and NIR LUCI observations, respectively. The He and H emission line flux ratios utilized in our model (see Section 2) are measured from the MODS spectra and reported in Paper II, with the exception of He I λ10830, where the values are measured from the LUCI NIR spectra and reported in Paper III or are taken from the literature. Paper II also includes the determination of T(O III) and O/H for those observed targets. For determining the primordial helium abundance, y_p, and corresponding mass fraction, Y_p, the following criteria were required for our dataset.

1. O/H $< 15 \times 10^{-5}$ *(26% of solar)*. Ideally, one would assemble a large dataset of only the lowest-metallicity, extremely metal-poor (XMP) galaxies (O/H $< 2.24 \times 10^{-5}$; N. G. Guseva et al. 2015; K. B. W. McQuinn et al. 2020), but, as discussed in Paper I, such targets are rare and tend to be faint. Nevertheless, targeting a reduced metallicity baseline limits the potential systemic error introduced by enrichment of He and/or of an assumed linear relationship between He and O (between Y and O/H). Correspondingly, we prioritized the lowest-metallicity targets from the literature, which still met our criteria for producing high-SNR spectra (namely, F(Hβ) $\gtrsim 3 \times 10^{-15}$ erg s^{-1}cm^{-2} and W(Hβ) $\gtrsim$ 100; see Paper I). We particularly emphasized targets with O/H $\leqslant 4 \times 10^{-5}$ (7% of solar; K. Lodders et al. 2025) for their impact on determining Y_p and prioritized them over observing more evenly across our metallicity range. As we exhausted our identified high-SNR targets, we worked our way up in metallicity with a set cutoff of O/H $< 15 \times 10^{-5}$ (26% of solar). This is still a relatively constrained metallicity baseline compared to many other Y_p analyses (e.g., Y. I. Izotov et al. 2007; V. Fernández et al. 2019; O. A. Kurichin et al. 2021). Furthermore, our sample coverage at low metallicity is much higher than other Y_p analyses (e.g., Y. I. Izotov et al. 2007; V. Fernández et al. 2019; T. Hsyu et al. 2020; O. A. Kurichin et al. 2021; H. Yanagisawa et al. 2026). Two targets, UM 420 and Mrk 5, were proposed based on literature O/H values that were less than our cutoff but returned O/H values exceeding it. As such, they were excluded from our He analysis dataset.
2. He I λ*4026 detected (>3σ)*. The weaker He emission lines are more sensitive to the effects of underlying stellar absorption, and, relative to its strength, the weak emission line He I λ4026 is the most sensitive (excluding He I λ3889, which is blended with H8 and is a stronger line). Therefore, He I λ4026 is a strong diagnostic for determining the underlying absorption. Furthermore, as shown in E. Aver et al. (2012), the absence of He I λ4026 can bias the result, due to overestimating the underlying absorption for the helium lines and hence overestimating the helium abundance. Two observed targets, HSC J2314+0154 and KUG 0743+513, were too faint for He I λ4026 detections. As a result, they were excluded from our He analysis dataset. Note that, when detected, we employ the fainter He emission lines, He I λ4388 and λ4922, which are also quite sensitive to underlying absorption, but when He I λ4026 is not detected, not surprisingly, He I λ4388 and λ4922 are also not detected.
3. He I λ*10830 measured.* As discussed in Paper II, He I λ10830 is much more sensitive to collisional excitations, and thus the electron density, than any of our other observed He emission lines (Y. I. Izotov et al. 2014; E. Aver et al. 2015). Correspondingly, E. Aver et al. (2015) demonstrated the crucial role He I λ10830 plays in helping break the temperature–density degeneracy (K. A. Olive & E. D. Skillman 2004; E. Aver et al. 2010, 2011). Therefore, He I λ10830 is a required emission line for our analysis. For most of our targets, He I λ10830 was measured from our LUCI spectra, but for 11 targets, literature He I λ10830 values were available and utilized. Paper I provides a table with that breakdown by target. The MODS spectra for some targets showed clear signs of high excitation and other dynamics, which do not conform to the general H II region assumptions our model rests upon. They are thus less suitable for our analysis, and LUCI observations were not always pursued. There were two such targets: WISEA J120503.54+455151.0 and SHOC 133. Similarly, a LUCI observation was not pursued for HSC J2314+0154, which was too faint and lacked a He I λ4026 detection (see above). A LUCI spectrum was also not pursued for I Zw 18 NW, as opposed to I Zw 18 SE, where I Zw 18 NW has been shown to be unsuitable for helium abundance determinations due to strong underlying absorption, Wolf–Rayet (W-R) stars, and a strong temperature gradient, as well as significant Galactic Na I absorption for He I λ5876 (Y. I. Izotov et al. 1999). Finally, the morphology of one target,

Table 1
χ^2 Excluded Targets

Object	χ^2	95% CL	d.o.f.	[Fe v]
HS 0811+4913	30.4	23.7	14	
HS 0837+4717	63.1	25.0	15	✓
J0519+0007	24.6	23.7	14	✓
LEDA 101527	22.3	21.0	12	✓
Mrk 36	23.5	19.7	11	✓
VCC 1744	42.6	26.3	16	
WJ0851+5841	79.5	21.0	12	✓

Note. The above targets are excluded on the basis of their best-fit χ^2 (second column) exceeding the 95% CL for the number of degrees of freedom available for each target. Targets with [Fe v] λ4227 detections are marked. [Fe v] emission indicates unexpectedly high ionization states not attributable to photoionization by massive stars. As such, these targets may not be expected to be well fit by our model.

HS 2236+1344, shows a double knot structure without a reliable He I λ10830 measurement. Therefore, lacking He I λ10830, five targets were excluded from our He analysis dataset (one of which also lacked He I λ4026).

Paper I provides a list of all targets observed for the the LBT Y_p Project. Applying the above criteria yielded a starting dataset of 54 targets for He abundance analysis and, after testing for statistical reliability and flagging for potential systematic biases, determining Y_p.

4. χ^2 Goodness-of-fit Testing

In evaluating the results from our sample, we first perform a 95% confidence level (CL) χ^2 cut for statistical reliability. For 15 degrees of freedom (for example, for 24 line ratios and nine fit parameters), we require $\chi^2 < 25.0$. Assuming reasonable flux uncertainties (not systematically underestimated), targets with best-fit (i.e., minimized) χ^2 values exceeding the 95% CL for their number of degrees of freedom are very likely not statistically reliable, and it is probable that systematic errors are undermining their returned physical conditions. This could be because of systematic effects in the measurements (e.g., Na I absorption), systematic errors in the model, or a physical system with conditions not captured by the model (e.g., a supernova remnant and very high excitation states).

From our starting dataset of 54 observations, seven have best-fit χ^2 values that exceed the 95% CL goodness-of-fit test, based on their number of degrees of freedom (which varies by target). These seven targets are listed in Table 1, along with the model-determined χ^2, the 95% CL value for χ^2, and the number of degrees of freedom. This leaves 47 targets, given in Table 2, that pass our standard 95% CL χ^2 cut for statistical reliability. In the absence of systematic errors and based on random error alone, one would expect three targets to exceed the 95% threshold. However, some of our targets clearly exhibit systematic effects not captured by our model.

Five of the seven targets in Table 1 exhibited emission lines characteristic of unexpectedly high ionization states, such as [Fe v] λ4227 and, in some cases, [Ne v] λ3425, which are not typically expected in low-metallicity H II regions. These types of objects have been identified as extreme emission line galaxies (EELGs), as discussed by D. A. Berg et al. (2021), and present the challenge of identifying a source of the high ionizing energy photons (which cannot be produced through standard photoionization). Since these high ionization states may indicate the presence of a supernova remnant or another source of ionization not attributable to photoionization by massive stars, they may not be well fit by our model. However, [Fe v] λ4227 was found in seven other targets that did qualify, and we found no clear relationship between the strength of the [Fe v] λ4227 emission line and the goodness of fit or the derived helium abundance. Furthermore, it is worthy of note that even the strongest detection of [Fe v] λ4227 is less than 0.5% of Hβ. Thus, we did not exclude or flag targets based on the presence or strength of [Fe v] λ4227. At present, the detection of [Fe v] λ4227 is considered evidence of a minor contaminant.

Multiple targets also exhibit very broad multicomponent wings on Hα and [O III] λ5007 and, extending with decreasing prominence, to Hβ, Hγ, and [O III] λ4959. These wings are very challenging to fit, raise questions about which components should be included in the measured flux for our analysis, and indicate complicated kinematic structures, which are not accounted for in our model. Multiple targets also exhibit clear W-R features, where the presence of W-R stars may contribute to a poor model fit. Additionally, the line profiles for several targets are also significantly skewed and asymmetric. It is not clear what the cause of that asymmetry is, but it undermines the reliability of the measured fluxes.

Of the seven targets exceeding their 95% threshold, two have features that clearly signal that we would not expect our model to apply to the physical conditions underlying their emission. HS 0837+4717 exhibits extremely strong wings on its strong emission lines (the strongest in our sample), as well as weak [Fe v] emission, while for Mrk 36, the emission line profiles are very strongly skewed. In addition to those two, whose spectra are clearly discrepant and ill-suited for analysis using standard H II region modeling, three other targets show weaker cases of the above pathologies (that is, characteristics that are pathological for our purposes). J0519+0007, LEDA 101527, WISEA J085115.60+584055.7, and the aforementioned Mrk 36 include [Fe v] emission (weaker for LEDA 101527 and Mrk 36). If we count all five of those targets as likely to result in poor model fits due to their anomalies, we are left with two targets—HS 0811+4913 and VCC 1744—excluded by the χ^2 test. This is in line with what would be expected based on random errors.

4.1. Excluded Emission Lines

In determining the best-fit parameter solution for each target, we examine the distribution of χ^2 values for our set of emission lines. Large χ^2 contributions from a given line may indicate a systematic effect undermining the accuracy and reliability of its measured flux. Further evaluation is required to determine whether removing that emission line from our analysis is justified.

In particular, the Paschen sequence of lines, P8–P15, is observed in the NIR, where telluric contamination is common. Water vapor absorption lines may be imprinted on our emission lines, as may the very strong night sky emission lines, which must be fit and subtracted. As a result, Paschen lines may be decreased due to absorption features, and the accuracy of a given Paschen line measurement may be reduced by the night sky emission line subtraction. Our error function for estimating the uncertainty on our measured fluxes varies with wavelength and is constructed to capture the increased

Table 2
Physical Parameters and He^+/H^+ Abundance Best-fit Solutions for the Qualifying Dataset

Object	$y^+ = He^+/H^+$	n_e (cm^{-3})	a_{He} (Å)	τ	T_e (K)	$C(H\beta)$	a_H (Å)	a_P (Å)	$\xi \times 10^4$	T(O III) (K)	χ^2	95% CL	d.o.f.
Final Dataset Not Flagged													
DDO 68	$0.07706^{+0.00280}_{-0.00208}$	58^{+18}_{-17}	$0.20^{+0.14}_{-0.11}$	$0.00^{+0.10}_{-0.00}$	$18{,}500^{+1400}_{-1400}$	$0.07^{+0.02}_{-0.02}$	$0.39^{+0.14}_{-0.16}$	$0.00^{+0.13}_{-0.00}$	0^{+6}_{-0}	18,900	16.4	19.7	11
HS 0029+1748	$0.07869^{+0.00131}_{-0.00133}$	148^{+35}_{-31}	$0.11^{+0.08}_{-0.08}$	$0.52^{+0.29}_{-0.27}$	$12{,}600^{+1000}_{-900}$	$0.27^{+0.02}_{-0.02}$	$1.41^{+0.16}_{-0.16}$	$0.93^{+0.21}_{-0.21}$	⋯	12,800	17.4	23.7	14
HS 0122+0743	$0.08214^{+0.00145}_{-0.00137}$	172^{+28}_{-23}	$0.15^{+0.12}_{-0.12}$	$1.57^{+0.35}_{-0.30}$	$17{,}900^{+1200}_{-1200}$	$0.29^{+0.01}_{-0.02}$	$0.65^{+0.19}_{-0.17}$	$1.07^{+0.31}_{-0.32}$	0^{+3}_{-0}	17,800	13.7	22.4	13
HS 0134+3415	$0.07777^{+0.00100}_{-0.00109}$	271^{+52}_{-43}	$0.12^{+0.09}_{-0.09}$	$1.72^{+0.31}_{-0.31}$	$12{,}900^{+900}_{-900}$	$0.16^{+0.01}_{-0.01}$	$1.06^{+0.13}_{-0.15}$	$0.00^{+0.24}_{-0.00}$	⋯	16,300	14.3	26.3	16
HS 1353+4706	$0.08036^{+0.00111}_{-0.00113}$	1^{+1}_{-1}	$0.18^{+0.13}_{-0.13}$	$0.37^{+0.24}_{-0.12}$	$17{,}700^{+900}_{-1200}$	$0.17^{+0.01}_{-0.02}$	$0.57^{+0.20}_{-0.23}$	$0.00^{+0.30}_{-0.00}$	0^{+3}_{-0}	19,600	17.7	23.7	14
HS 1442+4250	$0.08327^{+0.00295}_{-0.00323}$	30^{+12}_{-9}	$0.28^{+0.12}_{-0.11}$	$0.00^{+0.11}_{-0.00}$	$17{,}400^{+600}_{-800}$	$0.09^{+0.02}_{-0.02}$	$0.92^{+0.19}_{-0.18}$	$0.15^{+0.30}_{-0.15}$	54^{+32}_{-21}	16,600	14.1	22.4	13
I Zw 18 SE	$0.08243^{+0.00260}_{-0.00278}$	7^{+11}_{-7}	$0.31^{+0.09}_{-0.09}$	$0.18^{+0.34}_{-0.18}$	$17{,}500^{+1400}_{-1500}$	$0.13^{+0.03}_{-0.02}$	$1.12^{+0.13}_{-0.13}$	$0.14^{+0.35}_{-0.14}$	14^{+25}_{-11}	18,400	9.1	21.0	12
J0133+1342	$0.08042^{+0.00206}_{-0.00194}$	59^{+20}_{-15}	$0.33^{+0.09}_{-0.09}$	$0.54^{+0.33}_{-0.28}$	$15{,}800^{+1200}_{-1300}$	$0.18^{+0.02}_{-0.02}$	$0.75^{+0.14}_{-0.14}$	$0.56^{+0.22}_{-0.24}$	16^{+38}_{-16}	17,500	17.1	25.0	15
J0807+3414	$0.08725^{+0.00196}_{-0.00241}$	250^{+39}_{-34}	$0.23^{+0.13}_{-0.15}$	$6.20^{+0.58}_{-0.64}$	$16{,}800^{+1200}_{-900}$	$0.17^{+0.02}_{-0.01}$	$0.16^{+0.18}_{-0.16}$	$0.00^{+0.53}_{-0.00}$	21^{+20}_{-14}	17,400	10.0	25.0	15
J1044+0353	$0.07844^{+0.00190}_{-0.00206}$	163^{+29}_{-22}	$0.13^{+0.10}_{-0.11}$	$1.55^{+0.36}_{-0.33}$	$18{,}100^{+1100}_{-1300}$	$0.15^{+0.02}_{-0.02}$	$0.84^{+0.16}_{-0.14}$	$0.78^{+0.39}_{-0.41}$	11^{+13}_{-7}	19,600	19.2	23.7	14
J1148+2546	$0.08399^{+0.00214}_{-0.00168}$	145^{+29}_{-25}	$0.40^{+0.07}_{-0.07}$	$2.40^{+0.40}_{-0.41}$	$14{,}900^{+1100}_{-900}$	$0.20^{+0.02}_{-0.02}$	$0.90^{+0.14}_{-0.13}$	$0.83^{+0.21}_{-0.23}$	17^{+55}_{-17}	14,300	10.4	22.4	13
J1323–01325	$0.08480^{+0.00210}_{-0.00215}$	67^{+16}_{-14}	$0.26^{+0.08}_{-0.10}$	$2.51^{+0.35}_{-0.38}$	$16{,}600^{+1100}_{-1000}$	$0.10^{+0.02}_{-0.01}$	$0.76^{+0.13}_{-0.13}$	$0.02^{+0.39}_{-0.02}$	32^{+29}_{-18}	18,400	8.9	23.7	14
J1331+4151	$0.07690^{+0.00136}_{-0.00128}$	62^{+21}_{-17}	$0.10^{+0.08}_{-0.07}$	$1.01^{+0.37}_{-0.32}$	$14{,}800^{+1200}_{-1200}$	$0.15^{+0.02}_{-0.02}$	$0.79^{+0.10}_{-0.11}$	$0.74^{+0.17}_{-0.17}$	0^{+18}_{-0}	16,500	12.5	21.0	12
J2104–0035	$0.08267^{+0.00580}_{-0.00581}$	11^{+18}_{-9}	$0.16^{+0.23}_{-0.16}$	$0.45^{+0.59}_{-0.41}$	$18{,}800^{+1900}_{-2200}$	$0.13^{+0.04}_{-0.04}$	$1.27^{+0.31}_{-0.31}$	$0.49^{+0.77}_{-0.49}$	28^{+77}_{-28}	18,900	9.6	21.0	12
J2213+1722	$0.07787^{+0.00144}_{-0.00170}$	1^{+6}_{-1}	$0.23^{+0.08}_{-0.08}$	$0.40^{+0.49}_{-0.23}$	$14{,}200^{+1300}_{-1400}$	$0.10^{+0.02}_{-0.02}$	$1.09^{+0.13}_{-0.13}$	$0.86^{+0.34}_{-0.34}$	⋯	16,700	18.5	21.0	12
KUG 1138+327	$0.08836^{+0.00132}_{-0.00186}$	14^{+9}_{-8}	$0.44^{+0.04}_{-0.05}$	$0.00^{+0.12}_{-0.00}$	$15{,}700^{+400}_{-700}$	$0.04^{+0.01}_{-0.01}$	$1.28^{+0.10}_{-0.10}$	$0.00^{+0.11}_{-0.00}$	49^{+37}_{-19}	14,800	16.0	19.7	11
LEDA 2790884	$0.08615^{+0.00259}_{-0.00304}$	61^{+39}_{-33}	$0.25^{+0.14}_{-0.15}$	$0.05^{+0.29}_{-0.05}$	$16{,}800^{+1100}_{-1300}$	$0.11^{+0.02}_{-0.02}$	$0.88^{+0.22}_{-0.21}$	$0.00^{+0.40}_{-0.00}$	70^{+91}_{-33}	18,200	15.1	22.4	13
Leo P	$0.08386^{+0.00222}_{-0.00241}$	33^{+18}_{-10}	$0.41^{+0.19}_{-0.18}$	$0.00^{+0.27}_{-0.00}$	$17{,}900^{+1000}_{-1600}$	$0.10^{+0.02}_{-0.02}$	$0.12^{+0.19}_{-0.12}$	$0.00^{+0.34}_{-0.00}$	0^{+5}_{-0}	17,200	10.7	22.4	13
SBS 0335–052E	$0.08470^{+0.00250}_{-0.00194}$	69^{+13}_{-12}	$0.30^{+0.05}_{-0.05}$	$4.44^{+0.50}_{-0.43}$	$21{,}100^{+1200}_{-1300}$	$0.21^{+0.02}_{-0.02}$	$0.62^{+0.07}_{-0.07}$	$0.74^{+0.22}_{-0.23}$	1^{+2}_{-1}	20,900	20.9	21.0	12
SBS 0926+606	$0.08043^{+0.00182}_{-0.00188}$	121^{+44}_{-35}	$0.27^{+0.11}_{-0.11}$	$0.43^{+0.39}_{-0.41}$	$11{,}400^{+1100}_{-1000}$	$0.14^{+0.02}_{-0.02}$	$1.45^{+0.14}_{-0.14}$	$0.46^{+0.34}_{-0.34}$	⋯	11,400	5.8	16.9	9
SBS 0940+544	$0.08146^{+0.00255}_{-0.00321}$	89^{+30}_{-22}	$0.32^{+0.26}_{-0.28}$	$0.48^{+0.39}_{-0.40}$	$16{,}800^{+1700}_{-1800}$	$0.14^{+0.03}_{-0.02}$	$0.82^{+0.25}_{-0.27}$	$0.00^{+0.80}_{-0.00}$	19^{+38}_{-19}	19,200	10.1	23.7	14
SBS 0946+558	$0.08392^{+0.00131}_{-0.00128}$	43^{+15}_{-13}	$0.20^{+0.07}_{-0.07}$	$0.15^{+0.25}_{-0.15}$	$15{,}100^{+1000}_{-1000}$	$0.21^{+0.01}_{-0.01}$	$1.19^{+0.10}_{-0.11}$	$1.23^{+0.09}_{-0.11}$	0^{+13}_{-0}	13,400	11.0	22.4	13
SBS 0948+532	$0.08219^{+0.00122}_{-0.00127}$	167^{+37}_{-33}	$0.38^{+0.07}_{-0.07}$	$0.93^{+0.30}_{-0.30}$	$11{,}800^{+800}_{-800}$	$0.15^{+0.02}_{-0.02}$	$0.93^{+0.17}_{-0.17}$	$0.61^{+0.25}_{-0.24}$	⋯	12,500	15.5	23.7	14
SBS 1030+583	$0.07953^{+0.00337}_{-0.00138}$	40^{+10}_{-11}	$0.36^{+0.05}_{-0.04}$	$0.00^{+0.10}_{-0.00}$	$16{,}100^{+700}_{-800}$	$0.08^{+0.01}_{-0.02}$	$1.32^{+0.11}_{-0.09}$	$0.73^{+0.16}_{-0.21}$	2^{+18}_{-2}	15,500	18.1	18.3	10
SBS 1135+581	$0.08256^{+0.00074}_{-0.00072}$	1^{+3}_{-1}	$0.15^{+0.06}_{-0.06}$	$0.76^{+0.33}_{-0.17}$	$12{,}400^{+700}_{-700}$	$0.22^{+0.01}_{-0.01}$	$1.25^{+0.10}_{-0.10}$	$1.17^{+0.08}_{-0.09}$	⋯	12,300	15.4	22.4	13
SBS 1152+579	$0.08183^{+0.00111}_{-0.00098}$	409^{+64}_{-49}	$0.22^{+0.05}_{-0.06}$	$3.87^{+0.49}_{-0.37}$	$15{,}000^{+700}_{-1100}$	$0.25^{+0.01}_{-0.02}$	$0.46^{+0.09}_{-0.09}$	$0.70^{+0.11}_{-0.13}$	0^{+17}_{-0}	15,500	15.2	23.7	14
SBS 1159+545	$0.07813^{+0.00135}_{-0.00122}$	171^{+29}_{-24}	$0.15^{+0.08}_{-0.07}$	$1.36^{+0.36}_{-0.28}$	$16{,}500^{+1100}_{-1200}$	$0.13^{+0.01}_{-0.02}$	$0.09^{+0.12}_{-0.09}$	$0.15^{+0.26}_{-0.15}$	0^{+8}_{-0}	17,600	11.4	23.7	14
SBS 1211+540	$0.07761^{+0.00237}_{-0.00157}$	62^{+15}_{-13}	$0.27^{+0.10}_{-0.09}$	$0.00^{+0.12}_{-0.00}$	$15{,}900^{+700}_{-800}$	$0.07^{+0.02}_{-0.02}$	$1.69^{+0.15}_{-0.16}$	$0.84^{+0.27}_{-0.31}$	5^{+22}_{-5}	17,400	10.8	23.7	14
SBS 1249+493	$0.07686^{+0.00194}_{-0.00159}$	53^{+20}_{-15}	$0.22^{+0.08}_{-0.07}$	$0.98^{+0.43}_{-0.32}$	$15{,}700^{+1300}_{-1400}$	$0.16^{+0.02}_{-0.03}$	$1.23^{+0.12}_{-0.11}$	$1.21^{+0.36}_{-0.41}$	0^{+29}_{-0}	15,900	8.9	21.0	12
SBS 1331+493	$0.08275^{+0.00077}_{-0.00096}$	65^{+9}_{-8}	$0.17^{+0.08}_{-0.08}$	$0.00^{+0.06}_{-0.00}$	$17{,}000^{+400}_{-600}$	$0.13^{+0.01}_{-0.01}$	$0.67^{+0.15}_{-0.17}$	$0.00^{+0.04}_{-0.00}$	0^{+1}_{-0}	15,700	21.8	22.4	13
SBS 1415+437	$0.07870^{+0.00155}_{-0.00170}$	101^{+16}_{-12}	$0.31^{+0.06}_{-0.07}$	$0.00^{+0.06}_{-0.00}$	$17{,}300^{+500}_{-700}$	$0.11^{+0.01}_{-0.01}$	$0.75^{+0.13}_{-0.12}$	$0.00^{+0.10}_{-0.00}$	52^{+22}_{-15}	15,900	9.8	21.0	12
SBS 1420+544	$0.08421^{+0.00156}_{-0.00176}$	324^{+50}_{-42}	$0.16^{+0.08}_{-0.08}$	$4.95^{+0.46}_{-0.46}$	$17{,}300^{+1200}_{-1100}$	$0.17^{+0.01}_{-0.01}$	$0.08^{+0.15}_{-0.08}$	$0.00^{+0.33}_{-0.00}$	15^{+12}_{-8}	17,900	11.6	23.7	14
SBS 1437+370	$0.08237^{+0.00155}_{-0.00151}$	93^{+19}_{-16}	$0.29^{+0.06}_{-0.07}$	$0.00^{+0.10}_{-0.00}$	$13{,}500^{+600}_{-600}$	$0.12^{+0.01}_{-0.01}$	$1.15^{+0.10}_{-0.09}$	$0.89^{+0.18}_{-0.19}$	⋯	13,900	6.6	25.0	15
UGC 4483	$0.07847^{+0.00281}_{-0.00188}$	29^{+12}_{-11}	$0.36^{+0.10}_{-0.10}$	$0.00^{+0.19}_{-0.00}$	$17{,}300^{+1000}_{-1200}$	$0.13^{+0.01}_{-0.02}$	$1.07^{+0.15}_{-0.16}$	$1.30^{+0.36}_{-0.40}$	1^{+11}_{-1}	17,300	9.4	19.7	11
UGC 5541	$0.08004^{+0.00264}_{-0.00258}$	11^{+11}_{-10}	$0.43^{+0.09}_{-0.09}$	$0.00^{+0.11}_{-0.00}$	$15{,}900^{+600}_{-800}$	$0.09^{+0.02}_{-0.02}$	$0.86^{+0.11}_{-0.12}$	$0.41^{+0.27}_{-0.29}$	15^{+24}_{-15}	15,400	20.7	22.4	13
UM 133	$0.08434^{+0.00250}_{-0.00221}$	38^{+13}_{-11}	$0.40^{+0.09}_{-0.09}$	$0.00^{+0.14}_{-0.00}$	$16{,}400^{+600}_{-900}$	$0.15^{+0.01}_{-0.02}$	$0.77^{+0.12}_{-0.11}$	$0.83^{+0.29}_{-0.28}$	23^{+21}_{-13}	15,700	10.4	23.7	14
UM 161	$0.07987^{+0.00165}_{-0.00130}$	110^{+28}_{-22}	$0.30^{+0.12}_{-0.11}$	$1.39^{+0.33}_{-0.32}$	$14{,}300^{+1100}_{-1000}$	$0.23^{+0.02}_{-0.02}$	$0.68^{+0.15}_{-0.14}$	$0.00^{+0.49}_{-0.00}$	0^{+50}_{-0}	15,600	7.1	25.0	15
UM 461	$0.07870^{+0.00140}_{-0.00091}$	94^{+22}_{-20}	$0.10^{+0.08}_{-0.07}$	$3.32^{+0.39}_{-0.39}$	$14{,}100^{+900}_{-900}$	$0.22^{+0.01}_{-0.01}$	$0.66^{+0.13}_{-0.16}$	$0.39^{+0.20}_{-0.27}$	0^{+47}_{-0}	16,500	15.6	23.7	14
WJ1136+4709	$0.08489^{+0.00190}_{-0.00168}$	42^{+12}_{-10}	$0.23^{+0.08}_{-0.08}$	$0.18^{+0.25}_{-0.18}$	$17{,}000^{+1000}_{-1000}$	$0.14^{+0.02}_{-0.02}$	$0.53^{+0.09}_{-0.09}$	$0.85^{+0.18}_{-0.22}$	3^{+12}_{-3}	15,400	18.8	22.4	13
WJ1327+4022	$0.07532^{+0.00182}_{-0.00145}$	37^{+19}_{-14}	$0.11^{+0.13}_{-0.11}$	$0.34^{+0.34}_{-0.30}$	$14{,}700^{+1300}_{-1400}$	$0.11^{+0.02}_{-0.02}$	$0.94^{+0.17}_{-0.16}$	$0.27^{+0.31}_{-0.27}$	0^{+33}_{-0}	17,200	5.9	18.3	10
WJ2310–0211	$0.08640^{+0.00170}_{-0.00198}$	198^{+25}_{-28}	$0.35^{+0.06}_{-0.06}$	$4.98^{+0.42}_{-0.52}$	$17{,}300^{+1000}_{-900}$	$0.21^{+0.02}_{-0.01}$	$0.78^{+0.11}_{-0.10}$	$0.00^{+0.25}_{-0.00}$	14^{+10}_{-9}	16,400	10.9	19.7	11

Table 2
(Continued)

Object	$y^+ = He^+/H^+$	n_e (cm^{-3})	a_{He} (Å)	τ	T_e (K)	$C(H\beta)$	a_H (Å)	a_P (Å)	$\xi \times 10^4$	T(O III) (K)	χ^2	95% CL	d.o.f.
Final Dataset with Flags													
AGC 198691	$0.08076^{+0.00572}_{-0.00356}$	237^{+267}_{-237}	$0.37^{+0.20}_{-0.18}$	$0.30^{+0.97}_{-0.30}$	$14{,}000^{+2800}_{-2700}$	$0.11^{+0.02}_{-0.06}$	$1.65^{+0.28}_{-0.27}$	$0.92^{+0.68}_{-0.89}$	0^{+585}_{-0}	20,000	10.8	12.6	6
HS 1028+3843	$0.08786^{+0.00118}_{-0.00079}$	341^{+37}_{-34}	$0.02^{+0.11}_{-0.02}$	$13.25^{+0.65}_{-0.71}$	$17{,}300^{+800}_{-800}$	$0.24^{+0.01}_{-0.01}$	$0.00^{+0.04}_{-0.00}$	$0.00^{+0.09}_{-0.00}$	0^{+1}_{-0}	16,500	17.4	23.7	14
HS 1222+3741	$0.09171^{+0.00332}_{-0.00396}$	95^{+23}_{-17}	$0.61^{+0.07}_{-0.08}$	$0.00^{+0.30}_{-0.00}$	$17{,}400^{+800}_{-1400}$	$0.02^{+0.02}_{-0.02}$	$1.62^{+0.11}_{-0.11}$	$0.00^{+0.20}_{-0.00}$	37^{+47}_{-14}	15,000	5.8	19.7	11
J0118+3512	$0.07520^{+0.00204}_{-0.00223}$	54^{+33}_{-21}	$0.16^{+0.14}_{-0.15}$	$0.00^{+0.13}_{-0.00}$	$13{,}000^{+1200}_{-1300}$	$0.25^{+0.02}_{-0.02}$	$0.93^{+0.18}_{-0.17}$	$1.41^{+0.53}_{-0.56}$	⋯	17,500	10.3	19.7	11
Mrk 71	$0.08369^{+0.00108}_{-0.00092}$	213^{+28}_{-25}	$0.24^{+0.07}_{-0.07}$	$2.30^{+0.37}_{-0.30}$	$18{,}500^{+900}_{-1000}$	$0.25^{+0.01}_{-0.01}$	$0.64^{+0.12}_{-0.13}$	$0.35^{+0.21}_{-0.22}$	0^{+1}_{-0}	15,800	21.8	23.7	14
UGC 6456	$0.08375^{+0.00252}_{-0.00281}$	100^{+27}_{-17}	$0.78^{+0.18}_{-0.20}$	$0.00^{+0.35}_{-0.00}$	$16{,}600^{+700}_{-1400}$	$0.15^{+0.01}_{-0.02}$	$1.09^{+0.19}_{-0.19}$	$0.74^{+0.36}_{-0.37}$	13^{+30}_{-12}	15,500	20.7	22.4	13

uncertainty in the NIR. Nevertheless, a Paschen line may be systematically decreased due to atmospheric absorption, and subtraction of the night sky emission lines may affect the local continuum and the line.

Given those effects, when a given Paschen line is strongly discrepant compared to the rest of the Paschen sequence, we remove it from our analysis. After correcting for reddening and underlying absorption, each of which depends on a single model parameter, the ratios of the theoretical fluxes for the Paschen lines only vary weakly with temperature. The density dependence is almost negligible. At the higher orbital excitation levels ($n \geqslant 8$) for the utilized Paschen lines, the contributions from neutral hydrogen collisional excitation are relatively small, and those contributions do not decrease substantially as the level increases (i.e., they are roughly constant across these higher Paschen lines). Therefore, a Paschen line that is clearly discrepant from the others is likely contaminated, and removing it is justified. For example, for J1323–01325, the χ^2 contribution from P9 λ9230 was 16.9 (the next-highest χ^2 contribution was 1.2), and removing P9 λ9230 reduced the total χ^2 from 27.3 to 8.9.

The tight wavelength spacing and strong underlying absorption of the higher Balmer lines, H9–H12, also make accurately measuring their fluxes challenging. Paralleling the explanation above for the Paschen series, the theoretical flux ratios are also well anchored. Correspondingly, similar to the Paschen series, though less common in frequency, we also remove higher Balmer lines that are clearly discrepant compared to the rest of the Balmer sequence, especially when the ability to accurately fit the local continuum is compromised.

However, we do not remove any of our "core" lines from our analysis based on their χ^2 values. The core lines (line ratios) are He I $\lambda\lambda$4026, 4471, 5876, 6678, 7065, and 10830; the Balmer lines, Hα, Hγ, and Hδ; and the blended line He I λ3889 + H8. These core lines are the heart of our model, providing the strongest diagnostic power for determining the physical conditions (model parameters) of the H II region (K. A. Olive & E. D. Skillman 2001, 2004; E. Aver et al. 2010, 2011, 2012, 2013, 2015). With the exception of He I λ10830, they are also isolated lines located in a region of the spectrum with the highest spectral sensitivity and with many fewer night sky emission features and telluric absorption bands (compared to the NIR).

The only cases where a core line is removed from our analysis is the (rare) situation where we can see clear evidence of a systematic effect significantly undermining the reliability of the measured flux for that line. These come in three cases: (1) atmospheric molecular oxygen A- or B-band absorption impacting He I λ6678, (2) galactic Na I absorption and/or night sky emission coincident with He I λ5876, and (3) very strong, broad emission wings on Hα that are stronger and broader than would be expected based on [O III] λ5007 or Hβ.

The atmospheric A and B O_2 absorption bands are easily identified in our spectra, with a clear drop in the continuum level. For galaxies with redshift ranges of $z = 0.120$–0.134 and $z = 0.025$–0.039, He I λ6678 will fall within the A or B bands, respectively. In those cases, the measured He I λ6678 flux will be systematically decreased and is not accurate. There are two targets where He I λ6678 is excluded for this reason: HS 1028+3843 ($z = 0.0295$) and HS 1353+4706 ($z = 0.0281$). As a validation of our methodology of determining the best-fit parameters by minimizing χ^2 (see Section 2), it should be noted that the returned χ^2 contributions from He I λ6678 for these targets (prior to removing He I λ6678) were very large—32.4 for HS 1028+3843 and 9.6 for HS 1353+4706—signaling the very strong disagreement of the measured He I λ6678 flux with the predicted flux. That predicted He I λ6678 flux is, in effect, determined by the other He emission lines, since their combined χ^2 minimization is what determines the model parameters. As such, for these two targets, the measured He I λ6678 flux is in strong disagreement with all of the other He emission lines for any set of model parameters. As expected, the measured He I λ6678 flux for these two targets was also significantly lower than the model's predicted value. Upon removing He I λ6678, the total χ^2 for HS 1028+3843 dropped from 64.7 to 17.4, and it dropped from 31.3 to 17.7 for HS 1353+4706. These dramatic decreases highlight just how extreme the discrepancy between the measured He I λ6678 flux was with all of the other He emission lines, as well as highlighting the diagnostic utility of the χ^2 distribution.

Galactic Na I λ5889.95 and Na I λ5895.92 absorption will decrease the observed He I λ5876 flux for redshifts of 0.00243 and 0.00344 with a previously identified conservative range of $\pm$0.00033 (K. A. Olive & E. D. Skillman 2004; E. Aver et al. 2022). The magnitude of the decrease will vary and may be negligible. At the same time, the same atmospheric Na I night sky emission lines will also overlay He I λ5876, creating the potential for a systematic error to be introduced from the night sky subtraction. For two of our targets, I Zw 18 SE with $z = 0.002505$ and LEDA 2790884 with $z = 0.002425$, not only do their redshifts fall within the Na I absorption range, but the spectrum showed evidence for the absorption in the local continuum for He I λ5876. This finding was bolstered by the measured He I λ5876 flux being significantly lower than the model's predicted value, as would be expected for Na I absorption. Furthermore, this result is consistent with the relatively large foreground Galactic extinction for each target: $A_V = 0.091$ for I Zw 18 SE and $A_V = 0.126$ for LEDA 2790884 (E. F. Schlafly & D. P. Finkbeiner 2011). Therefore, He I λ5876 was removed from our analysis for I Zw 18 SE and LEDA 2790884.

Four targets, HS 1442+4250, SDSS J210455.31–003522.2, LEDA 2790884, and SBS 1415+437, show very strong, broad emission wings for Hα, and that, unusually, are stronger and broader than would be expected based on [O III] λ5007 or Hβ. This behavior is not expected, lacking an obvious explanation, and it may indicate complicated kinematics within the H II region or potential Raman scattering (W. J. Henney 2021). Regardless, it is not clear what portion of the Hα emission should be included for comparison to the predicted model flux. Furthermore, very strong wings on Hα pose significant challenges for accurately fitting and measuring its emission line flux with its multiple components. Therefore, Hα is not reliable for these four galaxies and was excluded for our analysis. Supporting the finding that Hα is anomalous and unreliable for analysis with our model, all four of these galaxies showed unusually large χ^2 contributions from Hα, indicating, in effect, significant disagreement between Hα and all of the other H emission lines for any set of model parameters. Upon removing Hα, all of the other Balmer lines that had been in tension snapped into good agreement with their measured values for the revised set of best-fit model parameters. It is also worth noting that, though Hα was in strong disagreement with the other lines and contributed a very

Table 3
Excluded Lines by Target

Object	Excluded Lines
AGC 198691	…
DDO 68	H9
HS 0029+1748	P9, P10
HS 0122+0743	P9, P10
HS 0134+3415	…
HS 1028+3843	He I λ6678
HS 1222+3741	H12
HS 1353+4706	He I λ6678
HS 1442+4250	Hα
I Zw 18 SE	He I λ5876, P8, P11
J0118+3512	…
J0133+1342	…
J0807+3414	…
J1044+0353	P8
J1148+2546	P9, P12
J1323–01325	P9
J1331+4151	He I λ4922, H9, P9
J2104–0035	Hα, P8
J2213+1722	…
KUG 1138+327	He I λ4922, H12, P13, P15
LEDA 2790884	He I λ5876, Hα
Leo P	H9
Mrk 71	P10
SBS 0335–052E	P9, P10, P14
SBS 0926+606	He I λ4922, H12, P8, P9, P10
SBS 0940+544	…
SBS 0946+558	He I λ4922, P14
SBS 0948+532	H9, P12
SBS 1030+583	P13, P14
SBS 1135+581	He I λ4922, P8, P14
SBS 1152+579	P9
SBS 1159+545	P8
SBS 1211+540	P10
SBS 1249+493	…
SBS 1331+493	P8, P9
SBS 1415+437	Hα, H9, P8
SBS 1420+544	P8
SBS 1437+370	P14
UGC 4483	H9, P8
UGC 5541	…
UGC 6456	P13
UM 133	…
UM 161	…
UM 461	P9
WJ1136+4709	He I λ4922, P14
WJ1327+4022	H9, P8, P9
WJ2310–0211	H9, P9, P13, P15

large χ^2, the same was not true of He I λ6678, He I λ7065, or the Paschen series lines. This rules out a potential MODS red-versus-blue channel calibration issue as the source of the discrepant Hα.

Table 3 provides the full list of the excluded lines for each target.

4.2. χ^2 Qualifying Fraction Comparison

Compared to previous analyses, the fraction of our dataset passing the χ^2 cut is a dramatic improvement compared to previous studies. Of our 54 targets, 47 qualify, equating to 87%. Though, ideally, 95% would have passed, as discussed above (Section 4), systematic effects in our spectra and/or that are fundamentally unaccounted for in our H II region emission modeling for a subset of our targets means that we should not expect 95% to qualify. Furthermore, an 87% qualifying fraction is a vast improvement upon previous analyses. In E. Aver et al. (2012), the χ^2 qualifying fraction using the HeBCD dataset from Y. I. Izotov et al. (2007) was only 36% (25 of 70), a very unsettling result. Restricting to the subset of generally brighter HeBCD targets that included He I λ10830 observations from Y. I. Izotov et al. (2014) increased that qualifying fraction to 61% (19 of 31), but that was still much lower than would be expected.

Using different criteria (see Paper I), not χ^2 testing, the qualification rate in T. Hsyu et al. (2020) varies, but for their preferred sample criteria applied to the HeBCD dataset with He I λ10830 observations, the qualification rate is 29%. For the qualification rates quoted from T. Hsyu et al. (2020), some of the nonqualifying targets are excluded based on their model parameter values (where we flag such targets), but the majority of the excluded targets are based on the T. Hsyu et al. (2020) criteria designed to play a similar role to a χ^2 cut. For their combination of the optical-only HeBCD, PHLEK, and Sloan Digital Sky Survey (SDSS) observations, the qualifying rate decreases to 7%. Relaxing their criteria allows more targets to qualify, but, for their combined dataset, the highest qualifying rate T. Hsyu et al. (2020) find is still only 50%.

In A. Matsumoto et al. (2022), they combine their Subaru dataset with the sample from T. Hsyu et al. (2020) (Sample 1). For their Subaru dataset, the qualification rate is 50% (5 of 10), using the same criteria as T. Hsyu et al. (2020) (again see Paper I). H. Yanagisawa et al. (2026) add 27 Subaru targets to the Subaru and T. Hsyu et al. (2020) datasets from A. Matsumoto et al. (2022). Applying the T. Hsyu et al. (2020) criteria to those 27, the qualifying rate is 41% (11 of 27).

High best-fit χ^2 values indicate one of three things, or a combination thereof: (1) systematic errors with the measured fluxes, (2) systematic errors in the model, and/or (3) the reported uncertainties for the measured fluxes are underestimated. Disentangling the source is challenging and impeded by the lack of information about various steps in the observational and/or measurement process, as well as the potential systematic errors in the atomic data underpinning the model equations.

Therefore, one of the major goals of the LBT Y_p Project was to collect our own high-quality, high-SNR observations to produce a uniformly observed dataset (see Paper I), carefully reduce those observations ourselves (see Papers II and III), measure the emission line fluxes ourselves (see Papers II and III), and apply our own error model for calculating the flux uncertainties (see Papers I and II). That dataset, the LBT Y_p Project dataset, resulted in a χ^2 qualifying fraction of 87%. The dramatic improvement underscores the quality of our dataset, as well as our screening of unsuitable targets and exclusion of contaminated emission lines. The significantly improved qualifying rate increases our confidence in the applied model and thus the results.

5. Sample Testing

The large, high-quality dataset provided by our LBT observations allows us to better investigate potential systematic biases and test for reliability. We screen for potential systematic bias in the helium abundance that is correlated with other physical parameters. In evaluating corrections for systematic effects in our model, we also examine parameter values that

correspond to large systematic model corrections. Since the underlying model equations have unknown uncertainties and, by necessity, make simplifying assumptions, large model corrections for systematic effects carry the risk of introducing significant systematic error and reducing the reliability of the returned physical conditions.

In these cases, where we see evidence for potential systematic bias in the helium abundance and/or large model corrections that may introduce a systematic error compromising the reliability of the returned physical conditions, we flag those targets. We still report the best-fit parameter values for flagged targets, but they are not included in our preferred final dataset for determining Y_p.

To guard against the introduction of bias in the analysis of our data, several procedural steps in the spirit of blinding were established. First, the fitting of the emission line fluxes and the helium abundance analysis were conducted by different team members. Second, the helium analysis was conducted without reference to the metallicity of the target or the corresponding Y value. Third, decisions on flagging were made collectively based on distributions in parameter space and without identifying the targets or their other properties, such as metallicity. Where applicable, parameter flags were evaluated based on physical considerations and/or the sample distribution and without review or consideration of the helium abundance. In testing for potential systematic bias, we then subsequently evaluated for trends in the helium abundance against our model parameters and other measurements. Fourth, the final sample was assembled and finalized before determining y_p and Y_p.

5.1. Optical Depth (τ)

As discussed above in Section 2.2, our radiative transfer model comes from KI26. It assumes a spherically symmetric H II region. It does not account for any nonspherical geometry, expansion, velocity structure, or potential temperature or density inhomogeneities. Therefore, we note the potential impact of any model inaccuracy for high values of optical depth, where the effects of radiative transfer are larger. As those corrections for radiative transfer increase, the magnitude of any potential error introduced by a potential systematic error in the model increases. Furthermore, the KI26 fit equations for f_τ are fit over the range $0 < \tau < 10$ (see Section 2.2 and Appendix D). For values of optical depth with $\tau > 10$, the radiative transfer correction is an extrapolation, which may introduce increasing degrees of systematic error.

In particular, because radiative transfer at larger values of optical depth significantly decreases He I λ3889 emission and increases He I λ7065 and He I λ10830 emission (see Figure 3 above), it is possible that radiative transfer corrections could systematically bias the helium abundance. Figure 6 shows the deviation in the helium abundance, y, for our targets from their linear y-versus-O/H trend versus their best-fit optical depth value. That deviation is the residual as calculated by subtracting the linear fit (WLSQ; see Section 7.4) from the y value for each target.

There is no physical reason to expect a relationship between optical depth and helium abundance. Nonetheless, for the highest values of optical depth, there is some potential evidence of an upward bias in the helium abundance, but the limited number of points with $\tau > 2$ limits the conclusions we can draw. Additionally, the target with the largest optical depth, HS 1028+3843 with $\tau = 13.25$, appears to be a clear

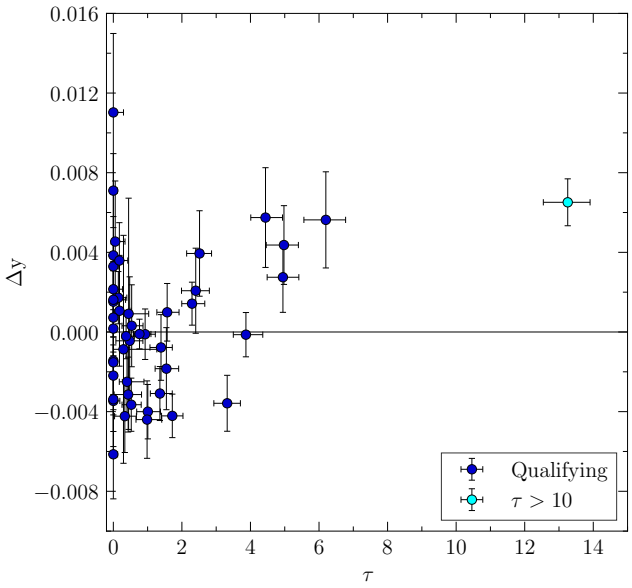


Figure 6. The deviation in the helium abundance, Δy, for our qualifying sample (47 targets) from their linear trend (i.e., their residuals) plotted versus their best-fit optical depth value, τ. The value of τ corresponds to the optical depth for He I λ3889, with the radiative transfer correction for each helium triplet emission line parameterized in terms of the optical depth for He I λ3889. One point is a clear outlier, and the fit domain for the radiative transfer equations is $0 < \tau < 10$. Therefore, the target with $\tau > 10$ is flagged. The flagged target is plotted in cyan.

outlier in the sample. Correspondingly, it carries the risk of introducing significant systematic error as an outlier with the largest radiative transfer correction, as well as due to its best-fit optical depth extending beyond the fit domain for the radiative transfer equations ($0 < \tau < 10$).

Therefore, we flag HS 1028+3843, the one target with an optical depth greater than the fit equation's domain, $\tau > 10$. One could reasonably argue for flagging the five targets with $\tau > 4$ or the 10 targets with $\tau > 2$. However, in each case, those points fall well within the range of deviations established by the much larger low optical depth subsample. As such, and given the limited number of targets with $\tau > 4$ or even $\tau > 2$, those subsets do not exhibit a definitive upward bias in the helium abundance. Furthermore, we do not have any reason to suspect that the KI26 equations may be less accurate as optical depth increases within their fit domain. Therefore, to be conservative and retain more of our sample in our preferred dataset for our subsequent analysis, we only flag the single target with $\tau > 10$.

E. Aver et al. (2012) flagged targets with $\tau > 4$, as justified by the reasoning above regarding any systematic errors introduced by the radiative transfer equations becoming more significant combined with an examination of the distribution of optical depth values in that dataset (the HeBCD dataset from Y. I. Izotov et al. 2007). There are two key differences for this work. First, E. Aver et al. (2012) utilized the BSS02 limited-range fit equations with a fit domain of $0 < \tau < 2$, rather than the new KI26 calculations with a fit domain of $0 < \tau < 10$. Second, our χ^2 qualifying dataset is larger, and points with $\tau > 4$ are not outliers in our dataset.

5.2. Underlying Helium Stellar Absorption (a_{He})

The underlying stellar absorption model employed in this work is detailed in E. Aver et al. (2021). It is based on the spectral energy distributions from BPASS (J. J. Eldridge &

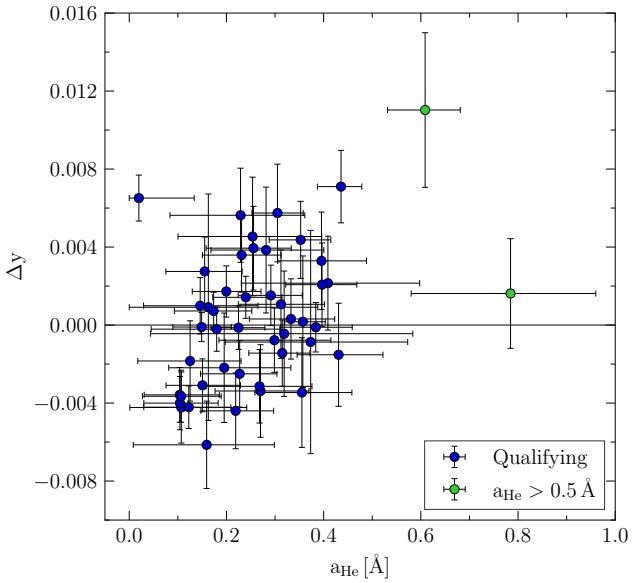


Figure 7. The deviation in the helium abundance, Δy, for our qualifying sample (47 targets) from their linear trend (i.e., their residuals) plotted versus their best-fit underlying stellar absorption parameter for the helium lines, $a_{\rm He}$. The value of $a_{\rm He}$ corresponds to the underlying absorption for He I λ4471. The correction for every other helium line is scaled off that value according to the scaling coefficients given in E. Aver et al. (2021). For one of the two targets with the highest underlying helium absorption, there is evidence of a potential upward bias in the derived helium abundance, which could bias our results. Furthermore, the two targets with the highest underlying helium absorption are outliers from the rest of the sample. Therefore, the two targets with $a_{\rm He} > 0.5$ Å are flagged. Those flagged targets are plotted in green.

E. R. Stanway 2009; J. J. Eldridge et al. 2017; E. R. Stanway & J. J. Eldridge 2018) for ages of 1, 2, 3, 4, and 5 Myr and for both single and binary star systems. For each case, the absorption equivalent width was measured, and the set of values for each line was averaged. The underlying absorption ratios vary with those starburst ages and between the single and binary star systems. As a result, it is possible the model may introduce systematic error, and any such error would increase in magnitude for larger best-fit underlying absorption values (i.e., $a_{\rm He}$ for the helium emission lines).

The deviation in the helium abundance is plotted versus the best-fit underlying stellar absorption for the helium lines, $a_{\rm He}$, in Figure 7. The value of $a_{\rm He}$ corresponds to the underlying absorption for He I λ4471. The correction for every other helium line is scaled off that value, according to the scaling coefficients given in E. Aver et al. (2021). Figure 7 shows two clear outliers with significantly elevated underlying helium absorption, demarcated by $a_{\rm He} > 0.5$ Å, with one of the two also showing a significantly elevated helium abundance. Those two targets are HS 1222+3741 and UGC 6456. Due to their greater potential for systematic error, we flag both.

In E. Aver et al. (2012), the flagging threshold for underlying helium absorption was twice as high: $a_{\rm He} > 1.0$ Å. However, that work, utilizing the HeBCD dataset from Y. I. Izotov et al. (2007), showed significantly higher values for $a_{\rm He}$ overall. For the LBT $Y_{\rm p}$ Project dataset presented in this work, the average value for $a_{\rm He}$ is 0.266 Å, while in E. Aver et al. (2012), it is 0.522 Å. Reassuringly, these lower best-fit underlying helium absorption values from the LBT $Y_{\rm p}$ Project's dataset are more consistent with our measurements from BPASS (E. Aver et al. 2015), where the value (for He I λ4471) ranged between 0.1 and 0.2 Å.

The cause for this significant decrease in the typical underlying absorption value is not known. The scaling coefficients for underlying helium absorption used in E. Aver et al. (2012) were updated in E. Aver et al. (2021), with this work using the latter, but the changes in those coefficients were not large, and the overall pattern across the primary He lines was the same. Therefore, that model change does not seem like the likely source. Our revised treatment of the blended H8 + He I λ3889 line could also have affected the best-fit $a_{\rm He}$ (E. Aver et al. 2021), but He I λ3889 is less sensitive to underlying absorption than weaker He lines (e.g., He I λ4026), and the treatment of underlying absorption for He I λ3889 was not changed. Differences in the extraction apertures for the HeBCD observations (Y. I. Izotov & T. X. Thuan 2004; Y. I. Izotov et al. 2007) and our observations may be the source, as well as potential methodological differences in reducing the spectra.

Regardless, the $a_{\rm He} > 0.5$ Å flagging criterion adopted here is conservative and results in the same number of flagged targets as were flagged in E. Aver et al. (2012) based on their criteria (i.e., two flagged targets for $a_{\rm He}$ in both). The distribution of the best-fit underlying Balmer and Paschen stellar absorption parameters, $a_{\rm H}$ and $a_{\rm P}$, did not exhibit any unusually large values or clear outliers.

5.3. *Temperature Comparison:* T*(He),* T*(O III),* T*(S III)*

In our model, the electron temperature, $T_{\rm e}$, is a model parameter, with the helium and hydrogen emissivities both functions of the same temperature. The hydrogen emission line emissivity ratios are only very weak functions of temperature (see Appendix C). As such, the best-fit electron temperature is dominantly determined by the helium emission lines, due to their much stronger temperature sensitivity compared to the hydrogen lines (M. Peimbert et al. 2000; K. A. Olive & E. D. Skillman 2004). In general, one would expect that this helium temperature, T(He), should closely track the temperature determined by the [O III] emission, T(O III), due to the O^{++} ionization zone encompassing almost the entirety of the He^{+} zone (∼95%). For the idealized, spherically symmetric H II region, the He^{+} zone could have a slightly lower average electron temperature than the O^{++} zone due to its larger volume, but this effect would be small due to the extent of their overlap.

However, in the presence of temperature fluctuations throughout the emission region, the higher-temperature regions will contribute an elevated share of the total [O III] emission, thus weighting the [O III] flux more strongly to the higher-temperature regions than their share of the volume. This effect could bias T(O III) systematically upward compared to T(He), as has been observed in some studies (M. Peimbert et al. 2000; A. Peimbert et al. 2002; K. A. Olive & E. D. Skillman 2004; E. Aver et al. 2011; J. E. Méndez-Delgado et al. 2025), though not others (N. G. Guseva et al. 2006, 2007). A. Peimbert et al. (2002) found that T(He) was always less than T(O III) by 6%–10% using their best-fit values from the He emission lines and 3%–11% in their photoionization modeling. In our model, we use T(O III) as a weak prior on determining the best-fit value for T(He) (E. Aver et al. 2011, 2021).

We would expect T(He) to track T(O III) closely, though possibly with a value that is slightly lower, though not necessarily, given differing estimates of the typical magnitude

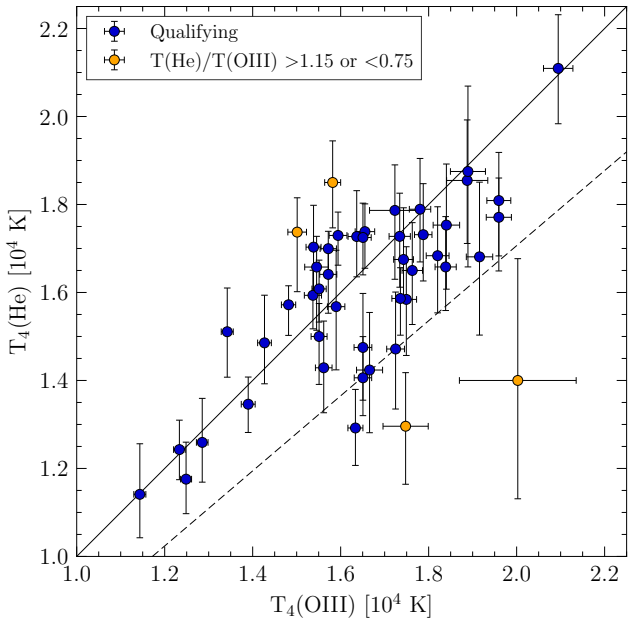


Figure 8. The best-fit electron temperature from our model as determined (primarily) by the He emission lines, T(He), plotted versus the electron temperature determined by the [O III] emission lines, T(O III). Our qualifying sample (47 targets) is plotted. The solid line is for equality, and the dashed line represents the expected relationship between T(He) and T(O III) for temperature fluctuations as parameterized by $t^2 = 0.03$ (e.g., M. Peimbert et al. 2000; J. García-Rojas & C. Esteban 2007). (The "t^2" parameter is the rms deviation from the average nebular temperature. It is a measure of the internal temperature variations of the gas as quantified in the formalism proposed by M. Peimbert 1967). A definitive upward bias in T(O III) is not observed, though there is some evidence for that upward bias at higher temperatures ($\gtrsim$15,000 K). Two targets where T(He) exceeds T(O III) and two targets where T(He) is lower than T(O III) appear to be outliers from the rest of the sample. Those flagged targets are plotted in orange.

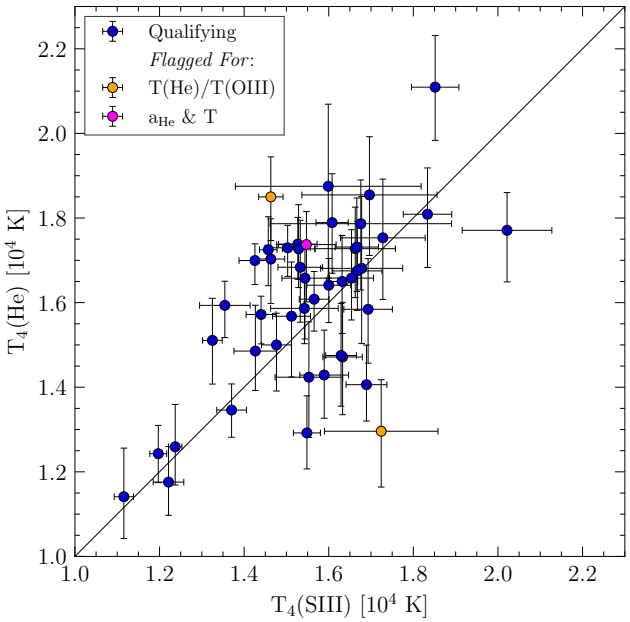


Figure 9. The best-fit electron temperature from our model as determined (primarily) by the He emission lines, T(He), plotted versus the electron temperature determined by the [S III] emission lines, T(S III). Our qualifying sample (47 targets) is plotted, though excluding one target without a [S III] temperature. The solid line is for equality. Four targets are flagged for the discrepancy in their T(He) and T(O III) temperatures (see Figure 8), with two of the four plotted in orange and one that is additionally flagged for underlying helium absorption plotted in magenta, and the fourth is not plotted because it lacks a T(S III) value. The two orange targets appear to be outliers when comparing their T(He) and T(S III), with one higher and one lower, just as was seen for their T(He) and T(O III) in Figure 8. The magenta point's T(He) and T(S III) are not discrepant, but it is already flagged for $a_{\rm He} > 0.5$.

of temperature inhomogeneities in H II regions (M. Peimbert et al. 2000; A. Peimbert et al. 2002; N. G. Guseva et al. 2006, 2007). Figure 8 compares T(He) and T(O III). The magnitude of the T(He) uncertainties limits one's ability to draw firm conclusions, but T(O III) does not appear to be generally biased high compared to T(He). At the higher temperatures in our sample ($\gtrsim$15,000 K), there is some evidence for a systematically higher value for T(O III) than T(He), but it is not conclusive.

More striking, perhaps, is the difference in T(He) and T(O III), with T(He) exceeding T(O III) in many cases, and occasionally dramatically lower, as shown in Figure 8. The large uncertainties for T(He) mean that the two temperatures agree within 2σ for most of the targets, but there are also a few clear outliers with larger absolute and relative differences. These large temperature discrepancies raise concerns that T(He) may be systematically over- or underestimated in those targets, biasing y^+. In particular, T(He) exceeds T(O III) by 2680 K or 17.0% for Mrk 71 and 2360 K or 15.7% for HS 1222+3741, though it should be noted that HS 1222+3741 is flagged for underlying helium absorption, and its best-fit parameter values may be less reliable and potentially systematically biased. For two other targets, T(He) is lower than T(O III) by a much greater degree than in the rest of the sample. For AGC 198691, T(He) is lower than T(O III) by 6030 K or 30.1%, and it is lower by 4520 K or 25.8% for J0118+3512.

The very tight linear relationship between T(O III) and T(S III), as shown in Paper II, means that T(S III) can also be used as a diagnostic for identifying T(He) discrepancies. Figure 9 compares T(He) and T(S III). Though T(S III) tends to be slightly lower than T(O III) (see Paper II), a similar pattern emerges. As we saw comparing Mrk 71's helium best-fit temperature to its [O III] temperature (Figure 8), T(He) is also discrepantly elevated compared to T(S III) for Mrk 71. Similarly, for J0118+3512, its T(He) is discrepantly low compared to T(S III), just like it was compared to T(O III). HS 1222+3741 is not an outlier when comparing T(He) to T(S III), unlike for T(O III), but HS 1222+3741 is already flagged for underlying helium absorption. The fourth outlier identified by T(O III), AGC 198691, does not have a calculated [S III] temperature because [S III] λ6312 was not detected. Figure 10, a plot of T(He)/T(S III) versus T(He)/T(O III), identifies those two unique T(He) outliers, Mrk 71 and J0118+3512, most clearly and demonstrates that they are shared outliers on each measure, T(O III) and T(S III).

For these four identified outliers (Figure 8), the temperature differences are larger than can be justified by any reasonable physical model. The calculated helium abundance, y^+, depends strongly on the electron temperature. Therefore, such large temperature differences in the best-fit T(He) value and the T(O III) and T(S III) values may be introducing a significant systematic error in the best-fit helium abundance. On this basis, we flag the four targets identified above: HS 1222+3741 and Mrk 71 for T(He)/T(O III) $> 115\%$ and AGC 198691 and J0118+3512 for T(He)/T(O III) $< 75\%$. HS 1222+3741 is already flagged for $a_{\rm He} > 0.5$ and does not increase our number of flagged targets.

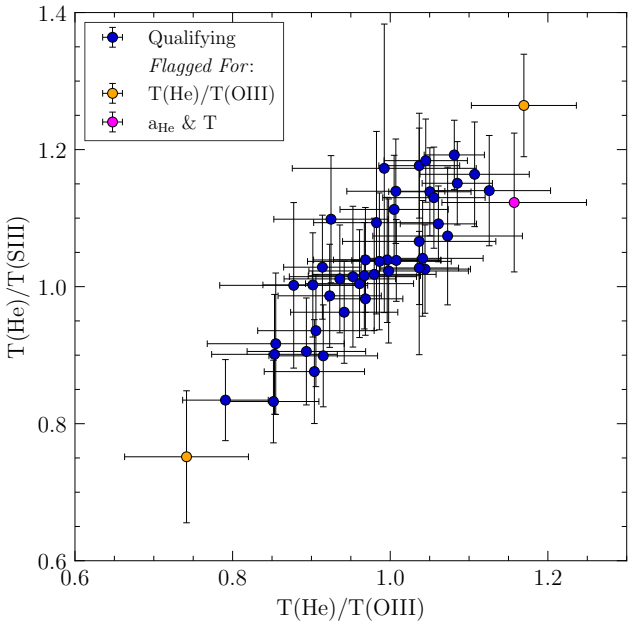


Figure 10. T(He)/T(S III) plotted versus T(He)/T(O III) for our qualifying sample (47 targets), though excluding one target lacking a [S III] temperature. A strong linear relationship is observed between the two temperature ratios, as expected based on the results presented in Paper II. Four targets are flagged for the discrepancy in their T(He) and T(O III) temperatures (see Figure 8), with two of the four plotted in orange and one that is additionally flagged for underlying helium absorption plotted in magenta, and the fourth is not plotted because it lacks a T(S III) value. The two orange targets are outliers, with one where T(He) exceeds both T(O III) and T(S III) and one where it is lower than both. The magenta point's T(He)/T(S III) value is not discrepant, but it is already flagged for $a_{\rm He} > 0.5$. This figure reinforces the flagging selections in Figure 8.

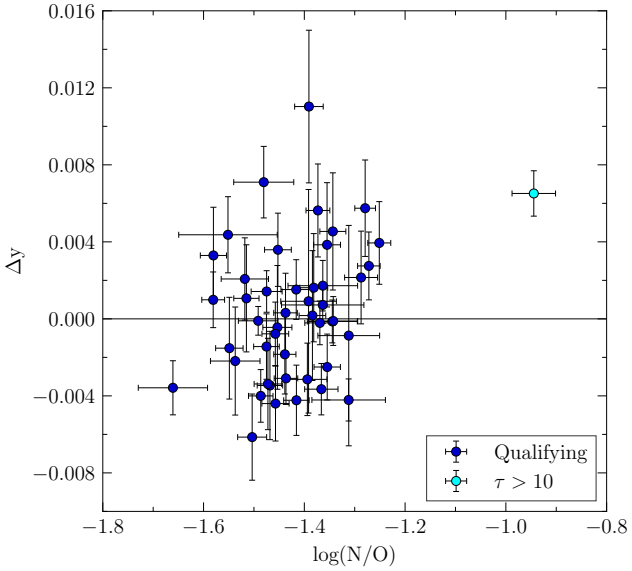


Figure 11. The deviation in the helium abundance, Δy, for our qualifying sample (47 targets) from their linear trend (i.e., their residuals) plotted versus log(N/O). There is no clear evidence of systematic bias in the helium abundance related to the N/O abundance ratio for the targets in our sample. The one target with an anomalously larger log(N/O) is flagged for optical depth ($\tau > 10$) and plotted in cyan.

5.4. Nitrogen-to-oxygen Ratio (log(N/O))

In a recent work, H. Yanagisawa et al. (2024) report results from JWST observations of three high-z ($z \sim 6$) galaxies, which show high values for their nitrogen-to-oxygen abundance ratio ($\log(\mathrm{N/O}) \gtrsim -1.0$). They also show very strong He I emission, which may signal significantly elevated helium abundances ($y = \mathrm{He/H} \gtrsim 0.10$), compared to what would be expected for their metallicity, O/H. Based on that correlation between high N/O and potentially high He/H, and the possibility for chemical evolution that deviates substantially from the rest of their sample, H. Yanagisawa et al. (2026) exclude four targets from their sample with $\log(\mathrm{N/O}) > -1.0$.

We investigated flagging targets in our sample based on their N/O value, but, as shown in Figure 11, our sample did not exhibit any systematic effect on helium abundance as a function of N/O. Furthermore, there is only one target in our χ^2 qualifying sample with $\log(\mathrm{N/O}) > -1.0$, and it is already flagged for optical depth. Excluding this target, our sample has a nitrogen-to-oxygen abundance ratio in the range $-1.7 < \log(\mathrm{N/O}) < -1.2$.

The target in Figure 11 with $\log(\mathrm{N/O}) > -1.0$, HS 1028+3843, has, by far, the *highest* best-fit optical depth in the sample, with $\tau = 13.25$. This is very large, and unusually so, for a low-metallicity H II region. The galaxies in H. Yanagisawa et al. (2024) with high N/O also show very high optical depths ($\tau > 8$). Similarly, two targets excluded due to their best-fit χ^2 values exceeding their 95% CL have $\log(\mathrm{N/O}) \gtrsim -1.0$, HS 0837+4717 and WISEA J051902.72+000728.7, and their best-fit optical depth values are 9.46 and 8.57, respectively. Also worthy of note, HS 0837+4717 exhibits the strongest wings on its strong emission lines, as mentioned above (Section 4), and it returns $y^+ = 0.10907$.

As discussed above (Section 5.1), high optical depth values carry the potential for significant systematic errors in the model and the determined helium abundance. Both high log (N/O) and large optical depth values may indicate physical conditions in the H II region that do not conform with the rest of the sample and the applied modeling. Although there appears to be a correlation between high τ and high log(N/O), they may both be markers for H II regions with atypical underlying dynamics or physical conditions. To this end, we provide a more detailed discussion concerning the elevated N/O abundances measured in five of the LBT $Y_{\rm p}$ targets in Paper VI.

5.5. Additional Testing

Similar to Figures 6, 7, and 11, we examined the deviation in the helium abundance from the sample trend versus each of our physical model parameters. As mentioned in Section 5.2, the underlying Balmer and Paschen stellar absorption parameters, $a_{\rm H}$ and $a_{\rm P}$, did not exhibit any unusually large values, clear outliers, or systematic trend with the helium abundance, nor did the reddening, C(Hβ), or neutral hydrogen fraction, ξ. Only in the cases of optical depth and temperature was there clear evidence of a potential systematic bias. In the case of temperature, T(He), that relationship is expected since, all else being equal, higher temperatures increase the helium abundance, due to the emissivity ratio (E(He)/E(Hβ) for each of the three strong helium lines, He I $\lambda\lambda$4471, 5876, and 6678) decreasing with temperature. As discussed in Section 5.3, we do flag based on the divergence of T(He) from T(O III) and T(S III). Similar to our model parameters, we also investigated for other parameters and measured values, such as W(Hβ), $n_{\rm e}$(S II), $\mathrm{He^{++}/H^+}$, $\mathrm{O^+/O}$, $\eta = \frac{\mathrm{O^+/O^{+2}}}{\mathrm{S^+/S^{+2}}}$, χ^2/d.o.f., z, etc. We did not find clear evidence for a systematic relationship

Table 4
Sample Breakdown of Cuts and Flags

	Number of Targets
The LBT Y_p Project dataset	54
$\chi^2 > 95\%$ CL	7/54
Well-defined solutions	47
Flagged	
$\tau > 4$	1
$a_{He} > 0.5$ Å	2
$T(He)/T(O\ III) > 1.15$	1
$T(He)/T(O\ III) < 0.75$	2
Subtotal: flagged	6
Final qualifying dataset	41

between any of these other parameters and the difference in helium abundance from the linear trend, Δy. Finally, we also examined the χ^2 contributions from each individual emission line for a correlation with each of our model parameters, as well as Δy, and we did not find any significant correlation or potential systematic bias.

6. Sample Results

Following the χ^2 qualifying cut and applied flags for potential systematic errors (Sections 4 and 5), Table 4 presents a breakdown of our sample dataset. For our starting sample of 54 targets, 7 were excluded due to best-fit (minimized) χ^2 values exceeding their 95% CL (see Section 4). Of the remaining 47 targets, 6 are flagged, and there are 41 qualifying targets without any flags. These 41 targets constitute our final qualifying dataset. The best-fit parameter solutions with uncertainties for each of the 47 targets, qualifying and flagged, is provided in Table 2 above.

6.1. Uncertainty Comparison

Comparing our results to our previous work is complicated by the mixed sources of observations in our two most recent Y_p determinations (E. Aver et al. 2021, 2022). To recap, the LBT Y_p Project began with the high-quality LBT MODS and LUCI observations of Leo P (E. D. Skillman et al. 2013; E. Aver et al. 2021). The reanalysis of Leo P in E. Aver et al. (2021) utilized a significantly expanded and improved physical model enabled by the MODS and LUCI observations. Leo P served as a proof of concept for the advances in helium abundance determinations that could be made based on high-quality, high signal-to-noise, and broad wavelength coverage optical and NIR spectra. Subsequently, AGC 198691 was also reanalyzed based on an LBT MODS observation (E. Aver et al. 2022). Therefore, to properly compare with our results prior to the LBT Y_p Project, E. Aver et al. (2015) is the appropriate comparison.

Increasing the precision of galactic helium abundance determinations is one of the primary goals of this project. Comparing to our previous results, the average relative uncertainty for y^+ in E. Aver et al. (2015) was 4.0%, while for the LBT Y_p Project, it is 2.3%. This 42% reduction in the average He abundance uncertainty across qualifying targets without flags (41 targets) is due to multiple improvements in the LBT Y_p Project:

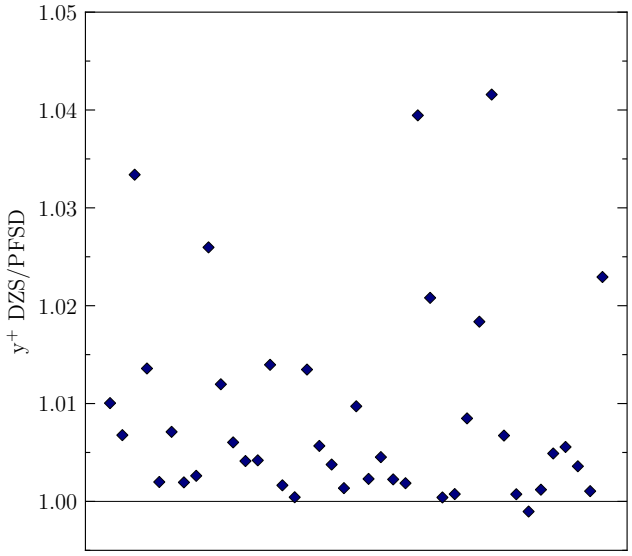


Figure 12. The best-fit helium abundance, y^+, based on the updated He emissivities of G. Del Zanna & P. J. Storey (2022) relative to that of the previously employed He emissivities (R. L. Porter et al. 2012, 2013). Our final qualifying sample (41 targets) is plotted. Due to the relatively minor changes in the emissivities at low density (~1%), the effect on y^+ is relatively small, though it is systematic. Overall, there is an increase in the resulting helium abundance from the new emissivities, with an average relative increase of 0.9%.

1. high signal-to-noise LBT MODS and LUCI spectral observations, uniformly observed and reduced (see Papers II and III);
2. high spectral resolution and broad wavelength coverage optical and NIR spectra, as enabled by MODS and LUCI (see Paper I);
3. the full deployment of our expanded model, including additional weaker He lines, Paschen lines, and higher Balmer lines, as enabled by the high resolution and broad wavelength coverage observations (see E. Aver et al. 2021); and
4. our improved flux uncertainty model based on the stable MODS spectral sensitivity function (see Paper I).

While all of our model parameters are more precisely determined, given the limited constraints on the neutral hydrogen fraction values, ξ, in our previous samples (E. Aver et al. 2012, 2013, 2015), it is particularly encouraging to see the significant improvements in better constraining ξ (for $T_4 > 1.4$). Comparing to the E. Aver et al. (2015) dataset, the average uncertainty for ξ decreased by 90%. The inclusion of Paschen and higher Balmer emission lines significantly improves the determination of the primary hydrogen fit parameters, $C(H\beta)$, a_H, a_P, and ξ, which, in turn, contribute to the reduced uncertainty for y^+.

6.2. Emissivity Comparison

In this work, we updated the He emissivities employed in our model from the R. L. Porter et al. (2012, 2013) emissivities to the more recent emissivity calculations of G. Del Zanna & P. J. Storey (2022) (Section 2.1). At the same time, the normalizing Hβ emissivity, $E(H\beta)$, was also updated using the new P. J. Storey & T. Sochi (2015) H emissivities (Section 2.1). Figure 12 shows the change in y^+ from the G. Del Zanna & P. J. Storey (2022) emissivities.

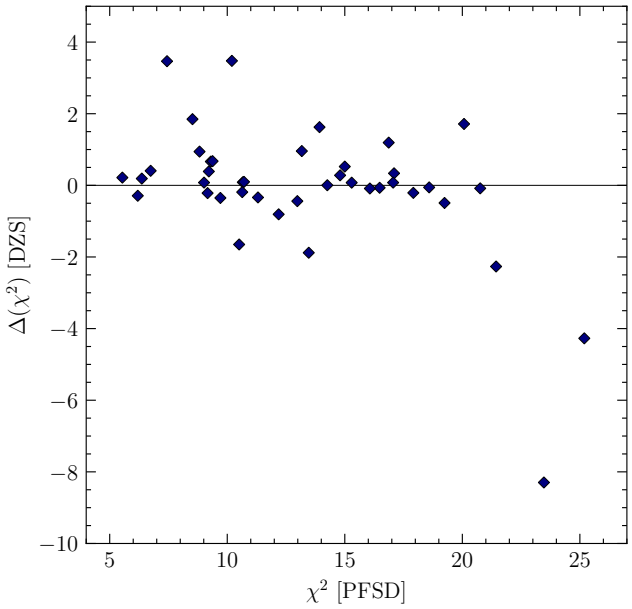


Figure 13. The difference in the best-fit (minimized) χ^2 between the updated He emissivities of G. Del Zanna & P. J. Storey (2022) and the previously employed He emissivities of R. L. Porter et al. (2012, 2013) plotted versus the R. L. Porter et al. (2012, 2013) best-fit χ^2. Our final qualifying sample (41 targets) is plotted. Due to the relatively minor changes in the emissivities at low density (∼1%), the effect on χ^2 is relatively small, and for most targets, the change is consistent with random variation (i.e., some small increases, some small decreases). However, the two largest changes from the updated emissivities are decreases in χ^2, indicating closer agreement between the model and observed fluxes.

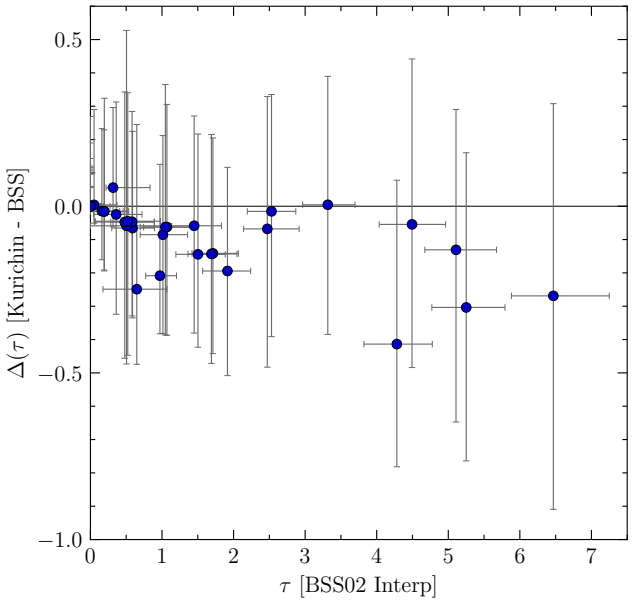


Figure 14. The difference in the best-fit optical depth, τ, between the KI26 radiative transfer fit equations and the BSS02 radiative transfer interpolation plotted versus τ based on the interpolation. The value of τ corresponds to the optical depth for He I λ3889, with the radiative transfer correction for each helium triplet emission line parameterized in terms of the optical depth for He I λ3889. Our final qualifying sample (41 targets) is plotted. The best-fit τ tends to decrease, largely driven by an increase in the magnitude of the radiative transfer effect for He I λ7065 (the line most strongly affected by radiative transfer; see Figure 4).

As shown in Figure 12, the effect on the helium abundance was relatively small but systematic, with all but one target (40 of 41) showing a small increase in y^+. Across our final qualifying dataset, the average relative change in y^+ was an increase of 0.9%. As discussed in Section 2.1, the most significant change for the G. Del Zanna & P. J. Storey (2022) emissivities is a decrease in the He I λ6678 emissivity (see Figures 1 and 2). Though complicated by the full set of model parameter values changing, a decrease in the He I λ6678 emissivity tends to increase the helium abundance, since the lower emissivity requires a larger abundance to produce the same flux.

The updated absolute Hβ emissivity increased by ∼0.1%–0.25%. Since E(Hβ) normalizes the He emissivities, this change decreases the helium-to-hydrogen emissivity ratio uniformly for all helium lines, thus increasing y^+ by a commensurate amount. The combination of the G. Del Zanna & P. J. Storey (2022) emissivities change, primarily a decrease in He I λ6678, along with the E(Hβ) increase, yields the overall increase in the best-fit helium abundance, y^+, of 0.95%.

Figure 13 compares the best-fit χ^2 for the R. L. Porter et al. (2012, 2013) and G. Del Zanna & P. J. Storey (2022) emissivities. As shown in Figure 13, the best-fit χ^2 value is largely unchanged for the majority of our sample. That is not surprising given the relatively minor changes in the emissivities at low density (see Figure 2). However, it is encouraging that the two targets with the largest changes in their χ^2 value show decreases. The decreased best-fit χ^2 for those targets from the G. Del Zanna & P. J. Storey (2022) emissivities indicates improved agreement between the model and observed fluxes.

6.3. Radiative Transfer Model Comparison

As discussed in Section 2.2, we have replaced the radiative transfer calculations of BSS02 in our model with the recent, updated calculations by KI26. In this subsection, we track the effects of the new KI26 radiative transfer calculations from the previous BSS02 calculations, as incorporated using the trilinear interpolation from BSS02.

As shown in Figure 4 and discussed in Section 2.2, the magnitude of the radiative transfer effect for He I λ7065—the line most strongly affected by radiative transfer—is increased in the new KI26 calculations compared to the previous BSS02 calculations. As a result, to achieve a similar increase to He I λ7065 from radiative transfer as the interpolation would predict, the corresponding optical depth will be lower. Therefore, it is not surprising that the best-fit optical depth value for targets returning higher optical depths tended to decrease from the adoption of the new KI26 radiative transfer equations.

This is shown in Figure 14, which plots the change in the best-fit τ from the KI26 equations compared to the best-fit τ from the BSS02 interpolation. As τ increases, the divergence between the BSS02 interpolation and the KI26 fit equations tends to grow in most cases; hence, the divergence between the best-fit τ values also tends to grow. Correspondingly, the magnitude of the decrease to the returned τ under the new KI26 radiative transfer model tends to grow proportionally to the τ value itself (i.e., a larger decrease for higher τ).

Fifteen targets in our sample have best-fit optical depths with $\tau < 0.1$ (13 with $\tau \sim 0$) and are essentially unaffected by radiative transfer effects. As a result, their physical parameter solutions were not significantly altered by the adoption of the new KI26 radiative transfer calculations. For the remaining

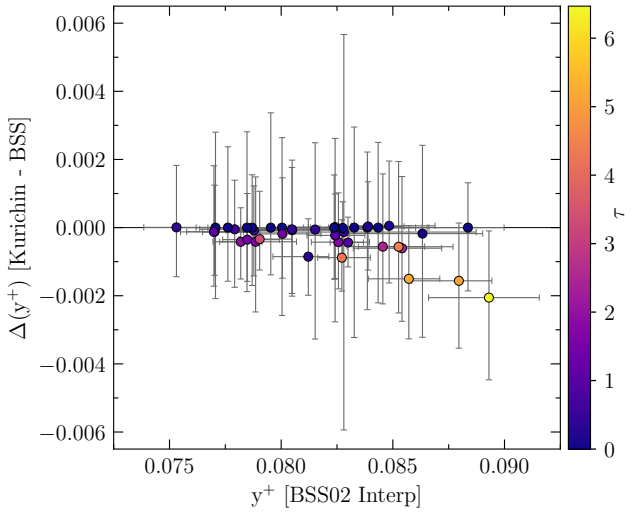


Figure 15. The difference in the best-fit helium abundance, y^+, between the KI26 radiative transfer fit equations and the BSS02 radiative transfer interpolation plotted versus the interpolation y^+. Our final qualifying sample (41 targets) is plotted, and the points are shaded by their best-fit optical depth ($\tau = \tau_{3889}$) from the BSS02 interpolation. For targets with nonnegligible optical depths, the best-fit y^+ decreases marginally, due to the decrease in the best-fit optical depth, τ (see Figure 14).

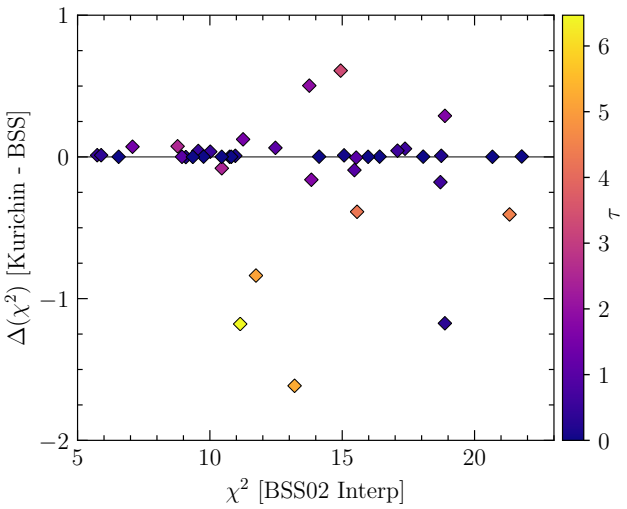


Figure 16. The difference in the best-fit (minimized) χ^2 between the KI26 radiative transfer fit equations and the BSS02 radiative transfer interpolation plotted versus the interpolation χ^2. Our final qualifying sample (41 targets) is plotted, and the points are shaded by their best-fit optical depth ($\tau = \tau_{3889}$) from the BSS02 interpolation. Consistent with the similarities in the two radiative transfer calculations, most of the sample exhibits random scatter in their $\Delta(\chi^2)$ about zero. For five of the targets with higher values of optical depth, there are significant changes in their best-fit χ^2, and they each show decreases. This provides evidence that the new KI26 calculations are an improvement upon the preceding BSS02 calculations, as expected.

targets, the effects of the change vary depending on their previous best-fit solution. As discussed above, the best-fit τ tended to decrease, and that decrease propagates through to the helium abundance, generally resulting in a decreased best-fit y^+. This is shown in Figure 15, which compares the change in the best-fit y^+ from the KI26 equations to the best-fit τ from the BSS02 interpolation. Because, for our relatively low optical depth systems, radiative transfer only has significant effects on He I $\lambda\lambda$3889, 7065, and 10830, the effect on y^+ is attenuated by the presence of the other helium emission lines.

To help evaluate the accuracy of the updated KI26 calculations compared to the previous BSS02 calculations, we compare the best-fit χ^2 values returned for each. This is shown in Figure 16, which plots the change in χ^2 from the adopted KI26 fit equations versus the χ^2 from the BSS02 interpolation. If the new KI26 calculations are an improvement, one would expect better agreement between the fluxes predicted by the model and their measured values.

Overall, that is what we see. For most of the lines and most relevant portions of parameter space, the new KI26 calculations are not substantially different from the preceding BSS02 calculations. As such, it is not surprising to see that most of our sample exhibits random scatter in their $\Delta(\chi^2)$ about zero with changes of less than ± 0.75 in χ^2. However, for five of the targets with higher values of optical depth—four with $\tau > 4$ and one with $\tau > 2$—there are significant changes in their best-fit χ^2, and they each show decreases, with three targets showing decreases greater than one unit in χ^2. Not coincidentally, the four targets with $\tau > 4$ also exhibit the four largest decreases in their τ and y^+ best-fit values (see Figures 14 and 15).

That all of the largest χ^2 changes are significant decreases provides evidence that the KI26 calculations are an improvement and more accurate than the preceding BSS02 calculations. This advance can be traced back to the improvements in modeling and updated atomic data in the KI26 calculations. In particular, the significant decreases in χ^2 for the higher optical depth targets provides evidence for improved reliability of the KI26 radiative transfer corrections at higher values of optical depth. In turn, that lends support for not flagging the results that fall within the fit domain for the KI26 equations ($0 < \tau < 10$).

That all of the largest χ^2 changes are significant decreases provides evidence that, as expected, the KI26 calculations, employing the latest atomic data, as well as improvements in modeling, are an improvement and more accurate than the preceding BSS02 calculations.

7. Primordial Helium

In this section, we calculate the primordial helium abundance, y_p, which is most commonly reported and discussed as a mass fraction, Y_p. To best determine Y_p, we have prioritized galaxies with the lowest metallicity, O/H. The unprecedented number of low-metallicity, yet high-quality, targets in our sample enables, for the first time, a robust weighted average determination (Section 7.3). For comparison, we also perform a linear regression using the full qualifying sample without any flags (Section 7.4). In Section 7.5, we compare our results to previous determinations in the literature. Before calculating Y_p, we first briefly discuss He^{++} and He^0 in Section 7.1, and then we provide an overview of our sample and its characteristics in Section 7.2 below.

7.1. He^{++} and He^0

For targets with He II λ4686 detections, we calculate y^{++}, as reported below in Table 5, to add to y^+ to determine y. The He II λ4686 emissivity (relative to Hβ) is taken from R. A. Benjamin et al. (1999), based on P. J. Storey & D. G. Hummer (1995). The uncertainty for y^{++} is determined by propagating the flux, T_e, $C(H\beta)$, and a_H uncertainties. Our model does not include corrections for neutral helium.

Table 5
Final Dataset Helium Abundance Values

Object	$O/H \times 10^5$	$y^+ = He^+/H^+$	$y^{++} = He^{++}/H^+$	$y = y^+ + y^{++}$	Y
Final Dataset Not Flagged					
I Zw 18 SE	1.49 ± 0.06	0.08243 ± 0.00278	0.00034 ± 0.00005	0.08277 ± 0.00278	0.2487 ± 0.0063
DDO 68	1.52 ± 0.08	0.07706 ± 0.00280	0.00246 ± 0.00017	0.07952 ± 0.00281	0.2412 ± 0.0065
Leo P	1.53 ± 0.11	0.08386 ± 0.00241	0.00000 ± 0.00000	0.08386 ± 0.00241	0.2511 ± 0.0054
SBS 0335–052E	1.74 ± 0.06	0.08470 ± 0.00250	0.00279 ± 0.00006	0.08748 ± 0.00250	0.2591 ± 0.0055
J2104–0035	1.90 ± 0.08	0.08267 ± 0.00581	0.00000 ± 0.00000	0.08267 ± 0.00581	0.2484 ± 0.0131
LEDA 2790884	2.66 ± 0.09	0.08615 ± 0.00304	0.00026 ± 0.00005	0.08641 ± 0.00304	0.2567 ± 0.0067
J1044+0353	2.67 ± 0.08	0.07844 ± 0.00206	0.00159 ± 0.00004	0.08003 ± 0.00206	0.2424 ± 0.0047
SBS 0940+544	2.91 ± 0.10	0.08146 ± 0.00321	0.00000 ± 0.00000	0.08146 ± 0.00321	0.2456 ± 0.0073
UGC 4483	3.06 ± 0.11	0.07847 ± 0.00281	0.00000 ± 0.00000	0.07847 ± 0.00281	0.2387 ± 0.0065
SBS 1159+545	3.23 ± 0.11	0.07813 ± 0.00135	0.00074 ± 0.00006	0.07886 ± 0.00136	0.2397 ± 0.0031
J0133+1342	3.52 ± 0.13	0.08042 ± 0.00206	0.00189 ± 0.00008	0.08231 ± 0.00206	0.2475 ± 0.0047
HS 1353+4706	3.61 ± 0.12	0.08036 ± 0.00113	0.00144 ± 0.00007	0.08180 ± 0.00113	0.2464 ± 0.0026
J2213+1722	3.72 ± 0.18	0.07787 ± 0.00170	0.00166 ± 0.00016	0.07952 ± 0.00171	0.2411 ± 0.0039
HS 0122+0743	3.80 ± 0.13	0.08214 ± 0.00145	0.00089 ± 0.00006	0.08303 ± 0.00145	0.2491 ± 0.0033
SBS 1415+437	4.01 ± 0.16	0.07870 ± 0.00170	0.00193 ± 0.00005	0.08063 ± 0.00170	0.2437 ± 0.0039
SBS 1211+540	4.18 ± 0.12	0.07761 ± 0.00237	0.00109 ± 0.00007	0.07871 ± 0.00237	0.2392 ± 0.0055
WJ1327+4022	4.30 ± 0.13	0.07532 ± 0.00182	0.00256 ± 0.00013	0.07788 ± 0.00182	0.2373 ± 0.0042
HS 1442+4250	4.75 ± 0.16	0.08327 ± 0.00323	0.00275 ± 0.00011	0.08602 ± 0.00323	0.2558 ± 0.0071
J0807+3414	4.85 ± 0.16	0.08725 ± 0.00241	0.00057 ± 0.00008	0.08782 ± 0.00241	0.2597 ± 0.0053
UM 133	4.93 ± 0.23	0.08434 ± 0.00250	0.00115 ± 0.00007	0.08549 ± 0.00250	0.2546 ± 0.0056
J1323–01325	4.96 ± 0.16	0.08480 ± 0.00215	0.00134 ± 0.00004	0.08615 ± 0.00215	0.2560 ± 0.0047
J1331+4151	5.08 ± 0.17	0.07690 ± 0.00136	0.00132 ± 0.00007	0.07822 ± 0.00137	0.2381 ± 0.0032
SBS 1420+544	5.15 ± 0.15	0.08421 ± 0.00176	0.00077 ± 0.00003	0.08498 ± 0.00176	0.2534 ± 0.0039
SBS 1249+493	5.37 ± 0.19	0.07686 ± 0.00194	0.00100 ± 0.00009	0.07786 ± 0.00194	0.2372 ± 0.0045
UGC 5541	5.45 ± 0.25	0.08004 ± 0.00264	0.00071 ± 0.00008	0.08075 ± 0.00264	0.2439 ± 0.0060
SBS 1030+583	5.89 ± 0.19	0.07953 ± 0.00337	0.00298 ± 0.00010	0.08251 ± 0.00337	0.2478 ± 0.0076
SBS 1331+493	6.27 ± 0.30	0.08275 ± 0.00096	0.00037 ± 0.00003	0.08311 ± 0.00096	0.2492 ± 0.0022
UM 161	6.33 ± 0.23	0.07987 ± 0.00165	0.00175 ± 0.00009	0.08162 ± 0.00165	0.2458 ± 0.0037
UM 461	6.50 ± 0.45	0.07870 ± 0.00140	0.00015 ± 0.00002	0.07884 ± 0.00140	0.2395 ± 0.0032
WJ1136+4709	6.77 ± 0.23	0.08489 ± 0.00190	0.00116 ± 0.00007	0.08605 ± 0.00190	0.2557 ± 0.0042
KUG 1138+327	6.78 ± 0.41	0.08836 ± 0.00186	0.00120 ± 0.00005	0.08956 ± 0.00186	0.2634 ± 0.0040
HS 0134+3415	6.93 ± 0.31	0.07777 ± 0.00109	0.00050 ± 0.00002	0.07827 ± 0.00109	0.2381 ± 0.0025
WJ2310–0211	6.95 ± 0.63	0.08640 ± 0.00198	0.00046 ± 0.00002	0.08686 ± 0.00198	0.2575 ± 0.0044
SBS 1152+579	8.15 ± 0.48	0.08183 ± 0.00111	0.00069 ± 0.00002	0.08253 ± 0.00111	0.2478 ± 0.0025
SBS 1437+370	8.59 ± 0.37	0.08237 ± 0.00155	0.00187 ± 0.00007	0.08425 ± 0.00155	0.2516 ± 0.0035
SBS 0946+558	9.60 ± 0.65	0.08392 ± 0.00131	0.00067 ± 0.00003	0.08459 ± 0.00131	0.2523 ± 0.0029
J1148+2546	10.30 ± 0.77	0.08399 ± 0.00214	0.00105 ± 0.00006	0.08504 ± 0.00214	0.2533 ± 0.0047
HS 0029+1748	11.17 ± 0.42	0.07869 ± 0.00133	0.00075 ± 0.00004	0.07944 ± 0.00134	0.2406 ± 0.0031
SBS 0948+532	12.31 ± 0.71	0.08219 ± 0.00127	0.00096 ± 0.00004	0.08315 ± 0.00127	0.2490 ± 0.0029
SBS 1135+581	13.71 ± 0.79	0.08256 ± 0.00074	0.00080 ± 0.00004	0.08336 ± 0.00075	0.2494 ± 0.0017
SBS 0926+606	14.48 ± 0.99	0.08043 ± 0.00188	0.00000 ± 0.00000	0.08043 ± 0.00188	0.2427 ± 0.0043
Final Dataset with Flags					
AGC 198691	1.00 ± 0.12	0.08076 ± 0.00572	0.00000 ± 0.00000	0.08076 ± 0.00572	0.2441 ± 0.0131
J0118+3512	3.08 ± 0.20	0.07520 ± 0.00223	0.00059 ± 0.00020	0.07579 ± 0.00224	0.2325 ± 0.0053
UGC 6456	4.45 ± 0.21	0.08375 ± 0.00281	0.00000 ± 0.00000	0.08375 ± 0.00281	0.2507 ± 0.0063
HS 1028+3843	6.38 ± 0.21	0.08786 ± 0.00118	0.00106 ± 0.00004	0.08892 ± 0.00118	0.2620 ± 0.0026
HS 1222+3741	6.78 ± 0.28	0.09171 ± 0.00396	0.00179 ± 0.00012	0.09349 ± 0.00396	0.2718 ± 0.0084
Mrk 71	7.33 ± 0.24	0.08369 ± 0.00108	0.00027 ± 0.00001	0.08397 ± 0.00108	0.2511 ± 0.0024

Neutral helium is not expected to be significant for our targets, given our low-metallicity sample with hard ionization radiation fields. This conclusion is supported by our examination of Δy versus the radiation softness parameter, $\eta = \frac{O^+/O^{+2}}{S^+/S^{+2}}$ (J. M. Vilchez & B. E. J. Pagel 1988), for our sample. If neutral helium contributions were significant, a relationship showing decreased helium with increasing η would be expected. As noted in Section 5.5, our sample does not show any evidence of a relationship between Δy and η.

7.2. Sample Overview

From our initial dataset of 54 targets, there are 47 targets in the χ^2 qualifying dataset, including six that are flagged (see Section 6). For the 41 qualifying points without any flags, Figure 17 presents y versus O/H for the LBT Y_p Project dataset, as well as the corresponding E. Aver et al. (2015) dataset for comparison. The values plotted in the upper panel are given in Table 5, with the O/H values taken directly from Paper II.

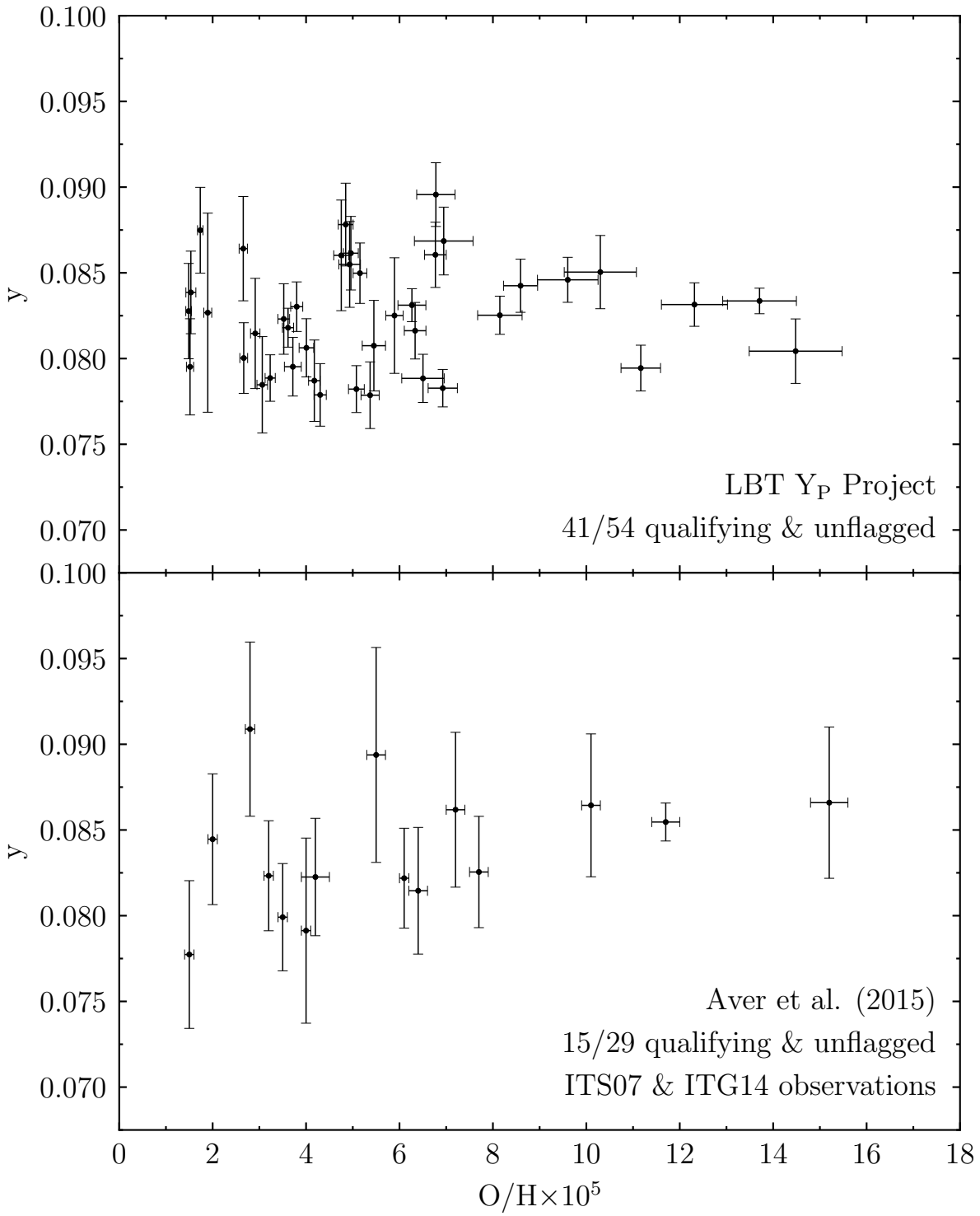


Figure 17. Comparison of the E. Aver et al. (2015) dataset with the LBT Y_p Project dataset presented in this work, with helium abundance (number density ratio, $y = \frac{n(\mathrm{He})}{n(\mathrm{H})}$) versus oxygen-to-hydrogen ratio (O/H) plotted. The LBT Y_p Project's uniformly observed and reduced dataset exhibits reduced uncertainties, lower dispersion, and much denser sampling at low metallicities, as well as a greater sample size.

As discussed in Section 6.1 and as is immediately apparent in Figure 17, the increase in the number of targets in the LBT Y_p Project final dataset is dramatic, and, reassuringly, that increase is due in large part to a larger χ^2 qualifying fraction. As discussed in Sections 4 and 6, 47 of 54 targets (87%) pass the 95% CL χ^2 goodness-of-fit test, with six flagged, leaving 41 qualifying points without any flags (76%). Comparing to E. Aver et al. (2015), 19 of 31 targets (61%) pass the 95% χ^2 test, with three of those 19 observations of the same target (SBS 0335–052E) and three targets flagged (including one SBS 0335–052E observation). That left 16 qualifying observations without any flags, 15 of which were unique targets (15 of 29, 52%). Almost tripling from 15 to the current 41 points is a very significant advance in our dataset.

The dramatic improvement in the LBT Y_p Project's dataset is also demonstrated by the significant reduction in the target

uncertainties, which is also clearly evident in Figure 17. Compared to E. Aver et al. (2015), the average uncertainty for y decreased by 47%.

As Figure 17 shows, our target coverage is greater for lower metallicities, reflecting our target selection priorities. That low-metallicity target coverage vastly exceeds E. Aver et al. (2015), with 33 targets compared to 12 for $O/H \leqslant 8 \times 10^{-5}$ (14% of solar). Restricting to even lower metallicities, $O/H \leqslant 4 \times 10^{-5}$ (7% of solar), the LBT Y_p Project dataset still retains an impressive 15 targets, while E. Aver et al. (2015) contained only six.

As seen in Figure 17, for $O/H \leqslant 8 \times 10^{-5}$, there appears to be a degree of intrinsic scatter in our dataset, which is not uncommon with astronomical observations. The sampling for $O/H > 8 \times 10^{-5}$ is limited. With relatively sparse sampling, the degree of intrinsic scatter in that higher-metallicity region may not be fully captured by our dataset. Additionally, the still relatively large dispersion compared to the relatively sparse sampling limits our ability to constrain the rate of chemical evolution, $\Delta y/\Delta(O/H)$. This provides further support for preferring a weighted mean determination for Y_p (see Section 7.3 below).

As noted above, at low metallicities ($O/H \leqslant 8 \times 10^{-5}$), where the bulk of our targets are, there is evidence for significant intrinsic dispersion. This can arise from at least two different causes. First, if we have underestimated our uncertainties, this could result in the appearance of an intrinsic scatter. Alternatively, the intrinsic scatter could be produced by the galaxies following slightly different paths in chemical evolution. We cannot rule out a small underestimate of our uncertainties, but it is worth discussing what might lead to a true intrinsic dispersion in y at a given value of O/H.

Due to the correlation of metallicity with stellar mass (e.g., D. A. Berg et al. 2012), at the lowest values of O/H, the targets are all relatively low-mass galaxies. At these low masses, chemical enrichment is extremely inefficient (e.g., ~5% of the oxygen is retained in Leo P; K. B. W. McQuinn et al. 2015) and thus may be subject to stochastic effects. The nucleosynthetic production of helium and oxygen is expected to have different timescales. Helium production is thought to be significantly driven by asymptotic giant branch (AGB) stars in the mass range of 4–8 $M_\odot$, while oxygen production through supernovae is dominated by stars more massive than 8 $M_\odot$ (e.g., M. K. Weller et al. 2025, their Figure 4 in particular). Thus, the evolution of a single galaxy in the y–O/H diagnostic diagram could take a zigzag path, as was originally envisioned for nitrogen based on a similar timescale argument (D. R. Garnett 1990).

Additionally, many of the lowest-metallicity star-forming galaxies are thought to have exceptionally low metallicities due to the recent infall of relatively pristine gas, as proposed by B. Ekta & J. N. Chengalur (2010) and discussed by K. B. W. McQuinn et al. (2020). Given the above, it is perhaps not surprising to detect an intrinsic dispersion in the values of y at the lowest values of O/H. For the purpose of determining Y_p, the dispersion has the effect that the presumed slope in y versus O/H is more difficult to detect or constrain at the lowest values of O/H.

7.3. Weighted Average for Y_p

The goal of our project is to determine Y_p, and determining Y_p does not require determining the slope, $\Delta y/\Delta(O/H)$ (or $\Delta Y/\Delta(O/H)$), as long as one can sufficiently limit the metallicity baseline, as is discussed further below. Correspondingly, as discussed in Paper I and Section 3, we prioritized the lowest-metallicity targets over a more even coverage across our metallicity range. Given its dispersion, our sample does not contain sufficient higher-metallicity observations to determine the slope, $\Delta y/\Delta(O/H)$, with confidence, as is evident in Figure 17 and will be further explored in Section 7.4. Indeed, from Figure 17, it is evident that our dataset does not exhibit a significant degree of enrichment for low metallicities. However, enabled by our observing strategy, the unprecedented number of low-metallicity yet high-quality optical and NIR observations in our sample allows for a robust weighted average determination of Y_p with unprecedented precision.

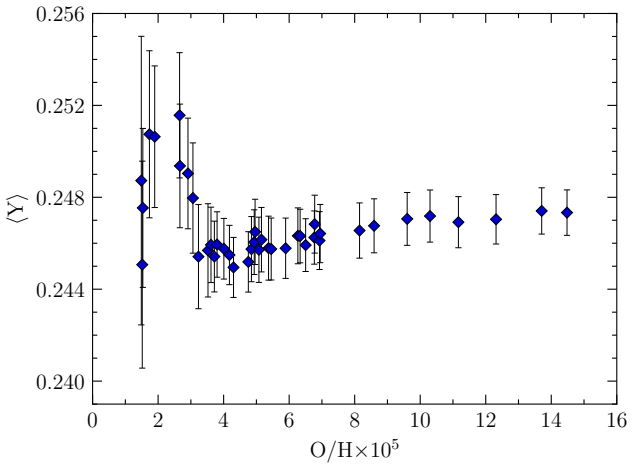


Figure 18. The weighted average value for the helium mass fraction, $\langle Y \rangle$, versus increasing baseline cutoff values for the oxygen-to-hydrogen ratio, O/H, used for calculating the weighted average. The series of weighted average values is calculated from our final qualifying sample (41 targets), and that weighted average is calculated for the helium abundance, y, and then converted to a mass fraction, Y, for easier comparison. Though $\langle Y \rangle$ varies and there is some increase at higher metallicities, the weighted average does not show any significant systematic increase as the metallicity baseline increases, especially within the $O/H = 2.3–7 \times 10^{-5}$ band and within uncertainties.

Over an extended range in metallicity, we expect the helium abundance to increase with metallicity. As a result, the mean of the helium abundance, $\langle Y \rangle$, with $O/H < x$, would be expected to increase with x. In our data, no clear systematic increase in $\langle Y \rangle$ with O/H is observed. This is demonstrated in Figure 18, which plots the weighted mean, $\langle Y \rangle$, calculated for progressively increased O/H cutoffs. This limits the bias in Y_p that one would introduce due to a positive slope from chemical evolution. For comparison, if one assumes a slope of $\Delta Y/\Delta(O/H) = 46$, as determined by the relationship for higher metallicity (O. A. Kurichin et al. 2021), the increase in Y_p introduced by the weighted average would be ~0.0009 (i.e., the midpoint enrichment value of Y over a domain of $O/H \leqslant 4 \times 10^{-5}$), which is less than the uncertainty we find in our result below.

As Figure 18 shows, the running weighted average, $\langle Y \rangle$, for increasing O/H baselines is relatively constant once a suitable number of points is included. Indeed, within the uncertainties, there is little change in the mean for a cutoff of $O/H < 3.3 \times 10^{-5}$ (10 points) and that for $O/H \leqslant 8 \times 10^{-5}$ (33 points). This makes the result relatively insensitive to the choice of cutoff, which is reassuring. In addition, there is little

evidence for the introduction of any significant bias from the weighted average.

To determine Y_p, we first calculate $\langle y \rangle$, the weighted average of the helium abundance (number density ratio) for our $O/H \leqslant 4 \times 10^{-5}$ subsample, to determine y_p, the primordial helium abundance. Then, we convert y_p to Y_p, the primordial helium mass fraction, for easier comparison with the CMB prediction and astrophysical determinations from the literature.

To ensure that our result for Y_p is not subject to the effects of significant chemical evolution, we restrict our metallicity range to $O/H \leqslant 4 \times 10^{-5}$. This limits the bias in Y_p that one would introduce due to a positive slope from chemical evolution (if present). The weighted average of y for those 15 qualifying targets without any flags and $O/H \leqslant 4 \times 10^{-5}$ yields

$$y_p = 0.08146 \pm 0.00058, \tag{2}$$

with a reduced $\chi^2 = 1.315$. The primordial helium abundance, y_p, may be converted to the corresponding mass fraction, Y_p, via

$$Y_p = \frac{4y_p}{1 + 4y_p}, \tag{3}$$

which yields

$$Y_p = 0.2458 \pm 0.0013. \tag{4}$$

Because the reduced χ^2 is slightly larger than 1, the uncertainties in Equations (2) and (4) include an S-factor correction to account for that. This correction and our specific procedure for calculating the mean and uncertainty are described in detail in Appendix G. The reduced χ^2 corresponds to an S factor, $S = 1.15$; that is, the quoted uncertainties have been increased by about 15%. This is a well-established method for accounting for uncertainties that may be underestimated in one or more of the objects, and it simply scales the uncertainties by a common factor (A. H. Rosenfeld 1975; S. Navas et al. 2024). While this correction is nonnegligible, it also indicates that there is not a substantial amount of dispersion in this data subset.

Equation (4) is our primary result for the primordial helium abundance (reported as a mass fraction, as is common convention). Our Y_p determination achieves a relative uncertainty of 0.5%. This is an unprecedented precision and represents the realization of the LBT Y_p Project's primary goal.

The insensitivity of our result to the O/H cutoff is underscored by Figure 19, which plots y versus O/H for our dataset with $O/H \leqslant 8 \times 10^{-5}$, overlaid with the weighted average results for $O/H \leqslant 4 \times 10^{-5}$ and $O/H \leqslant 8 \times 10^{-5}$. Despite doubling the metallicity baseline from $O/H \leqslant 4 \times 10^{-5}$ to $O/H \leqslant 8 \times 10^{-5}$, resulting in more than double the number of points ($N = 33$ versus 15), the weighted average result does not change significantly: $y_p = 0.08175 \pm 0.00056$ and $Y_p = 0.2464 \pm 0.0013$. The uncertainty here is the same as in Equation (4), despite more than twice as many points being averaged. This is due to the increased dispersion (easily seen in Figure 19), and the uncertainty carries a more significant correction of $S = 1.76$. This dispersion may be random or may indicate the presence of nonprimordial contributions to the helium abundance. Without being able to account for this dispersion, we restrict to $O/H \leqslant 4 \times 10^{-5}$ for our weighted average calculation. We also note that the dispersion is minimized (for $N \geqslant 10$) at $N = 15$ and 16 (both give $S = 1.15$). One could argue for an even more restrictive baseline, but that would cut against the need to have a significant number of points for a robust weighted average determination.

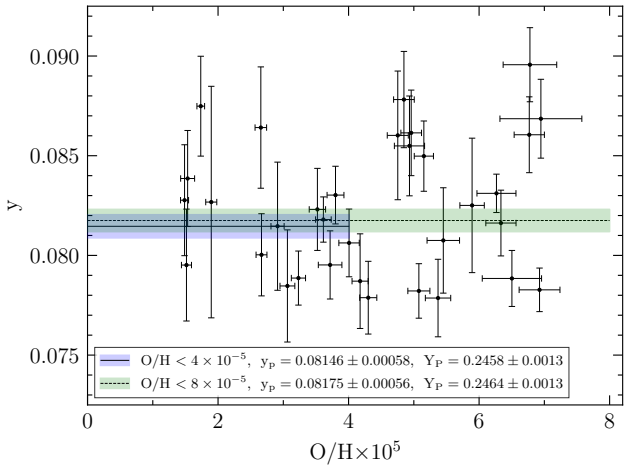


Figure 19. The helium abundance (number density ratio, $y = \frac{n(\mathrm{He})}{n(\mathrm{H})}$) for the 33 targets from our final qualifying dataset with $O/H \leqslant 8 \times 10^{-5}$, plotted versus the oxygen-to-hydrogen ratio (O/H). The horizontal shaded bands show the weighted average, $\langle y \rangle$, with $\pm 1\sigma$ uncertainties. The weighted average for the set of 15 targets with $O/H \leqslant 4 \times 10^{-5}$ is shown by the darker (blue) shaded band, and the weighted average for the set of 33 targets with $O/H \leqslant 8 \times 10^{-5}$ is shown by the lighter (green) shaded band. Despite the doubling of the metallicity baseline (and more than doubling of the number of points, from 15 to 33), the weighted average results are very similar, demonstrating the robustness of the weighted average value with respect to the sample cutoff. For each set, the weighted average results are included (y_p), as well as the corresponding Y_p values.

7.4. Linear Regression to Y_p

Although our primary result for Y_p is given in Equation (4), for completeness and comparison, we also perform a linear regression to determine Y_p. We calculate a regression of y versus O/H, the oxygen abundance, from the full sample of qualifying targets without any flags to extrapolate to the primordial value, y_p. From y_p, we then calculate Y_p, the primordial helium mass fraction. The regression using y, rather than Y, the helium mass fraction, removes the dependence on Z (through $Y = \frac{4y(1-Z)}{1+4y}$) in determining Y_p, as advocated by T. Hsyu et al. (2020).

Our method for regression to y_p is briefly described in Appendix G. We use a weighted least-squares linear regression with uncertainties on both variables (y and O/H). Regression based on the 41 targets in our final qualifying dataset yields

$$y_p = 0.08117 \pm 0.00096, \tag{5}$$

with a slope $\Delta y/\Delta(O/H) = 14 \pm 12$. This corresponds to a primordial helium mass fraction of

$$Y_p = 0.2451 \pm 0.0022. \tag{6}$$

The quoted uncertainties include an S factor, as described in Appendix G, which in this case is $S = 1.70$. The result of the linear regression is shown in Figure 20.

While Equation (6) agrees well with our preferred Y_p result, the weighted average, as given in Equation (4), the data do not allow for an unambiguous determination of a slope, $\Delta y/\Delta(O/H)$. The determination of the slope is almost entirely reliant on the sparse points with $O/H > 8 \times 10^{-5}$, as can been seen in Figure 20. With only 8 of 41 points in the upper half of

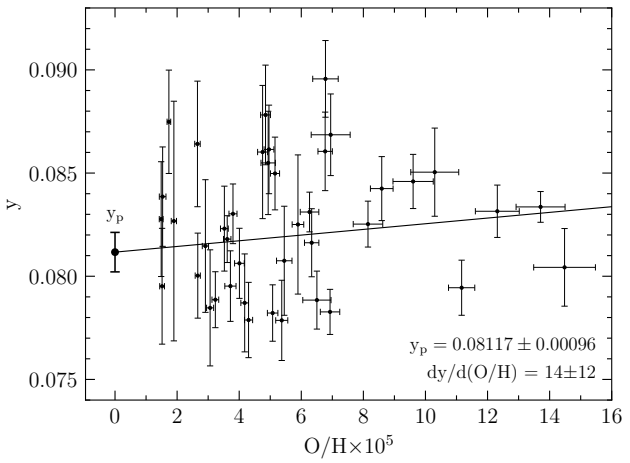


Figure 20. A linear regression of the helium abundance (number density ratio, $y = \frac{n(\mathrm{He})}{n(\mathrm{H})}$) versus oxygen-to-hydrogen ratio (O/H) for the complete final qualifying sample (41 points). The fit line slope, $\Delta y/\Delta(\mathrm{O/H})$, and intercept, y_p, are given.

the regression's metallicity baseline, our ability to reliably extract the slope, $\Delta y/\Delta(\mathrm{O/H})$, is severely limited. This point is reinforced by the dispersion evident in those eight points. Indeed, without the points with $\mathrm{O/H} > 8 \times 10^{-5}$, a determination of the slope of the 33 lowest-metallicity targets yields $\Delta y/\Delta(\mathrm{O/H}) = 15 \pm 36$ ($S = 1.79$), clearly indicating that taking the weighted mean is preferable for the lower-metallicity subset of the data.

V. Fernández et al. (2018) advocate for using sulfur as a metallicity tracer. For our low-metallicity sample, calculating the sulfur abundance requires an ionization correction factor (ICF) to account for the significant but unobserved contribution from S^{+4}. Using S/H rather than O/H does not make any significant difference and returns an almost identical regression result for Y_p ($Y_p = 0.2455 \pm 0.0019$).

Given the indications of intrinsic scatter in our dataset, one can further investigate using the PYTHON LINMIX package,[11] which is briefly described in Appendix G. Using LINMIX for the finally qualifying dataset (41 points) returns $y_p = 0.08184 \pm 0.00110$, with a slope $\Delta y/\Delta(\mathrm{O/H}) = 8 \pm 16$ and intrinsic scatter $\sigma_{\mathrm{int}} = 0.00262 \pm 0.00048$. Once again we see that a nonzero slope cannot be determined with any confidence. The returned intrinsic scatter value indicates significant intrinsic scatter in the dataset. However, it is not clear if the intrinsic random scatter in our dataset is well characterized by a single parameter across the dataset or whether it may vary with metallicity.

The LINMIX y_p translates to $Y_p = 0.2466 \pm 0.0025$. This result agrees well with Equation (6), though the difference illustrates the effect of fitting for intrinsic scatter, or not, on the resulting slope and intercept. The weighted least-squares regression returns a noticeably different slope and intercept than the Bayesian MCMC LINMIX result. This difference in result, depending on the regression algorithm, further cautions against the reliability of using linear regression to determine Y_p for our dataset.

7.5. Y_p Comparisons

The weighted average (Equation (4)) for Y_p agrees well with the standard BBN (SBBN) value, $Y_p = 0.2467 \pm 0.0002$ (T.-H. Yeh et al. 2022, 2023), based on the Planck determination of the baryon density (Planck Collaboration 2020). Equation (4) also agrees well with the SBBN-independent direct Planck estimation of $Y_p = 0.239 \pm 0.013$ (Planck Collaboration 2020) using temperature, polarization, and lensing data, which is not surprising given the relatively large uncertainty on this value from the CMB alone.

E. Aver et al. (2015), our last result prior to the LBT Y_p Project (see Section 6), determined $Y_p = 0.2449 \pm 0.0040$ with a slope of $\Delta Y/\Delta(\mathrm{O/H}) = 79 \pm 43$. Our Y_p results here, from both the weighted average and linear regression, are in very good agreement with the E. Aver et al. (2015) result. The more striking comparison is for the uncertainty. For the linear regression, both results are based on the qualifying sample excluding flagged targets, and the model and analysis methodology employed are quite similar. However, the fruits of this project are evident in the resulting uncertainty. Compared to E. Aver et al. (2015), the uncertainty on Y_p is reduced by 45% based on linear regression (Equation (6)) to achieve a relative uncertainty of <1%.

The regression dataset in E. Aver et al. (2015) only included 15 targets, compared to 41 targets in this work. Furthermore, the average uncertainty for its galactic helium abundance determinations was larger (see Sections 6.1 and 7.2). The combination of decreased uncertainties for the sample points and the increased number of sample points is the primary source of the decreased uncertainty for Y_p.

However, that rather pedestrian statement masks the requirements for achieving those decreased target uncertainties. As discussed in Section 6, it rests on high-SNR, high-resolution, and broad wavelength coverage observations, uniformly observed and reduced and then combined with an expanded physical model. Figure 17 (introduced above in Section 7.2) compares the E. Aver et al. (2015) dataset with the LBT Y_p Project dataset presented in this work. As discussed in Section 7.2, Figure 17 demonstrates the greater number of targets, reduced uncertainties, lower dispersion, and much denser sampling at low metallicities. These advances are the foundation of the LBT Y_p Project's significantly higher-precision Y_p determination.

Though E. Aver et al. (2022) include the first two targets from the LBT Y_p Project, Leo P and AGC 198691, comparing to those results is still of interest, since they are our most recent. Based on 17 targets, E. Aver et al. (2022) determined $Y_p = 0.2448 \pm 0.0033$ with a slope of $\Delta Y/\Delta(\mathrm{O/H}) = 80 \pm 38$. Since 15 of the 17 points were from E. Aver et al. (2015), it is not surprising that the intercept value was largely unchanged from E. Aver et al. (2015). However, the inclusion of Leo P, with its extremely low metallicity and reduced uncertainty for Y, helped to better constrain the intercept. Our Y_p results here are again in good agreement with the E. Aver et al. (2022) determination but with the linear regression Y_p uncertainty decreased by 33%.

The datasets in E. Aver et al. (2015, 2022) did not allow for a reliable weighted average determination based on a low-metallicity subset, due to the paucity of very low-metallicity targets in its dataset (even with Leo P and AGC 198691 added). Comparing our weighted average result here (Equation (4)) to the E. Aver et al. (2015) result for Y_p, the uncertainty shrinks by more than half, decreasing by 67%. Comparing to Y_p from E. Aver et al. (2022), the uncertainty for our weighted average Y_p determination is reduced by 60%.

[11] https://github.com/jmeyers314/linmix

Table 6
Recent Primordial Helium Abundance Results

Citation	Y_P	N	Method
Y. I. Izotov et al. (2014)	0.2551 ± 0.0022	28	H II region
E. Aver et al. (2015)	0.2449 ± 0.0040	15	H II region
A. Peimbert et al. (2016)	0.2446 ± 0.0029	5	H II region
R. J. Cooke & M. Fumagalli (2018)	$0.250^{+0.033}_{-0.025}$	1	Absorption line
M. Valerdi et al. (2019)	0.2451 ± 0.0026	1	H II region
V. Fernández et al. (2019)	0.243 ± 0.005	16	H II region
Planck Collaboration (2020)	0.239 ± 0.013	⋯	CMB
T. Hsyu et al. (2020)	$0.2436^{+0.0039}_{-0.0040}$	54	H II region
O. A. Kurichin et al. (2021)	0.2462 ± 0.0022	120	H II region
A. Matsumoto et al. (2022)	$0.2370^{+0.0034}_{-0.0033}$	59	H II region
Atacama Cosmology Telescope Collaboration (E. Calabrese et al. (2025))	0.2312 ± 0.0092	⋯	CMB
SPT-3G Collaboration (E. Camphuis et al. (2026))	0.2285 ± 0.0085	⋯	CMB
H. Yanagisawa et al. (2026)	0.2402 ± 0.0040	67	H II region
The LBT Y_p Project	0.2458 ± 0.0013	15	H II region
T.-H. Yeh et al. (2022)	0.2467 ± 0.0002	⋯	SBBN + CMB

As illustrated by the comparisons above, the LBT Y_p Project's weighted average determination is a significant advance in primordial helium abundance determinations, achieving a relative uncertainty of 0.5%. Furthermore, it highlights the value and diagnostic power provided by assembling a dataset with many very low-metallicity targets.

A comparison of our result with other recent determinations is found in Table 6 and plotted in Figure 21. It is encouraging that almost all of the most recent results agree. The only one not in agreement with all of the others within the 2σ level, including with our results presented here, is Y. I. Izotov et al. (2014).[12] E. Aver et al. (2015) include a detailed description of the differences in the methodology and dataset cuts between Y. I. Izotov et al. (2014) and our model and approach. The recent CMB-based determinations from the Atacama Cosmology Telescope Collaboration (E. Calabrese et al. (2025)) and the SPT-3G Collaboration (E. Camphuis et al. (2026)) show notably lower values for Y_p, but, due to their larger uncertainties, they still agree with the other more recent results, including our results here, within the 2σ level. For H II–region-based determinations, apart from the aforementioned Y. I. Izotov et al. (2014), they all agree with each other and with our results presented in this work within the 1σ level, except for A. Matsumoto et al. (2022), but those results do agree with the others and with our results here at 2σ.

8. Future Investigations

Two avenues for future investigation and potentially improving our H II region modeling are directly motivated by our results above: our temperature model and the Case B assumption for the He singlet emission lines. Each could potentially introduce a systematic error in our analysis, and further investigation is warranted. However, those explorations and any potential wholesale updates to our current temperature or radiative transfer models are beyond the scope of this work.

[12] O. A. Kurichin et al. (2021) reanalyze Y. I. Izotov et al. (2014) and find a value in closer agreement with the other determinations.

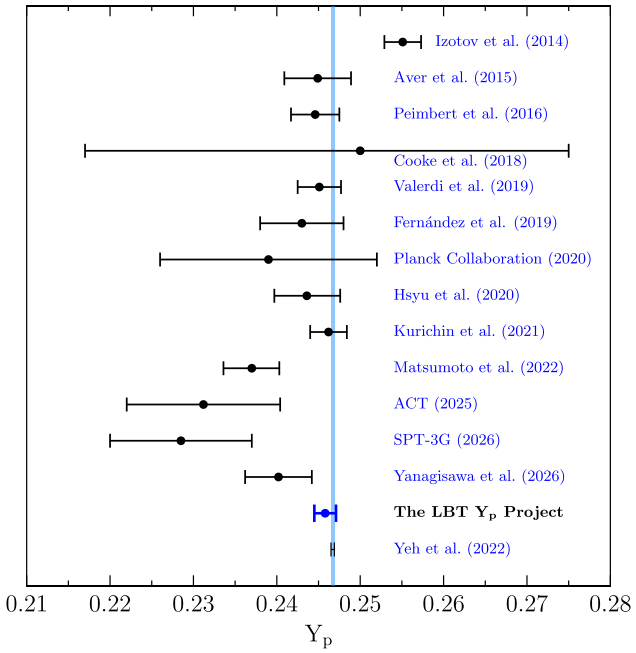


Figure 21. A comparison of recent Y_p results. The SBBN result based on the Planck-determined baryon density (Planck Collaboration 2020) is plotted as a vertical band in light blue (T.-H. Yeh et al. 2022, 2023). The uncertainty for the LBT Y_p Project result is reduced, yet it remains in good agreement with most of the recent results.

The subsections below discuss the evidence for potential deficiencies in our current temperature model (Section 8.1), as well as expanding upon the previous discussion (Section 2.3) of the discrepant He singlet emission lines, He I λ5016 and λ7281 (Section 8.2).

8.1. Temperature Model

As discussed in Section 5.3, T(He), a fit parameter in our model, as determined by the He emission lines, would be expected to closely track T(O III), as determined by the [O III] emission lines. However, due to potential temperature inhomogeneities, T(O III) could be biased upward compared to T(He) (M. Peimbert et al. 2000; A. Peimbert et al. 2002; K. A. Olive & E. D. Skillman 2004; E. Aver et al. 2011; J. E. Méndez-Delgado et al. 2025). This is the primary motivation for including T(He) as a model parameter to fit from the He emission lines themselves, rather than adopting T(O III) as the appropriate T_e for calculating the He and H emissivities and He radiative transfer (M. Peimbert et al. 2000; K. A. Olive & E. D. Skillman 2004). However, as shown in Figure 8, our results do not demonstrate a systematic discrepancy between T(O III) and T(He). There is some evidence for a systematically higher value for T(O III) than T(He) for the higher-temperature qualifying points in our sample, but it is not definitive.

Therefore, the results from our dataset suggest further investigation of the temperature structure and relationships for the H II regions in our sample. That work will build upon the detailed temperature analysis in Paper II and focus on improving our temperature model for the He emission. It is possible that T(O III) is not a biased measurement for T(He), and if so, the much higher precision of T(O III) offers an avenue for decreasing the uncertainty on the helium abundance. In addition, previous studies have advocated for the

importance of temperature structure and potential inhomogeneities in H II regions (M. Peimbert 1967; M. Peimbert et al. 2000; A. Peimbert et al. 2002), and further investigation of these effects could lead to potential improvements in our model.

8.2. He I λ5016 and λ7281 Testing

Section 2.3 discussed the systematic discrepancies in He I λ5016 and λ7281. This was first reported by Y. I. Izotov et al. (2014), and J. E. Méndez-Delgado et al. (2025) suggest deviations from Case B due to photon loss and/or temperature inhomogeneities as plausible causes. Further examination of the effects of potential temperature inhomogeneities (or lack thereof) is already motivated by the comparison of T(He) and T(O III) for our sample, as discussed above (Section 8.1). If the observed He I λ5016 and λ7281 fluxes are systematically decreased due to photon loss caused by H I absorption or escape from the H II region, that would have consequences for all of the He singlet lines, including He I λλ4922, 6678, and 4388, though to a significantly reduced degree. We did not observe the same systematically low fluxes for those three He lines (compared to the predicted fluxes) as we did for He I λ5016 and λ7281. However, given the potential for the systematic error, further study is warranted. J. E. Méndez-Delgado et al. (2025) create a toy model that combines Case A and Case B emission to test the hypothesis of deviation from Case B due to photon loss. For the J. E. Méndez-Delgado et al. (2025) sample of H II regions, though not for star-forming galaxies or planetary nebulae, this toy model's predictions are consistent with the observed discrepancy. Expanded investigation of the assumption of Case B for H II region modeling building off the "Case A + B" toy model may be a natural place to start.

9. Conclusions

The primary goal of the LBT Y_p Project is to determine the primordial helium abundance with the highest precision yet achieved. Through a carefully designed observing program leveraging the high resolution, high SNR, and broad wavelength coverage offered by the LBT, we have achieved that goal, determining Y_p with a precision of 0.5%. Our dataset is the largest high-quality optical and NIR sample for helium abundance analysis yet assembled. Our dataset shows significantly improved statistical reliability compared to previous datasets, and we have taken care to flag targets for potential systematic errors. Along the way, we have updated our model to employ the latest atomic data, as well as incorporating refinements to our methodology. Here is a brief summary of the major advances and results presented in this paper.

1. The latest helium emissivity calculations from G. Del Zanna & P. J. Storey (2022) have been incorporated, using a higher-resolution temperature and density grid. Similarly, the latest hydrogen emissivity calculations from P. J. Storey & T. Sochi (2015) have been incorporated using a higher-resolution temperature and density grid. The H emissivities are almost identical in the low-density regime relevant for this work, and the new He emissivities are broadly similar to those that preceded them. This consistency provides greater confidence in the results from our model.
2. Our radiative transfer model has been updated with the (very) recent radiative transfer calculations by KI26. These new calculations are based on the latest atomic data and significant modeling improvements. Demonstrating the improvements in these new radiative transfer calculations, our results show better agreement between our model and the observations, especially for higher optical depth systems.
3. Our model was expanded to incorporate three additional Paschen series lines (P13, P14, and P15) for greater diagnostic power and flexibility. We improved our treatment of the blended emission H8 + He I λ3889 line, and, due to the exponential temperature dependence for collisional excitation of neutral hydrogen, we excluded the neutral hydrogen fraction as a fit parameter for temperatures below 14,000 K, where collisional enhancement is negligible. Based on the recent findings of J. E. Méndez-Delgado et al. (2025), we excluded He I λ5016 and λ7281 from our analysis, due to systematic discrepancies in their observed fluxes compared to standard Case B modeling and assumed temperature homogeneity.
4. Many previous helium abundance analyses exhibited the disturbing result that a large fraction, typically the majority, of the observations failed a 95% CL χ^2 test. From our starting dataset of 54 observations, 47 passed a 95% CL χ^2 test, equating to 87% of the dataset. This is a very significant improvement upon previous datasets. Furthermore, of the seven targets excluded by the χ^2 test, the majority exhibited behavior in their spectra that would make them unsuitable, such that their failure was not surprising. This dramatic improvement in the statistical reliability of our dataset can be directly attributed to our uniformly observed and reduced spectra combined with our high-fidelity flux measurements and error model. Our sample's much higher qualifying fraction bolsters our confidence in our applied model and thus the results.
5. We examined our dataset for potential systematic biases and conservatively flagged targets where there were concerns that they may introduce systematic error into our results. Six targets in total were flagged, one for optical depth, two for underlying helium absorption, and three for the divergence between their helium and [O III] temperatures.
6. Following directly from the quality of our observations and measurements, we were able to deploy our full model employing up to 24 lines, with the effect that the average uncertainty on the helium abundance (y) for the LBT Y_p Project dataset decreased by 47% compared to our previous dataset and analysis.
7. We specifically targeted the lowest-metallicity H II regions with sufficient signal strength to produce high-SNR spectra. As a result, our final dataset for determining Y_p is a subset of the total sample, consisting of the 15 targets with the lowest metallicities, $O/H \leqslant 4 \times 10^{-5}$. This singular advance allows us to determine Y_p using a weighted average, thus removing the assumption of linear enrichment. We note that, due to our reduced uncertainties on the individual data points, we detect a significant dispersion in y within our sample.

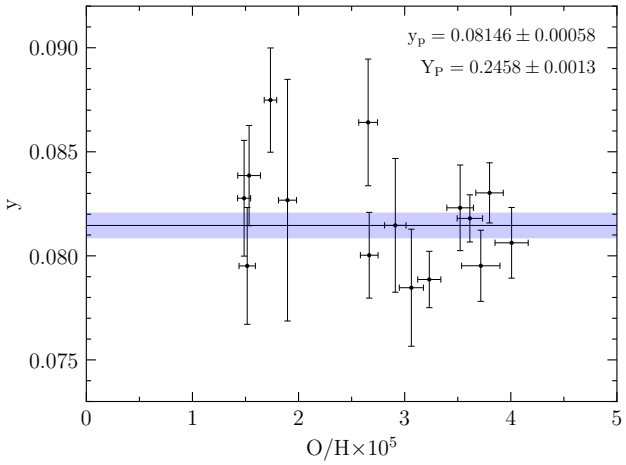


Figure 22. The helium abundance (number density ratio, $y = \frac{n(\mathrm{He})}{n(\mathrm{H})}$) for the 15 targets in our final qualifying dataset with $\mathrm{O/H} \leqslant 4 \times 10^{-5}$ plotted versus the oxygen-to-hydrogen ratio (O/H). The weighted average, $\langle y \rangle$, with $\pm 1\sigma$ uncertainties is shown by the darker (blue) shaded band. The weighted average result for $\mathrm{O/H} \leqslant 4 \times 10^{-5}$ is provided (y_p), as well as the corresponding Y_p value.

8. Figure 22 presents our final, low-metallicity dataset, with y plotted versus O/H, and our resulting Y_p determination. Our resulting value, $Y_p = 0.2458 \pm 0.0013$, attains the unprecedented precision of 0.5%. This value is in good agreement with the BBN prediction, based on the Planck determination of the baryon density. The implications of this result will be explored in the next paper in this series (Paper V).
9. Our results demonstrate the power of a large dataset of high-quality spectra of very low-metallicity targets. As such, adding more high-SNR, high-resolution optical and NIR observations of the lowest-metallicity targets remains our highest priority for further improvements in our Y_p determination. We think our work demonstrates that is the future for primordial helium abundance determinations.

Acknowledgments

We are grateful to the anonymous referee for the thorough, thoughtful review and very helpful suggestions, which have significantly improved the clarity and depth of this manuscript.

This work was supported by funds provided by NSF Collaborative Research grants AST-2205817 to R.W.P., AST-2205864 to E.D.S., and AST-2205958 to E.A. Our team workshop at OSU in 2024 July was sponsored in part by OSU's Center for Cosmology and AstroParticle Physics (CCAPP). The work of K.A.O. was supported in part by DOE grant DE-SC0011842 at the University of Minnesota. E.A. benefited greatly from multiple visits to the University of Minnesota and is grateful to the University of Minnesota and the William I. Fine Theoretical Physics Institute for the support.

The authors owe special thanks to Giulio Del Zanna and Peter Storey for providing their He and H emissivity calculations, respectively, on a finer grid.

Our team greatly appreciated the invitation, discussion, and feedback at the 2025 May CERN and EuCAPT workshop, *News, Opportunities and Challenges in Big Bang Nucleosynthesis*.

This paper uses data taken with the MODS spectrographs built with funding from NSF grant AST-9987045 and the NSF Telescope System Instrumentation Program (TSIP), with additional funds from the Ohio Board of Regents and the Ohio State University Office of Research. This paper made use of the modsIDL spectral data reduction pipeline developed in part with funds provided by NSF grant AST-1108693.

This work is based on observations made with the Large Binocular Telescope. The LBT is an international collaboration among institutions in the United States, Italy, and Germany. LBT Corporation members are the University of Arizona on behalf of the Arizona Board of Regents; Istituto Nazionale di Astrofisica, Italy; LBT Beteiligungsgesellschaft, Germany, representing the Max-Planck Society, the Leibniz Institute for Astrophysics Potsdam, and Heidelberg University; the Ohio State University; and the Research Corporation, on behalf of The University of Notre Dame, University of Minnesota, and University of Virginia. Observations have benefited from the use of ALTA Center (alta.arcetri.inaf.it) forecasts performed with the Astro-Meso-Nh model. Initialization data of the ALTA automatic forecast system come from the General Circulation Model (HRES) of the European Centre for Medium Range Weather Forecasts.

This research used the facilities of the Italian Center for Astronomical Archive (IA2) operated by INAF at the Astronomical Observatory of Trieste.

All LBT observations for this project were executed remotely beginning during the global COVID-19 pandemic, when we all learned together how to operate the LBT from basements, spare bedrooms, and home offices. We are most grateful for the tireless efforts of the Mount Graham and Tucson technical and observing support staff of the Large Binocular Telescope Observatory who were critical to making it all work smoothly, keeping telescopes and instruments operating in top form under trying circumstances. The 130 hr of high-quality, consistent spectrophotometric data acquired for this project would not have been possible without them.

E.D.S., K.A.O., E.A., D.A.B., N.S.J.R., and J.H.M. would like to acknowledge and thank Stanley Hubbard for his generous gift to the University of Minnesota that allowed the university to become a member of the LBT collaboration.

This research has made use of the NASA/IPAC Extragalactic Database (NED), which is operated by the Jet Propulsion Laboratory, California Institute of Technology, under contract with the National Aeronautics and Space Administration and the NASA Astrophysics Data System (ADS).

Facility: LBT (MODS), LBT (LUCI).

Software: `astropy` (Astropy Collaboration et al. 2013, 2018, 2022), `jupyter` (T. Kluyver et al. 2016), `modsIDL` (K. V. Croxall & R. W. Pogge 2019), `modsCCDRed` (R. Pogge 2019), `PyNeb` (V. Luridiana et al. 2012, 2015), `numpy` (C. R. Harris et al. 2020), `PypeIt` (J. Prochaska et al. 2020; J. X. Prochaska et al. 2020).

Appendix

The extensive Appendices in E. Aver et al. (2021) provide our entire model and the data employed, including the model equations for the helium and hydrogen flux ratios. The following Appendices provide the corresponding updates to the equations and data provided in the E. Aver et al. (2021) appendices. These Appendices should be read as a supplement to the E. Aver et al. (2021) Appendices to bring them up to date with our model and data as employed in this work.

Appendix A
The Blended Emission Line H8 + He I λ3889

As discussed in Section 2, the treatment of the blended emission line H8 + He I λ3889 has been revised. Correspondingly, Equation (A.8) from E. Aver et al. (2021) is replaced by the following:

$$\frac{F(\mathrm{He3889+H8})}{F(\mathrm{H}\beta)} = y^{+}\frac{E(\mathrm{He3889})}{E(\mathrm{H}\beta)}\frac{\frac{W(\mathrm{H}\beta)+a_{\mathrm{H}}(\mathrm{H}\beta)}{W(\mathrm{H}\beta)}}{\frac{W(\mathrm{He3889})+a_{\mathrm{He}}(\mathrm{He3889})}{W(\mathrm{He3889})}} \times f_{\tau}(\mathrm{He3889})\frac{1}{1+\frac{C}{R}(\mathrm{H}\beta)}10^{-f(\mathrm{He3889})\,C(\mathrm{H}\beta)} + \frac{E(H8)}{E(H\beta)}\frac{\frac{W(\mathrm{H}\beta)+a_{\mathrm{H}}(\mathrm{H}\beta)}{W(\mathrm{H}\beta)}}{\frac{W(\mathrm{H8})+a_{\mathrm{H}}(\mathrm{H8})}{W(\mathrm{H8})}}\frac{1+\frac{C}{R}(\mathrm{H8})}{1+\frac{C}{R}(\mathrm{H}\beta)}10^{-f(\mathrm{H8})\,C(\mathrm{H}\beta)}. \tag{A1}$$

Following the steps in the E. Aver et al. (2021) Appendix, Equation (A1) can be reexpressed to remove $W(\lambda)$ entirely, based on the constrained flux of the continuum at each wavelength, $h(\lambda)$. This allows one to solve for a consistent emission line ratio relative to Hβ and yields a simplified equation for the flux ratio, replacing Equation (A.17) from E. Aver et al. (2021):

$$\frac{F(\mathrm{He3889+H8})}{F(\mathrm{H}\beta)} = \left(y^{+}\frac{E(\mathrm{He3889})}{E(\mathrm{H}\beta)}f_{\tau}(\mathrm{He3889}) + \frac{E(\mathrm{H8})}{E(\mathrm{H}\beta)}\left(1+\frac{C}{R}(\mathrm{H8})\right)\right) \times \frac{W(\mathrm{H}\beta)+a_{\mathrm{H}}(\mathrm{H}\beta)}{W(\mathrm{H}\beta)}\frac{1}{1+\frac{C}{R}(\mathrm{H}\beta)}10^{-f(\mathrm{He3889+H8})\,C(\mathrm{H}\beta)} - \frac{(a_{\mathrm{He}}(\mathrm{He3889})+a_{\mathrm{H}}(\mathrm{H8}))}{W(\mathrm{H}\beta)}\frac{h(\mathrm{He3889+H8})}{h(\mathrm{H}\beta)}. \tag{A2}$$

For both Equation (A1) and Equation (A2), the only change is the removal of the f_{τ}(He3889) term from the H8 flux contribution. The modeling and treatment of the blended emission line He I λ3889 + H8 had been improved in E. Aver et al. (2021) by treating it as a blended line in the model, rather than subtracting the theoretical flux expected for H8 from the measured, blended flux. As a result, the theoretical flux was then found by summing the contributions from He I λ3889 and H8. In calculating the H8 flux, the He I λ3889 radiative transfer term was included due to the two lines only being separated by 0.4 Å. However, even with estimated Doppler broadening of ∼0.4 Å, only a small fraction of the H8 emission would have a wavelength that would match the He I λ3889 absorption wavelength. Furthermore, in terms of the relative effect of that absorption for H8 compared to He I λ3889, it would be diluted by the much smaller number of He atoms per unit volume compared to H atoms (more than 10 times less). Correspondingly, the absorption of H8-emitted photons by He is expected to be relatively rare, with negligible impacts on the H8 or He fluxes (He I λλ3889, 7065, 10830).

Appendix B
He Emissivities

The He emissivities used in this work are based on the calculations of G. Del Zanna & P. J. Storey (2022). They are parameterized and incorporated identically to the He emissivities in E. Aver et al. (2021), which are from E. Aver et al. (2013). The only change for this work is the updated emissivity grid point values, based on the improved results of G. Del Zanna & P. J. Storey (2022), as discussed in Section 2.1. Those emissivities, as calculated on a higher-resolution temperature and density grid by G. Del Zanna (private communication), are available from the authors upon request.

The finer parametric grid is the same as was implemented in E. Aver et al. (2013) and is summarized in the E. Aver et al. (2021) Appendix. The helium emissivities are functions of the electron temperature and density, T_{e} and n_{e}, respectively. The temperatures for the finer grid are in 250 K increments from 10,000 to 25,000 K (inclusive), and 31 electron densities are irregularly spaced from 1 to 10,000 cm^{-3} (also inclusive), with tighter sampling at the lower densities most relevant for helium abundance analysis.

The helium emissivity ratio, $\frac{E(\lambda)}{E(\mathrm{H}\beta)}$, is then found by interpolation on the finer parametric grid. Measured and theoretical fluxes for He I λ10830 are calculated relative to Pγ, rather than Hβ. Correspondingly, the emissivity ratio for He I λ10830, $\frac{E(\lambda)}{E(\mathrm{P}\gamma)}$, is calculated using the Pγ emissivity, instead of the Hβ emissivity, and then interpolated on the finer parametric grid.

Appendix C
H Emissivities

The H emissivities for this work are based on the calculations of P. J. Storey & T. Sochi (2015). They are parameterized and incorporated identically to E. Aver et al. (2021), but the fits are now based on the updated results of P. J. Storey & T. Sochi (2015), as discussed in Section 2.1. Those emissivities, as calculated on a higher-resolution temperature and density grid by P. Storey (private communication), are available from the authors upon request. The updated fit equations for the H emissivity ratios are provided below.

For all the Balmer lines and for the optical/NIR Paschen lines in the LBT/MODS spectrum (P8–P15), the emissivity ratio is calculated relative to Hβ, $\frac{E(\lambda)}{E(\mathrm{H}\beta)}$. For the IR Paschen lines from the LBT/LUCI spectrum (Pβ and Pδ), the emissivity ratio is calculated relative to Pγ, $\frac{E(\lambda)}{E(\mathrm{P}\gamma)}$, though P$\beta$ and Pδ are not currently used in our analysis. Using the definition $T_4 = T_{\mathrm{e}}/10^4$, the functional form of the fits is as follows:

$$\frac{E(\lambda)}{E(\mathrm{H}\beta|\mathrm{P}\gamma)} = \sum_{ij} c_{ij}(\log(T_4))^{i}(\log(n_{\mathrm{e}}))^{2j}. \tag{C1}$$

Table C1 lists the coefficients, c_{ij}, and replaces Table 6 in the E. Aver et al. (2021) Appendix.

Table C1
Hydrogen Emissivities Coefficients

Line	$i\downarrow$	$j\rightarrow$		
		0	1	2
Hα	0	2.87	−1.36E-3	−5.84E-6
	1	−0.506	4.08E-3	1.69E-5
	2	0.335	−4.19E-3	−1.14E-5
Hγ	0	0.468	3.83E-5	9.02E-7
	1	2.90E-2	−1.23E-4	−2.64E-6
	2	−1.71E-2	1.13E-4	1.15E-6
Hδ	0	0.259	2.67E-5	7.54E-7
	1	2.19E-2	−8.91E-5	−2.61E-6
	2	−1.34E-2	7.12E-5	1.51E-6
H8	0	0.105	9.69E-6	6.33E-7
	1	9.48E-3	−4.47E-5	−1.83E-6
	2	−6.43E-3	3.23E-5	9.78E-7
H9	0	7.31E-2	4.42E-6	7.59E-7
	1	6.29E-3	−3.06E-5	−1.83E-6
	2	−4.50E-3	1.95E-5	1.11E-6
H10	0	5.30E-2	−3.07E-7	1.01E-6
	1	4.26E-3	−2.05E-5	−1.95E-6
	2	−3.22E-3	1.38E-5	1.12E-6
H11	0	3.97E-2	−4.80E-6	1.37E-6
	1	2.93E-3	−1.12E-5	−2.30E-6
	2	−2.34E-3	5.26E-6	1.53E-6
H12	0	3.05E-2	−9.48E-6	1.84E-6
	1	2.06E-3	−2.73E-6	−2.80E-6
	2	−1.73E-3	−5.29E-8	1.84E-6
Pβ	0	1.81	−4.25E-4	−6.62E-6
	1	−0.173	1.08E-3	1.73E-5
	2	8.55E-2	−9.08E-4	−1.26E-5
Pδ	0	0.613	5.55E-5	1.50E-6
	1	2.85E-2	−1.31E-4	−4.29E-6
	2	−1.30E-2	7.84E-5	3.56E-6
P8	0	3.66E-2	−1.45E-6	−9.59E-8
	1	−8.54E-3	−9.02E-7	1.16E-7
	2	−1.05E-3	6.19E-6	−2.23E-8
P9	0	2.54E-2	−5.02E-7	−8.02E-9
	1	−5.61E-3	−2.19E-6	−1.08E-7
	2	−9.68E-4	5.76E-6	1.17E-7
P10	0	1.84E-2	−2.99E-7	5.47E-8
	1	−3.95E-3	−1.61E-6	−2.89E-7
	2	−7.90E-4	3.47E-6	3.22E-7
P11	0	1.38E-2	−5.26E-7	1.21E-7
	1	−2.91E-3	−4.06E-7	−4.62E-7
	2	−6.21E-4	1.53E-6	4.83E-7
P12	0	1.06E-2	−9.50E-7	1.94E-7
	1	−2.23E-3	1.24E-6	−6.65E-7
	2	−4.83E-4	−5.68E-7	6.89E-7
P13	0	8.32E-3	−1.56E-6	2.82E-7
	1	−1.76E-3	3.26E-6	−9.03E-7
	2	−3.73E-4	−3.09E-6	9.37E-7
P14	0	6.66E-3	−2.32E-6	3.86E-7
	1	−1.42E-3	5.45E-6	−1.18E-6
	2	−2.89E-4	−5.42E-6	1.21E-6
P15	0	5.41E-3	−3.20E-6	5.07E-7
	1	−1.17E-3	7.71E-6	−1.47E-6
	2	−2.25E-4	−7.59E-6	1.49E-6

Note. Fit coefficients for the hydrogen emissivities, c_{ij}, in Equation (C1).

As discussed in Sections 2.1 and 6.2, the fit equations for the emissivities of Hβ and Pγ, E(Hβ) and E(Pγ), have been updated based on the newest P. J. Storey & T. Sochi (2015) calculations and the higher-resolution density and temperature grid. Equation (C2) replaces Equation (A.21) from E. Aver et al. (2021), and Equation (C3) replaces Equation (A.22):

$$\begin{aligned} E(\mathrm{H}\beta) = [&-2.79258 \times 10^5 + 3.69812 \times 10^4 \ln T_\mathrm{e} \\ &- 1.47201 \times 10^3 (\ln T_\mathrm{e})^2 + \frac{6.98598 \times 10^5}{\ln T_\mathrm{e}}\Bigg] \frac{1}{T_\mathrm{e}} \\ &\times \left[1.0 + 87.55976 (\log_{10} n_\mathrm{e})^2 \times T_\mathrm{e}^{-1.34756}\right] \\ &\times 10^{-25} \ \mathrm{erg\ cm^3\ s^{-1}}, \end{aligned} \tag{C2}$$

$$\begin{aligned} E(\mathrm{P}\gamma) = [&6.04710 \times 10^4 + 8.96867 \times 10^2 \ln T_\mathrm{e} \\ &- 2.59600 \times 10^2 (\ln T_\mathrm{e})^2 - \frac{3.27429 \times 10^5}{\ln T_\mathrm{e}}\Bigg] \frac{1}{T_\mathrm{e}} \\ &\times \left[1.0 + 3.37185 \times 10^3 (\log_{10} n_\mathrm{e})^2 \times T_\mathrm{e}^{2.11469}\right] \\ &\times \mathrm{SIGN}(3.0 \times 10^4 - 5.0 \times 10^4 \log_{10} n_\mathrm{e} - T_\mathrm{e}) \\ &\times (|3.0 \times 10^4 - 5.0 \times 10^4 \log_{10} n_\mathrm{e} - T_\mathrm{e}|)^{1/4} \\ &\times 10^{-26} \ \mathrm{erg\ cm^3\ s^{-1}}. \end{aligned} \tag{C3}$$

Appendix D
Radiative Transfer

The radiative transfer calculations employed in this work come from KI26, as discussed in Section 2.2. Radiative transfer affects the He triplet lines, and the correction to the He fluxes for radiative transfer is given by $f_\tau(\lambda)$ and depends on the H II region's optical depth, τ, as well as electron density and temperature, n_e and T_e. The calculations are parameterized in terms of the optical depth for He I λ3889 at line center, such that the model parameter, τ, represents the optical depth for He I λ3889 (i.e., $\tau = \tau_{3889}$). KI26 helpfully provide fit equations for $f_\tau(\lambda)$ over the parameter ranges $8000\ \mathrm{K} < T_\mathrm{e} < 22{,}000\ \mathrm{K}$, $1\ \mathrm{cm^{-3}} < n_\mathrm{e} < 10{,}000\ \mathrm{cm^{-3}}$, and $0 < \tau < 10$ with an accuracy of $\lesssim$0.1%. Those fit equations replace Equation (A.24) from E. Aver et al. (2021) and are reproduced below from KI26, with the fit coefficients reproduced in Table D1:

$$f_\tau(n_\mathrm{e}, T_\mathrm{e}) = \frac{1 + a(n_\mathrm{e}, T_\mathrm{e}) \times \tau}{1 + b \times \tau}, \tag{D1}$$

with

$$a(n_\mathrm{e}, T_\mathrm{e}) = \sum_{i=0}^{5} A_i(T_\mathrm{e}) x^i\ , \quad x = \log_{10}\left(\frac{n_\mathrm{e}}{10^2\ \mathrm{cm^{-3}}}\right).$$

Table D1
Radiative Transfer Coefficients

	B_0	B_1	B_2	B_3
		λ3889, b = 5.854E-02		
A_0	7.399E-04	2.506E-04	−2.762E-04	1.422E-04
A_1	1.806E-04	−3.057E-04	−8.839E-05	1.853E-04
A_2	−9.546E-05	1.822E-05	−3.319E-04	2.257E-04
A_3	−9.595E-05	−3.434E-05	−2.756E-04	4.107E-04
A_4	4.975E-05	−1.233E-04	2.953E-05	1.700E-04
A_5	−2.042E-06	4.591E-05	4.476E-05	−1.138E-04
		λ4026, b = −9.988E-03		
A_0	−9.095E-03	7.274E-04	3.047E-04	−7.155E-05
A_1	1.007E-04	−7.632E-05	9.027E-05	−4.993E-04
A_2	3.797E-06	−5.135E-06	1.064E-04	−6.808E-04
A_3	−3.394E-05	1.106E-05	−1.811E-04	−3.631E-04
A_4	1.486E-05	−2.175E-05	−1.611E-04	1.065E-04
A_5	−1.713E-06	4.692E-06	6.341E-05	7.705E-05
		λ4471, b = 2.118E-03		
A_0	4.204E-03	9.874E-04	8.248E-04	−3.394E-04
A_1	−5.567E-04	4.938E-04	−4.527E-04	−8.866E-04
A_2	4.332E-05	−4.700E-05	8.129E-05	−1.352E-03
A_3	1.922E-04	−2.217E-04	−6.444E-05	−4.032E-04
A_4	−8.242E-05	5.455E-05	−2.957E-04	4.713E-04
A_5	7.268E-06	5.672E-06	9.692E-05	−2.058E-06
		λ5876, b = 4.068E-02		
A_0	4.507E-02	3.753E-03	1.882E-03	−1.899E-03
A_1	−2.264E-04	−1.975E-04	−1.024E-03	−5.707E-03
A_2	8.758E-05	−3.356E-04	−1.676E-03	−5.033E-03
A_3	9.324E-05	−3.737E-04	−1.951E-03	4.196E-03
A_4	−7.755E-05	−8.592E-05	−3.971E-04	4.138E-03
A_5	1.304E-05	8.815E-05	5.352E-04	−1.834E-03
		λ7065, b = 5.461E-02		
A_0	2.361E-01	−8.759E-02	−5.182E-02	8.783E-02
A_1	−1.132E-02	−6.569E-02	−2.734E-02	1.896E-01
A_2	−1.440E-02	−7.036E-02	5.927E-02	1.441E-01
A_3	−6.555E-03	6.632E-03	1.216E-01	−1.965E-01
A_4	1.941E-03	3.070E-02	1.702E-02	−1.396E-01
A_5	9.679E-04	−8.075E-03	−3.082E-02	7.805E-02
		λ10830, b = 6.368E-02		
A_0	7.667E-02	−5.558E-03	−6.043E-03	1.144E-02
A_1	−5.435E-03	−1.455E-02	1.262E-02	3.525E-03
A_2	−3.630E-03	1.509E-03	3.039E-02	−3.820E-02
A_3	1.018E-03	7.582E-03	−8.689E-03	−3.769E-03
A_4	1.281E-03	−4.800E-04	−1.722E-02	2.311E-02
A_5	−4.396E-04	−9.710E-04	6.709E-03	−6.684E-03

Note. Fit coefficients b and $B_j^{(i)}$ for the optical depth correction function (Equation (D1)), as given in and reproduced from KI26.

Appendix E
Wavelength-dependent Underlying Stellar Absorption

E. Aver et al. (2021) include coefficients for scaling relative underlying stellar absorption contributions to the set of He emission lines employed in that work. Those coefficients were calculated using spectral energy distributions from BPASS (J. J. Eldridge & E. R. Stanway 2009; J. J. Eldridge et al. 2017; E. R. Stanway & J. J. Eldridge 2018). Because Leo P did not include detections for He I λ4388 and λ7281, scaling coefficients for those emission lines were not included. The scaling coefficients for those two lines are 0.707 and 0.165, respectively. As discussed above (Section 2.3), He I λ7281 and He I λ5016 are not utilized in our analysis here, due to evidence of systematic bias in these lines (J. E. Méndez-Delgado et al. 2025).

Appendix F
Hydrogen Emission Lines Paschen Series P13–P15

As enabled by the high resolution and broad wavelength coverage of MODS, Paschen series emission lines P8–P12 were observed and utilized for the analysis of Leo P in E. Aver et al. (2021). Many of the H II regions in our galactic survey for this work have sufficient SNR to allow clear detections of P13, P14, and P15. As a result, they were added to our model. The H emissivity fit equation coefficients for P13–P15 have already been included along with the other employed H emission lines in Table C1 above.

As with all of our other emission lines, the reddening coefficients, $f(\lambda)$, found in the terms $10^{-f(\lambda)C(\mathrm{H}\beta)}$, are calculated from the extinction fits of J. A. Cardelli et al. (1989) using $R = 3.1$ ($R = \frac{A(V)}{E(B-V)}$).

For modeling underlying absorption in terms of equivalent width, the Paschen lines are scaled relative to Pγ. For the Paschen lines, the ratios were all very close to unity. The deviations from unity in the averages between the Paschen lines were not established to be significant; instead, the deviations may be dominantly due to random variation. As a result, the underlying absorption correction (in terms of equivalent width) for all of the Paschen lines, including P13, P14, and P15, is taken to be the same, with no variation by line/with wavelength.

For the contribution to the hydrogen fluxes from neutral hydrogen collisional excitation, the relative amount of collisional-to-recombination emission can be calculated as follows:

$$\frac{C}{R}(\lambda) = \xi_4 \times 10^{-4} \times \frac{K_{\mathrm{eff}}}{\alpha_{\mathrm{eff}}} = \xi_4 \times \sum_i a_i \exp\left(-\frac{b_i}{T_4}\right) T_4{}^{c_i}, \tag{F1}$$

where $\xi = \frac{\mathrm{n(HI)}}{\mathrm{n(HII)}}$. That parameterization is unchanged from E. Aver et al. (2021). Also as in E. Aver et al. (2021), collisional excitations to P13, P14, and P15 are extrapolated according to a scaling law due to the available collisional

Table F1
Neutral Hydrogen Collisional Correction Coefficients

Line	Coefficient	Terms
P13	a	2.5140
	b	−15.689
	c	1.0223
P14	a	2.4148
	b	−15.702
	c	1.0305
P15	a	2.3287
	b	−15.712
	c	1.0374

Note. Coefficients for the neutral hydrogen collisional correction for P13–P15 in Equation (F1). This table augments Table 8 from E. Aver et al. (2021).

excitation calculations not including $n > 8$ (L. Fernández-Menchero et al. 2016; E. Aver et al. 2021).

For P13, P14, and P15, Table F1 lists the coefficients for constructing $\frac{K_{\rm eff}}{\alpha_{\rm eff}} \times 10^{-4}$, which is the quantity that multiplies ξ_4 and provides the increasing collisional enhancement factor for increasing temperature ($T_4 = T_{\rm e}/10^4$). Table F1 augments Table 8 from E. Aver et al. (2021).

Appendix G
Accounting for a Large Dispersion in Data

A large quantity of lower-quality data (e.g., SDSS observations) not only increases the vulnerability to systematic uncertainties but artificially reduces the statistical uncertainty in the determination of $Y_{\rm p}$.

When calculating the weighted mean, we apply a correction to the calculated uncertainty in the mean due to dispersive data. Given a set of helium abundances, $Y_i \pm \sigma_i$, the weighted mean is given by

$$\bar{Y} \pm \bar{\sigma} = \frac{\Sigma_i w_i Y_i}{\Sigma_i w_i} \pm (\Sigma_i w_i)^{-\frac{1}{2}}, \tag{G1}$$

where

$$w_i = \frac{1}{\sigma_i^2}. \tag{G2}$$

Given enough sample points, even with relatively large σ_i, an artificially small value of $\bar{\sigma}$ will result. The amount of dispersion can be evaluated relative to the mean value by calculating the χ^2 per degree of freedom, which is simply

$$S^2 \equiv \frac{\chi^2}{N-1} = \frac{\Sigma_i w_i (\bar{Y} - Y_i)^2}{N-1}, \tag{G3}$$

where N is the number of independent helium measurements. In the event that $S^2 > 1$ (but not very large), we correct the calculated uncertainty so that the mean and uncertainty is given by

$$\bar{Y} \pm \bar{\sigma} \times S. \tag{G4}$$

This is the standard procedure used in the Review of Particle Physics (S. Navas et al. 2024). If $S \leqslant 1$, no correction is made. If $S \gg 1$, one should question the validity of averaging the data.

For linear regressions, we compute the intercept (corresponding to primordial helium) and its uncertainty as well as the slope (and its uncertainty) using the uncertainties in both Y_i and the oxygen abundance, $X_i \pm \sigma_{X_i}$. More specifically, we use York's method (D. York 1966), as described in detail in B. C. Reed (1989, 1992). These also include the factor of S when computing uncertainties. The S factor is now given by

$$S^2 = \frac{\Sigma_i w_i (a + bX_i - Y_i)^2}{N-2}, \tag{G5}$$

where now

$$w_i = \frac{w_{X_i} w_{Y_i}}{w_{X_i} + b^2 w_{Y_I}}, \tag{G6}$$

and a and b are the derived intercept and slope, respectively. The individual weights are derived as in Equation (G2) for X and Y separately. We are assuming that the uncertainties on the data points are uncorrelated. The expressions for the slope (which is determined by the minimization of a cubic equation in the slope), the intercept, and their respective uncertainties are somewhat cumbersome, and we refer the reader to the references given above.

For linear regressions, we also use the program LINMIX, a Bayesian MCMC approach to linear regression allowing for uncertainties in both x and y (B. C. Kelly 2007). LINMIX determines its returned slope and intercept from the median values from 10,000 Markov Chains. LINMIX has the additional attribute that it fits for an intrinsic scatter in the data. For typical datasets, the results from York's method and LINMIX should be comparable.

ORCID iDs

Erik Aver https://orcid.org/0009-0006-2077-2552
Evan D. Skillman https://orcid.org/0000-0003-0605-8732
Richard W. Pogge https://orcid.org/0000-0003-1435-3053
Noah S. J. Rogers https://orcid.org/0000-0002-0361-8223
Miqaela K. Weller https://orcid.org/0000-0003-4912-5157
Keith A. Olive https://orcid.org/0000-0001-7201-5998
Danielle A. Berg https://orcid.org/0000-0002-4153-053X
John J. Salzer https://orcid.org/0000-0001-8483-603X
John H. Miller, Jr. https://orcid.org/0000-0002-2901-5260
José Eduardo Méndez-Delgado https://orcid.org/0000-0002-6972-6411

References

Astropy Collaboration, Price-Whelan, A. M., Lim, P. L., et al. 2022, ApJ, 935, 167
Astropy Collaboration, Price-Whelan, A. M., Sipőcz, B. M., et al. 2018, AJ, 156, 123
Astropy Collaboration, Robitaille, T. P., Tollerud, E. J., et al. 2013, A&A, 558, A33
Aver, E., Berg, D. A., Hirschauer, A. S., et al. 2022, MNRAS, 510, 373
Aver, E., Berg, D. A., Olive, K. A., et al. 2021, JCAP, 2021, 027
Aver, E., Olive, K. A., Porter, R. L., & Skillman, E. D. 2013, JCAP, 2013, 017
Aver, E., Olive, K. A., & Skillman, E. D. 2010, JCAP, 2010, 003
Aver, E., Olive, K. A., & Skillman, E. D. 2011, JCAP, 2011, 043
Aver, E., Olive, K. A., & Skillman, E. D. 2012, JCAP, 2012, 004
Aver, E., Olive, K. A., & Skillman, E. D. 2015, JCAP, 2015, 011
Balashev, S. A., Zavarygin, E. O., Ivanchik, A. V., Telikova, K. N., & Varshalovich, D. A. 2016, MNRAS, 458, 2188
Benjamin, R. A., Skillman, E. D., & Smits, D. P. 1999, ApJ, 514, 307
Benjamin, R. A., Skillman, E. D., & Smits, D. P. 2002, ApJ, 569, 288
Berg, D. A., Chisholm, J., Erb, D. K., et al. 2021, ApJ, 922, 170
Berg, D. A., Sanders, R. L., Shapley, A. E., et al. 2026, ApJ, 996, 68
Berg, D. A., Skillman, E. D., Marble, A. R., et al. 2012, ApJ, 754, 98
Calabrese, E., Hill, J. C., Jense, H. T., et al. 2025, JCAP, 2025, 063
Camphuis, E., Quan, W., Balkenhol, L., et al. 2026, PhRvD, 113, 083504
Cardelli, J. A., Clayton, G. C., & Mathis, J. S. 1989, ApJ, 345, 245
Cooke, R. J., & Fumagalli, M. 2018, NatAs, 2, 957
Cooke, R. J., Pettini, M., Jorgenson, R. A., Murphy, M. T., & Steidel, C. C. 2014, ApJ, 781, 31
Cooke, R. J., Pettini, M., Nollett, K. M., & Jorgenson, R. 2016, ApJ, 830, 148
Cooke, R. J., Pettini, M., & Steidel, C. C. 2018, ApJ, 855, 102
Croxall, K. V., & Pogge, R. W. 2019, rwpogge/modsIDL: modsIDL Binocular Release, v1.0, Zenodo, doi:10.5281/zenodo.2561424
Cyburt, R. H., Fields, B. D., Olive, K. A., & Yeh, T.-H. 2016, RvMP, 88, 015004
Dearborn, D. S. P., Steigman, G., & Tosi, M. 1996, ApJ, 465, 887
Del Zanna, G., & Storey, P. J. 2022, MNRAS, 513, 1198
Ekta, B., & Chengalur, J. N. 2010, MNRAS, 406, 1238
Eldridge, J. J., & Stanway, E. R. 2009, MNRAS, 400, 1019
Eldridge, J. J., Stanway, E. R., Xiao, L., et al. 2017, PASA, 34, e058
Fernández, V., Terlevich, E., Díaz, A. I., & Terlevich, R. 2019, MNRAS, 487, 3221

Fernández, V., Terlevich, E., Díaz, A. I., Terlevich, R., & Rosales-Ortega, F. F. 2018, MNRAS, 478, 5301
Fernández-Menchero, L., Del Zanna, G., & Badnell, N. R. 2016, A&A, 592, A135
Fields, B. D., & Olive, K. A. 2022, JCAP, 2022, 078
Fields, B. D., Olive, K. A., Yeh, T.-H., & Young, C. 2020, JCAP, 2020, 010
García-Rojas, J., & Esteban, C. 2007, ApJ, 670, 457
Garnett, D. R. 1990, ApJ, 363, 142
Guarneri, F., Pasquini, L., D'Odorico, V., et al. 2024, MNRAS, 529, 839
Guseva, N. G., Izotov, Y. I., Fricke, K. J., & Henkel, C. 2015, A&A, 579, A11
Guseva, N. G., Izotov, Y. I., Papaderos, P., & Fricke, K. J. 2007, A&A, 464, 885
Guseva, N. G., Izotov, Y. I., & Thuan, T. X. 2006, ApJ, 644, 890
Harris, C. R., Millman, K. J., van der Walt, S. J., et al. 2020, Natur, 585, 357
Henney, W. J. 2021, MNRAS, 502, 4597
Hsyu, T., Cooke, R. J., Prochaska, J. X., & Bolte, M. 2020, ApJ, 896, 77
Hummer, D. G., & Storey, P. J. 1987, MNRAS, 224, 801
Iocco, F., Mangano, G., Miele, G., Pisanti, O., & Serpico, P. D. 2009, PhR, 472, 1
Izotov, Y. I., Chaffee, F. H., Foltz, C. B., et al. 1999, ApJ, 527, 757
Izotov, Y. I., & Thuan, T. X. 2004, ApJ, 602, 200
Izotov, Y. I., Thuan, T. X., & Guseva, N. G. 2014, MNRAS, 445, 778
Izotov, Y. I., Thuan, T. X., & Stasińska, G. 2007, ApJ, 662, 15
Kelly, B. C. 2007, ApJ, 665, 1489
Kislitsyn, P. A., Balashev, S. A., Murphy, M. T., et al. 2024, MNRAS, 528, 4068
Kluyver, T., Ragan-Kelley, B., Pérez, F., et al. 2016, in Jupyter Notebooks—a publishing format for reproducible computational workflows, ed. F. Loizides & B. Schmidt (IOS Press), 87
Kurichin, O., & Ivanchik, A. 2026, PhRvD, 113, 043012
Kurichin, O. A., Kislitsyn, P. A., Klimenko, V. V., Balashev, S. A., & Ivanchik, A. V. 2021, MNRAS, 502, 3045
Lodders, K., Bergemann, M., & Palme, H. 2025, SSRv, 221, 23
Louis, T., La Posta, A., Atkins, Z., et al. 2025, JCAP, 2025, 062
Luridiana, V., Morisset, C., & Shaw, R. A. 2012, IAUS, 283, 422
Luridiana, V., Morisset, C., & Shaw, R. A. 2015, A&A, 573, A42
Markov, A. A. 1906, Proc. Phys. Math. Soc. Kazan Univ., 15, 135
Matsumoto, A., Ouchi, M., Nakajima, K., et al. 2022, ApJ, 941, 167
McQuinn, K. B. W., Berg, D. A., Skillman, E. D., et al. 2020, ApJ, 891, 181
McQuinn, K. B. W., Skillman, E. D., Dolphin, A., et al. 2015, ApJL, 815, L17
Méndez-Delgado, J. E., Skillman, E. D., Aver, E., et al. 2025, ApJ, 986, 74
Metropolis, N., Rosenbluth, A. W., Rosenbluth, M. N., Teller, A. H., & Teller, E. 1953, JChPh, 21, 1087
Navas, S., Amsler, C., Gutsche, T., et al. 2024, PhRvD, 110, 030001
Olive, K. A., Rood, R. T., Schramm, D. N., Truran, J., & Vangioni-Flam, E. 1995, ApJ, 444, 680
Olive, K. A., Schramm, D. N., Scully, S. T., & Truran, J. W. 1997, ApJ, 479, 752
Olive, K. A., & Skillman, E. D. 2001, NewA, 6, 119
Olive, K. A., & Skillman, E. D. 2004, ApJ, 617, 29
Olive, K. A., Steigman, G., & Walker, T. P. 2000, PhR, 333, 389
Osterbrock, D. E., & Ferland, G. J. 2006, Astrophysics of Gaseous Nebulae and Active Galactic Nuclei (Univ. Science Books)
Peimbert, A., Peimbert, M., & Luridiana, V. 2002, ApJ, 565, 668
Peimbert, A., Peimbert, M., & Luridiana, V. 2016, RMxAA, 52, 419
Peimbert, M. 1967, ApJ, 150, 825
Peimbert, M., Peimbert, A., & Ruiz, M. T. 2000, ApJ, 541, 688
Pitrou, C., Coc, A., Uzan, J.-P., & Vangioni, E. 2018, PhR, 754, 1
Planck Collaboration, Aghanim, N., Akrami, Y., et al. 2020, A&A, 641, A6
Pogge, R. 2019, rwpogge/modsCCDRed: v2.0.1, Zenodo, doi:10.5281/zenodo.2647501
Porter, R. L., Ferland, G. J., Storey, P. J., & Detisch, M. J. 2012, MNRAS, 425, L28
Porter, R. L., Ferland, G. J., Storey, P. J., & Detisch, M. J. 2013, MNRAS, 433, L89
Prochaska, J., Hennawi, J., Westfall, K., et al. 2020, JOSS, 5, 2308
Prochaska, J. X., Hennawi, J., Cooke, R., et al. 2020, pypeit/PypeIt: Release v1.0.0, Zenodo, doi:10.5281/zenodo.3743493
Reed, B. C. 1989, AmJPh, 57, 642
Reed, B. C. 1992, AmJPh, 60, 59
Riemer-Sørensen, S., Kotuš, S., Webb, J. K., et al. 2017, MNRAS, 468, 3239
Riemer-Sørensen, S., Webb, J. K., Crighton, N., et al. 2015, MNRAS, 447, 2925
Rogers, N. S. J., Skillman, E. D., Pogge, R. W., et al. 2026, ApJ, 1008, 238
Rosenfeld, A. H. 1975, ARNPS, 25, 555
Schlafly, E. F., & Finkbeiner, D. P. 2011, ApJ, 737, 103
Skillman, E. D., Pogge, R. W., Aver, E., et al. 2026, ApJ, 1008, 237
Skillman, E. D., Salzer, J. J., Berg, D. A., et al. 2013, AJ, 146, 3
Spite, F., & Spite, M. 1982, A&A, 115, 357
Stanway, E. R., & Eldridge, J. J. 2018, MNRAS, 479, 75
Storey, P. J., & Hummer, D. G. 1995, MNRAS, 272, 41
Storey, P. J., & Sochi, T. 2015, MNRAS, 446, 1864
Valerdi, M., Peimbert, A., Peimbert, M., & Sixtos, A. 2019, ApJ, 876, 98
Vangioni-Flam, E., Olive, K. A., Fields, B. D., & Cassé, M. 2003, ApJ, 585, 611
Vilchez, J. M., & Pagel, B. E. J. 1988, MNRAS, 231, 257
Weller, M. K., Pogge, R. W., Skillman, E. D., et al. 2026, ApJ, 1008, 239
Weller, M. K., Weinberg, D. H., & Johnson, J. W. 2025, MNRAS, 538, 1517
Yanagisawa, H., Ouchi, M., Matsumoto, A., et al. 2026, ApJ, 1004, 55
Yanagisawa, H., Ouchi, M., Watanabe, K., et al. 2024, ApJ, 974, 266
Yang, J., Turner, M. S., Steigman, G., Schramm, D. N., & Olive, K. A. 1984, ApJ, 281, 493
Yeh, T.-H., Olive, K. A., & Fields, B. D. 2023, Univ, 9, 183
Yeh, T.-H., Olive, K. A., Fields, B. D., et al. 2026, ApJ, 1008, 241
Yeh, T.-H., Shelton, J., Olive, K. A., & Fields, B. D. 2022, JCAP, 2022, 046
York, D. 1966, CaJPh, 44, 1079
Zavarygin, E. O., Webb, J. K., Dumont, V., & Riemer-Sørensen, S. 2018, MNRAS, 477, 5536